

2016-01-01

Manufacturing and Mechanics of Polymer Matrix Composites

Md Shariful Islam

University of Texas at El Paso, msislam64@gmail.com

Follow this and additional works at: https://digitalcommons.utep.edu/open_etd



Part of the [Mechanical Engineering Commons](#)

Recommended Citation

Islam, Md Shariful, "Manufacturing and Mechanics of Polymer Matrix Composites" (2016). *Open Access Theses & Dissertations*. 863.
https://digitalcommons.utep.edu/open_etd/863

This is brought to you for free and open access by DigitalCommons@UTEP. It has been accepted for inclusion in Open Access Theses & Dissertations by an authorized administrator of DigitalCommons@UTEP. For more information, please contact lweber@utep.edu.

MANUFACTURING AND MECHANICS OF POLYMER MATRIX COMPOSITES

MD SHARIFUL ISLAM

Doctoral Program in Mechanical Engineering

APPROVED:

Pavana Prabhakar, Ph.D., Chair

Cesar Carrasco, Ph.D.

Chintalapalle Ramana, Ph.D.

Yirong Lin, Ph.D.

Charles Ambler, Ph.D.
Dean of the Graduate School

©Copyright

by

Md Shariful Islam

2016

to my
PARENTS
with love

MANUFACTURING AND MECHANICS OF POLYMER MATRIX COMPOSITES

by

MD SHARIFUL ISLAM

THESIS

Presented to the Faculty of the Graduate School of

The University of Texas at El Paso

in Partial Fulfillment

of the Requirements

for the Degree of

DOCTOR OF PHILOSOPHY

Doctoral Program in Mechanical Engineering

THE UNIVERSITY OF TEXAS AT EL PASO

August 2016

Acknowledgements

I received extraordinary support from many people during different stages of my doctoral program and I would like to take this opportunity to thank all of them. I would like to thank my adviser Dr. Pavana Prabhakar for her continuous support and belief in my abilities. I hope to carry her advice and knowledge that she passed on into my future endeavors. It is an honor and privilege to express my appreciation to my committee members Dr. Cesar Carrasco, Dr. Chintalapalle Ramana and Dr. Yirong Lin who have given their valuable time and support. I would also like to thank my group members specially Raudel and Alejandra for their help and support. Special thank goes to all the members of Bangladeshi Community of El Paso, it was not possible to live here in El Paso without their help and support. Last but not the least, I would like to express my deep gratitude to all my family members for their inspiration and sacrifice throughout this journey.

Abstract

Fiber-reinforced composite materials are widely used in the aerospace and automobile industries. Their strength-to-weight and stiffness-to-weight ratios make them suitable to be used in spacecraft, especially as cryogenic tank materials. One of the focus of this dissertation is to investigate the application of woven carbon and Kevlar[®] fiber composites as cryogenic tank materials. Tensile, bending and short beam shear tests are performed on rectangular specimens at room temperature and after cryogenic exposure (-196°C). It is found that the mechanical properties of these composite materials do not degrade significantly due to cryogenic exposure. It is observed that the failure mode took place before and after the cryogenic exposure is identical, which implies that the carbon and Kevlar[®] fiber composite can be used as a cryogenic tank materials. Hybridization of this two types of composites (carbon and Kevlar[®] fiber) is also studied. A computational study is conducted to reduce the number of experiments, and to find the optimum combination of carbon and Kevlar[®] fiber reinforcements. Thirty different combinations of hybrid composites are studied computationally and six of these combinations are found suitable based on minimum number of peak stress and minimum peak stress value. This six optimum combinations along with some other combinations are manufactured by using the Vacuum Assisted Resin Transfer Molding (VARTM) process to facilitate comparative study. Comparison of mechanical test results performed on full cryogenic exposure, gradient exposure and pristine materials shows that the hybrid composites can be used as cryogenic tank materials.

Another important aspect of this dissertation is to study the inter-laminar reinforcement of multi-directional laminates by using additive manufacturing technology. Under thermos-mechanical loading, very high stress can be developed at the interfaces due to property mismatch between different plies leading to premature failure. In order to reinforce those interfaces, it is very important to identify these delamination prone interfaces. A novel semi-analytical model is developed to find the delamination prone interfaces in a multidirectional laminates under thermo-mechanical loading and the results of this model

is compared with previously published results. Very thin lines of polylactic acid (PLA) are printed on the critical interfaces in multi-directional laminate by using MakerBot Replicator Desktop 3D printer and it is found that, inter-laminar shear strength (ILSS) is increased by approximately 28 %. So, the additive manufacturing technology can be used to increase inter-laminar strength of multi-directional laminate.

Table of Contents

	Page
Acknowledgements	v
Abstract	vi
Table of Contents	viii
List of Tables	xii
List of Figures	xiii
Chapter	
1 Introduction	1
1.1 Types of Composites	1
1.2 Manufacturing Process of Composites	3
1.3 Applications of Composites	4
1.4 Main Contributions and Organization of the Thesis	5
2 Investigation of Woven Composites as Potential Cryogenic Tank Materials . . .	7
2.1 Introduction	7
2.2 Experimental Procedure	11
2.2.1 Material System	11
2.2.2 Manufacturing Process: Vacuum Assisted Resin Transfer Molding .	12
2.2.3 Exposure to Cryogenic Environment	12
2.2.4 Tensile Tests	13
2.2.5 Flexural Test	14
2.2.6 Short Beam Shear Test	15
2.3 Results and Discussion	15
2.3.1 Tension Test Results	16
2.3.2 Flexural Test Results	17
2.3.3 SBS Test Results	18
2.4 Pictographic Analysis	18

2.5	Conclusions	21
3	Hybrid Textile Composites as Potential Cryogenic Tank Materials	22
3.1	Introduction	22
3.2	Levels of Hybridization	26
3.3	Computational Analysis for Hybridization Process under Cryogenic Exposure	28
3.3.1	Transient Heat Transfer Analysis	29
3.3.2	Stress Analysis	30
3.3.3	Results from the Computational Study for Uniform Surface Cryo- genic Exposure	31
3.3.4	Computational Stress Analysis with Interlaminar Matrix Layer . . .	33
3.4	Experimental Procedure	34
3.4.1	Manufacturing	34
3.4.2	Exposure to Cryogenic Environment	35
3.4.3	Short Beam Shear Test	36
3.5	Computational Analysis of Gradient Cryogenic Exposure	37
3.5.1	Temperature Distribution	37
3.5.2	Stress Distribution	38
3.5.3	ABS Plastic Holder Computational Design and Manufacturing . . .	38
3.6	Experimental Study of Gradient Cryogenic Exposure on Composites	40
3.7	Fractographic Analysis of Gradient Exposed Hybrid Composites	42
3.7.1	100 % Carbon and 100 % Kevlar®	43
3.7.2	75 % Carbon - 25 % Kevlar®	43
3.7.3	50 % Carbon - 50 % Kevlar®	44
3.7.4	25 % Carbon - 75 % Kevlar®	45
3.8	Conclusions	45
4	Novel Model for Free Edge Effects in Laminates under Thermo-Mechanical Loading	47
4.1	Introduction	47
4.2	Mathematical Formulation	50

4.3	Implementation of the Quasi-2D Formulation	54
4.4	Results and Discussions	56
4.4.1	Case 1: Axial Loading	57
4.4.2	Case 2: Thermal Loading	59
4.4.3	Case 3: Combined Axial and Thermal Loading	60
4.4.4	Efficiency of Q-2D Model	61
4.5	Conclusions	62
5	Interface Strengthening of Multi-directional Laminates using Additive Manufacturing	64
5.1	Introduction	64
5.2	Determination of Delamination Prone inter-laminar regions	66
5.3	Experimental Details	67
5.3.1	Types of laminate investigated	67
5.3.2	Material system	68
5.3.3	3D printing on pre-pregs	68
5.3.4	Laminate Fabrication	70
5.3.5	Short beam shear test	71
5.4	Results and Discussions	72
5.5	Conclusions	76
6	Concluding Remarks	78
6.1	Conclusions	78
6.2	Future Work	79
Appendix		
A	Computational Modeling of Curing Induced Damage due to Compaction on Woven Fabric Composites	80
A.1	Introduction	80
A.2	Woven Composite-Mesoscale Model	83
A.2.1	Geometry of the Representative Volume Element (RVE)	83

A.2.2	Material System	83
A.3	Curing Model for Resin	84
A.3.1	Evolution of Temperature and the Degree of Cure	84
A.3.2	Evolution of Stresses during Curing	85
A.3.3	Modeling Damage due to Cure Shrinkage with Crack Band Model .	88
A.4	Curing Study with Matrix Degradation	91
A.5	Effect of Temperature Cycle	92
A.6	Effect of Compaction	94
A.7	Conclusion	96
References	98
Curriculum Vitae	114

List of Tables

2.1	Fabric properties (fibreglast.com)	11
2.2	Tensile test results with standard deviation	17
2.3	Three point bending test results with standard deviation	18
3.1	Layer Combinations with Volume Fraction	27
3.2	Thermo-Physical Properties of Carbon and Kevlar [®] Lamina	30
3.3	Mechanical Properties of Carbon and Kevlar [®] Lamina	30
3.4	Coefficient of Thermal Expansion for Kevlar [®] Lamina	30
3.5	Coefficient of Thermal Expansion for Carbon Lamina	31
3.6	Fabric Properties (fibreglast.com)	35
3.7	Epoxy Matrix Properties	35
4.1	Comparison of Q-2D and 3D model	62
5.1	Pre-pregs properties (www.cstsales.com)	68
5.2	Comparison of ILSS of different laminates	74
A.1	Tow properties	84
A.2	Matrix properties	84

List of Figures

1.1	Phases of a composite material	1
1.2	Types of fiber reinforced composites; (a) Particulate composites, (b) Discontinuous fiber composites and (c) Continuous fiber composites	2
1.3	Types of continuous fiber composites; (a) Unidirectional composites, (b) Cross-ply composites and (c) Multi-directional composites	3
1.4	Schematic diagram of VARTM process	4
1.5	Some applications of composite materials	5
2.1	(a) NASA's Composite Cryogenic Fuel Tank, (b) Schematic of Fiber-Reinforced Laminate Overwrap and (c) Schematic of Textile Composite Pressure Vessel	10
2.2	VARTM process: (a) Material Layup for the Mold; (b) Mold with Dry Fabric; (c) Vacuum Bag with Resin Infusion	13
2.3	(a) Cryogenic Exposure Container; (b) Instron Test Frame	14
2.4	Bar Chart showing (a) Tensile Chord Modulus and (b) Tensile Strength for both Composites with Standard Deviation	16
2.5	Bar Chart showing (a) Flexural Chord Modulus and (b) Flexural Strength for both Composites with Standard Deviation	17
2.6	Bar Chart showing ILSS for both Composites with Standard Deviation . .	18
2.7	Scanning Electron Microscope (SEM) Images of Carbon Composite (a) at Room Temperature; (b) after Cryogenic Exposure	19
2.8	Scanning Electron Microscope (SEM) Images of Kevlar® Composite (a) at Room Temperature; (b) after Cryogenic Exposure	19
2.9	Optical Microscope Images of Failed Carbon Composite (a) at Room Temperature; (b) after Cryogenic Exposure	20
2.10	Optical Microscope Images of Failed Kevlar® Composite (a) at Room Temperature; (b) after Cryogenic Exposure	20

2.11	Three Point Bending Test of Kevlar [®] Fiber Specimen	21
3.1	(a) NASA's Composite Cryogenic Fuel Tank, (b) Schematic of Fiber-Reinforced Laminate Over wrap and (c) Schematic of Textile Composite Pressure Vessel	25
3.2	Cross Section of [K6C6] _s Hybrid Composite	27
3.3	(a) Steps involved in the Computational Framework (b) Cryogenic Thermal Exposure of Hybrid Composites	28
3.4	Hybrid Composite Model in ABAQUS	29
3.5	Cryogenic Thermal Exposure of Composites	31
3.6	Maximum Principal Stress for 75% Carbon - 25% Kevlar [®]	32
3.7	Maximum Principal Stress for 50% Carbon - 50% Kevlar [®]	32
3.8	Maximum Principal Stress for 25% Carbon - 75% Kevlar [®]	33
3.9	Hybrid Composite Based on (a) Minimum Peak Stress Values and (b) Min- imum Number of Peak Values	33
3.10	Schematic of Composite with Interlaminar Epoxy Matrix	34
3.11	Maximum Principal Stress Computed in the Matrix Section for the Optimal Cases Mentioned in Fig 3.9.	34
3.12	(a) Cryogenic Exposure Container; (b) Instron Test Frame	36
3.13	Schematic of Gradient Exposure in a Hybrid Composite	37
3.14	(a) Temperature Distribution of the Composites after Gradient Exposure (b) Stress Distribution of the Composites after Gradient Exposure	38
3.15	(a) ABS Plastic Holder Model (b) Temperature Distribution Inside the Plas- tic Holder	39
3.16	(a) ABS Holder After Layers of Insulation (b) Final Hybrid Composite Position	40
3.17	(a) ABS Holder Before Cryogenic Exposure (b) Liquid Nitrogen Exposure (c) ABS Holder After Gradient Cryogenic Exposure	40
3.18	ILSS for the Hybrid Composites under Different Conditions	41
3.19	Load vs Deflection curves for the Hybrid Composites after Gradient Exposure	42

3.20	(a) C24 Fractographic Analysis (b) K24 Fractographic Analysis	43
3.21	(a) [KCKCKC7] _s Fractographic Analysis (b) [C3K3C6] _s Fractographic Analysis	44
3.22	(a) [C6K6] _s Fractographic Analysis (b) [C4K6C2] _s Fractographic Analysis .	45
3.23	(a) [CKCKCK7] _s Fractographic Analysis (b) [K9C3] _s Fractographic Analysis	46
4.1	(a) 3D Laminate; (b) Cross-section of a 3D laminate	50
4.2	3D slice of a laminate	54
4.3	(a) Typical mesh in the Q-2D model; (b) Working principle of python TM script	55
4.4	Snapshot of (a) input file and (b) equation file	56
4.5	Boundary conditions for uniaxial extension	56
4.6	Distribution of interlaminar stresses along the 0/90 interface of [0/90] _s laminate subjected to uniform axial extension (a) normal stress σ_{33} and (b) shear stress σ_{23}	57
4.7	Distribution of interlaminar stress of [45/ - 45/90/0] _s laminate subjected to uniform axial extension along (a) 45/-45, (b) -45/90 and (c) 90/0 interface	58
4.8	Distribution of interlaminar stresses along the 0/90 interface of [0/90] _s laminate due to a temperature change $\Delta T = 1\text{ }^{\circ}\text{C}$ (a) normal stress σ_{33} and (b) shear stress σ_{23}	59
4.9	Distribution of interlaminar stress of [45/ - 45/90/0] _s laminate due to a temperature change $\Delta T = 25\text{ }^{\circ}\text{C}$ (a) 45/-45, (b) -45/90 and (c) 90/0 interface	60
4.10	Distribution of interlaminar stress along the 0/90 interface of [0/90] _s laminate subjected to $\epsilon_{11} = 0.01$ and $\Delta T = 25\text{ }^{\circ}\text{C}$ (a) normal stress σ_{33} and (b) shear stress σ_{23}	61
4.11	Distribution of interlaminar stress of [45/ - 45/90/0] _s laminate subjected to $\epsilon_{11} = 0.01$ and $\Delta T = 25\text{ }^{\circ}\text{C}$ along (a) 45/-45, (b) -45/90 and (c) 90/0 interface	62
5.1	Schematic cross section of laminate	67

5.2	Distribution of interlaminar stress along along different inter-laminar regions of $[45_2/-45_2/90_2/0_2]_s$ laminate (a) normal stress σ_{33} and (b) shear stress σ_{23}	67
5.3	(a) MakerBot Replicator desktop 3D printer and (b) 3D printing on pre-pregs	69
5.4	Raft settings (a) default and (b) custom	70
5.5	Printed raft (a) default and (b) custom	70
5.6	(a) 3D printed lines on prepreg and (b) Schematic cross-section of 3D printed prepreg	71
5.7	Manufacturing of laminate	71
5.8	Cross section of 3D printed laminate (a) type A and (b) type B	72
5.9	Cross section of 3D printed laminate with additional resins (a) type A and (b) type B	73
5.10	Bar chart showing ILSS for composites with standard deviation	74
5.11	Formation of teeth along the 3D printed inter-laminar region	74
5.12	Cross section along with top and bottom surfaces of type A laminate (a) pristine, (b) 3D printed inter-laminar region and (c) 3D printed inter-laminar region with additional resin	75
5.13	Cross section along with top and bottom surfaces of type A laminate (a) pristine, (b) 3D printed inter-laminar region and (c) 3D printed inter-laminar region with additional resin	76
A.1	RVE of woven composite used	83
A.2	Variation of elastic modulus with respect to the degree of cure	87
A.3	Variation of the elastic modulus with respect to the degree of cure and separation (from cohesive law) in the material	89
A.4	Converting traction-separation law to traction-strain law	90
A.5	CBM: modified stress-strain material law incorporating failure	90
A.6	Curing cycles	91

A.7	Cure Cycle 1: Damage initiated regions corresponding to critical stress of (a) 45 MPa, (b) 60 MPa, (c) 75 MPa and (d) 90 MPa	92
A.8	Cure Cycle 2: Damage initiated regions corresponding to critical stress of (a) 45 MPa, (b) 60 MPa, (c) 75 MPa and (d) 90 MPa	93
A.9	Cure Cycle 1: Failed regions corresponding to critical stress of (a) 45 MPa, (b) 60 MPa, (c) 75 MPa and (d) 90 MPa	94
A.10	Cure Cycle 2: Failed regions corresponding to critical stress of (a) 45 MPa, (b) 60 MPa, (c) 75 MPa and (d) 90 MPa	95
A.11	Cure Cycle 1: Failed regions corresponding to critical stress of 45 MPa for a compaction of (a) 0 MPa, (b) 1.5 MPa, (c) 3 MPa and (d) 5 MPa	96
A.12	Cure Cycle 1: Failed regions corresponding to critical stress of 60 MPa for a compaction of (a) 0 MPa, (b) 1.5 MPa, (c) 3 MPa and (d) 5 MPa	97

Chapter 1

Introduction

Composite materials are hybrid material system that consist of two or more materials combined at a macroscopic scale to form a new material with mechanical performance and properties superior to those of the individual constituent materials. One of the constituent materials (also referred to as phases) is usually discontinuous, stiffer and stronger, which is called the reinforcement, whereas, the weaker and continuous phase is called the matrix. Due to chemical interactions or other processing effects, an additional phase exists between the reinforcement and matrix which is called the interphase. Fig. 1.1 shows the different component of a composite material.

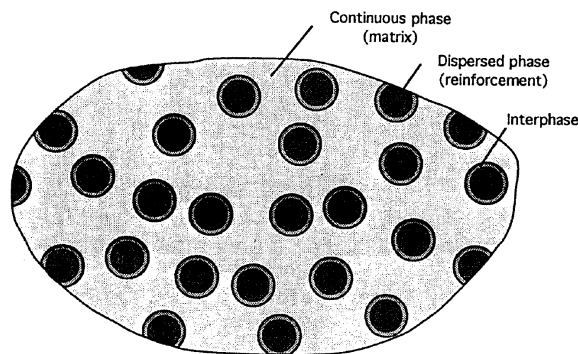


Figure 1.1: Phases of a composite material

1.1 Types of Composites

Two phase composite materials are broadly classified into three types: particulate composites, discontinuous or short fiber composites and continuous fiber composites. Particulate composites consist of particles of various sizes and shapes randomly dispersed within the

matrix. Discontinuous or short fiber composites consists of short fibers or whiskers dispersed within the matrix, and the orientation of these short fibers can either be oriented along one direction or randomly oriented. On the other hand, continuous fiber composites consist of long continuous fibers, and are most efficient compared to the other types in terms of strength and stiffness. Fig. 1.2 shows different fiber reinforced composites. Continuous fiber can be classified as unidirectional (all fibers oriented along one direction), cross-ply (fibers oriented at right angles to each other) and multi-directional (fibers oriented along several directions). Fig. 1.3 displays the different types of continuous fiber composites.

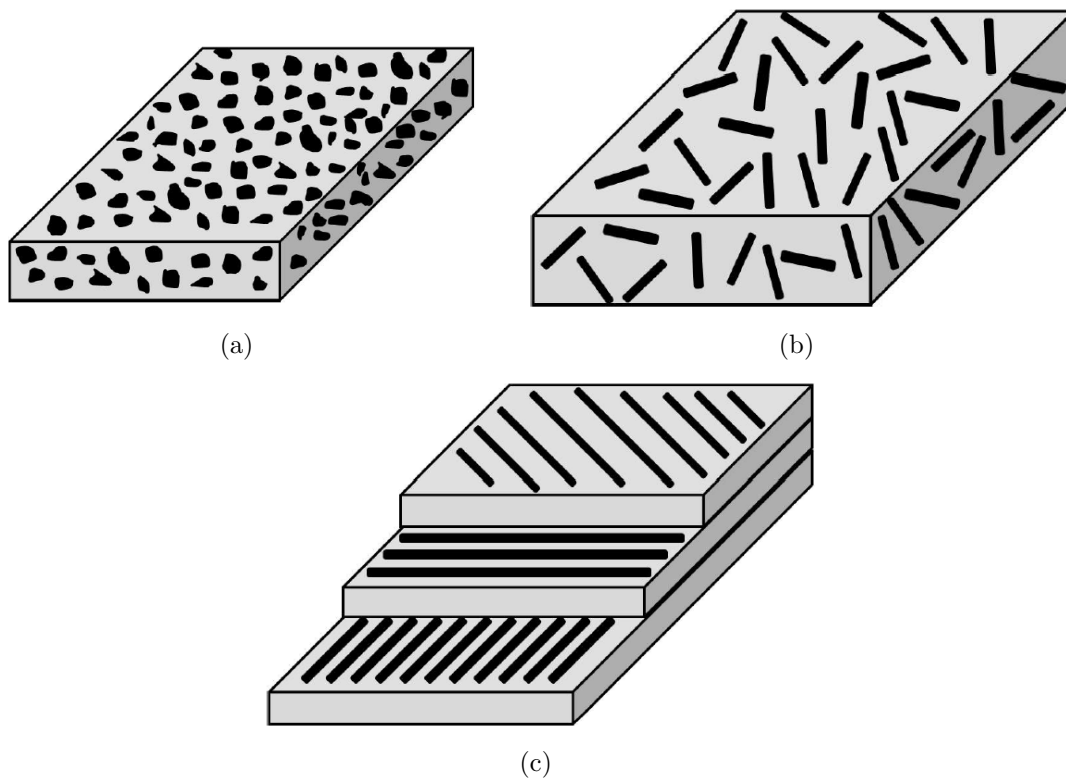


Figure 1.2: Types of fiber reinforced composites; (a) Particulate composites, (b) Discontinuous fiber composites and (c) Continuous fiber composites

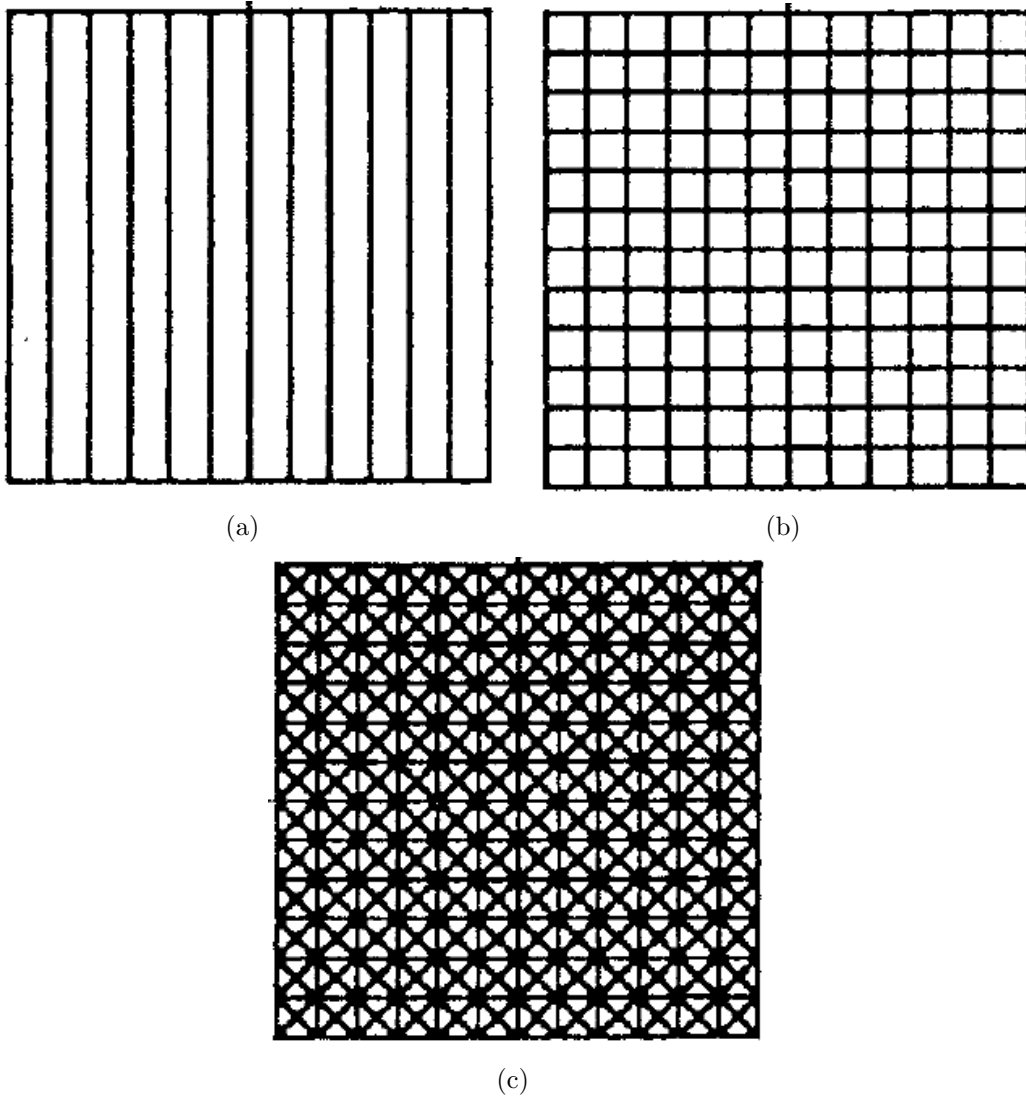


Figure 1.3: Types of continuous fiber composites; (a) Unidirectional composites, (b) Cross-ply composites and (c) Multi-directional composites

1.2 Manufacturing Process of Composites

There are several manufacturing processes for composites such as, hand lay-up, vacuum bagging/autoclave, compression molding, liquid resin molding, pultrusion, filament winding, injection molding etc. Each process has its own advantages and disadvantages, and

Vacuum Assisted Resin Transfer Molding (VARTM) and hand lay-up processes are used to manufacture composites in this thesis. Fig. 1.4 shows the schematic of the VARTM process. In this process, layers of dry preform (reinforcing fabric) are placed between two mold plates inside a vacuum bag. Vacuum is created using a vacuum pump and the resin flows from one side to the other of the mold. A detailed description of the VARTM process is given in section 2.2.2. The advantages of VARTM process are cost effective compared to other processes, lower tooling cost, shorter start-up time and can manufacture large scale component. There are also some disadvantages of this process as well which include, relatively complex process, difficulty in controlling the final thickness and fiber volume fraction of the composite due to the flexible nature of the vacuum bag [1, 2].

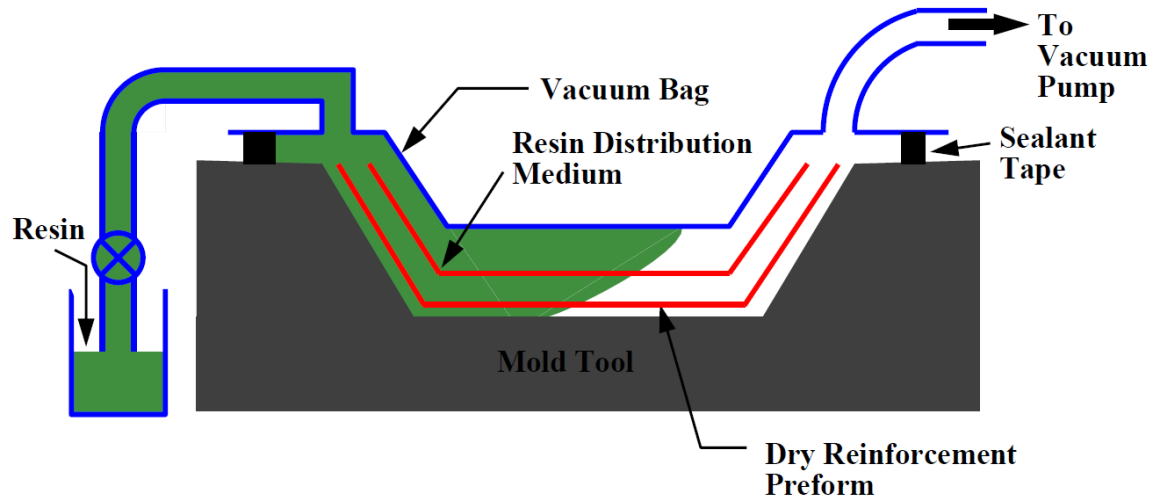


Figure 1.4: Schematic diagram of VARTM process

1.3 Applications of Composites

There are numerous applications of composite materials predominantly in the aerospace, naval, nuclear and automobile industries. Fig. 1.5 shows some applications of composite materials. In this thesis, application of composite materials specific to cryogenic environment is considered and the feasibility of using composite materials at cryogenic temperature

is investigated. Chapter 2 and 3 of this thesis are dedicated to this study in detail.

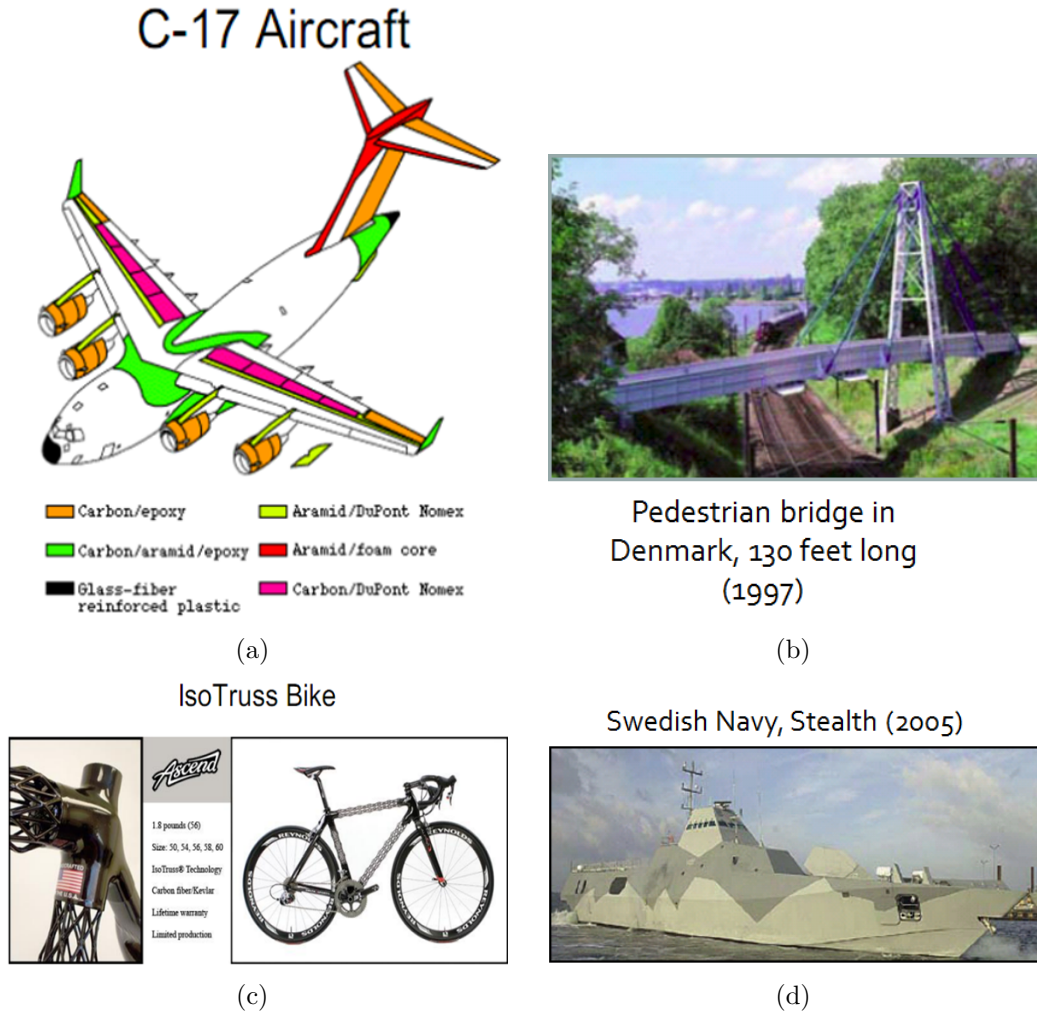


Figure 1.5: Some applications of composite materials

1.4 Main Contributions and Organization of the Thesis

In this thesis, the feasibility of woven carbon and Kevlar[®] fiber composites to be used as a potential cryogenic tank materials is investigated. Also, a novel computational method to

determine the inter-laminar stresses in multi-directional laminates to identify the delamination prone interfaces is also developed. And finally, a novel method to strengthen the critical interfaces in a multi-directional laminate is proposed in this thesis.

The dissertation is organized as follows; Chapter 2 presents the experimental investigation of woven composites to be used as potential cryogenic tank materials. Next, Chapter 3 discusses the hybridization technique of woven carbon fiber and Kevlar[®] fiber composites to minimize the adverse influence of cryogenic temperatures. Chapter 4 discusses the computational method developed to determine free edge effects in multi-directional laminates to identify the critical interfaces in multi-directional laminates. In Chapter 5, an manufacturing technique is developed to strengthen the interfacial strength of multi-directional laminates using additive manufacturing. The dissertation concludes with Chapter 6, which provides a summary of the main findings and suggestions for future work.

The research presented in this thesis are already published or under review in peer reviewed scientific journals and presented in several international conferences.

Chapter 2

Investigation of Woven Composites as Potential Cryogenic Tank Materials

In this chapter, carbon fiber and Kevlar[®] fiber woven composites were investigated as potential cryogenic tank materials for storing liquid fuel in spacecraft or rocket. Towards that end, both carbon and Kevlar[®] fiber composites are manufactured and tested with and without cryogenic exposure. The focus is on the investigation of the influence of initial cryogenic exposure on the degradation of the composite. Tensile, flexural and inter laminar shear strength (ILSS) tests are conducted, which indicate that Kevlar[®] and carbon textile composites are potential candidates for use under cryogenic exposure.

2.1 Introduction

The field of composite materials has gained importance within the study of engineering in the recent years. Developments in material science and the study of novel materials have allowed engineers to consider the use of alternative and less traditional materials in their designs. Composite materials have been known for providing good strength to weight ratios, improved thermal and mechanical properties, and many other desirable aspects which are obtained through the combination of different constituent materials. Among myriad applications of composite materials like aircraft and naval structures, automobiles, medical devices, etc., their use in cryogenic fuel tanks could result in an increase in the efficiency of the system.

Cryogenic tanks are commonly used to store extremely low temperature fluids, like liquid oxygen (-183°C), liquid methane (-161°C) or liquid hydrogen (-252°C) in their con-

densified form in order to generate highly combustible liquids. This type of tank, generally composed of different layers of insulators and some type of metal liners [3, 4], is exposed to an extremely cold temperature in its interior and to ambient temperature on its external surface. A large temperature gradient across the thickness of the wall often causes differential expansion and contraction across the tank walls, resulting in an uneven expansion or contraction of the material. If the stresses caused by this differential expansion exceed the strength of the material, cracks initiate and propagate in the direction of least resistance. In addition, if the boundaries of the material do not impede crack propagation, this will ultimately cause the tank's structure to fail, resulting in an undesirable leakage [5] that will consequently lead to the catastrophic fuel tank failure in the case of a rocket or spacecraft being launched into space.

National Aeronautics and Space Administration (NASA) recently (August 2014) completed a major space technology development milestone by successfully testing a large pressurized cryogenic propellant tank made of composite material [3]. The advancements made in the scope of composite materials have allowed for improvements in designs that were restrained in the past by a limited material selection. In the case of NASA, switching from metallic to composite construction has the potential to dramatically increase the performance capabilities of future space systems through a significant reduction in weight [3, 4, 6]. The applications and benefits that could be derived from further developing composite materials for cryogenic applications are countless. It would be of paramount interest to design better composite material systems, like textile composites that have superior structural [7, 8, 9, 10, 11, 12] and thermal properties compared to traditional laminates, as well as better draping compared to continuous fiber reinforced composites [10, 12]. Draping is the ability of woven textile fabric to conform to complex curved shapes, that is, regardless of the weave pattern, the fabric tows rotate freely to take the shape of the underlying structure [13]. Further, study by Potter [14] on the influence of stretching/draping of various reinforcements, like woven fabric (textiles), unidirectional and cross-ply layers on complex geometry has shown that the slippage capability between tows in woven fabric allows for

more stretch/easy draping compared to others without applying undue force.

Previous research regarding the use of composite materials as cryogenic tank materials mainly dealt with thermal cycling of unidirectional composites, and their damage behavior and permeability under fatigue-thermal loads [15, 16, 17, 18, 19, 20, 21, 22, 23, 24]. Gong et al. [25] studied the mechanical properties of unidirectional E-glass fiber/epoxy and carbon fiber/epoxy laminates at cryogenic temperature and Disdier et al. [26] studied helium permeation on woven E-glass fabric composites. Verstraete et al. [27] investigated hydrogen fuel tank with foam core and multilayer insulations (MLI) along with aluminum tank wall and composite fairing. Aceves et al. [28] explored aluminum-lined, fiber wrapped cryogenic hydrogen storage tank at different temperature and pressure cycles. Shindo et al. [29] evaluated the interlaminar shear strength (ILSS) of G-10CR glass-cloth/epoxy laminates at room temperature, 77 K and 4 K temperatures and found a slight increase in ILSS with reduced temperature. Further, Kumar et al. [30] probed the influence of cryogenic conditioning of woven carbon/epoxy laminates and found a reduction in ILSS at high fiber volume fraction.

NASA's Composite Overwrapped Pressure Vessel (COPV refer to Fig. 3.1(a)) is a well established cryogenic tank with metallic liner and continuous fiber/matrix system wrapped around it (refer to Fig. 3.1(b)). The main purpose of liner in cryogenic tanks is to prevent or minimize the permeation of cryogenic liquid through the walls of the external structure as well as minimize thermal stresses. Embrittlement in metallic liners and significant mismatch in coefficient of thermal expansion between liner and tank structure pose issues of microcracking in liner and delamination between the two [31]. Therefore, if an unlined composite tank structure is designed efficiently to prevent possible microcracking while maintaining the overall structural integrity will result in lightweight cryogenic tanks. **The overarching goal of the study conducted in this paper is to design cryogenic tanks without metallic liner or insulator, thus, further reducing the overall weight of the cryogenic tank while sustaining cryogenic temperatures and in-service mechanical loads.** Towards that end, the feasibility of using textile composites

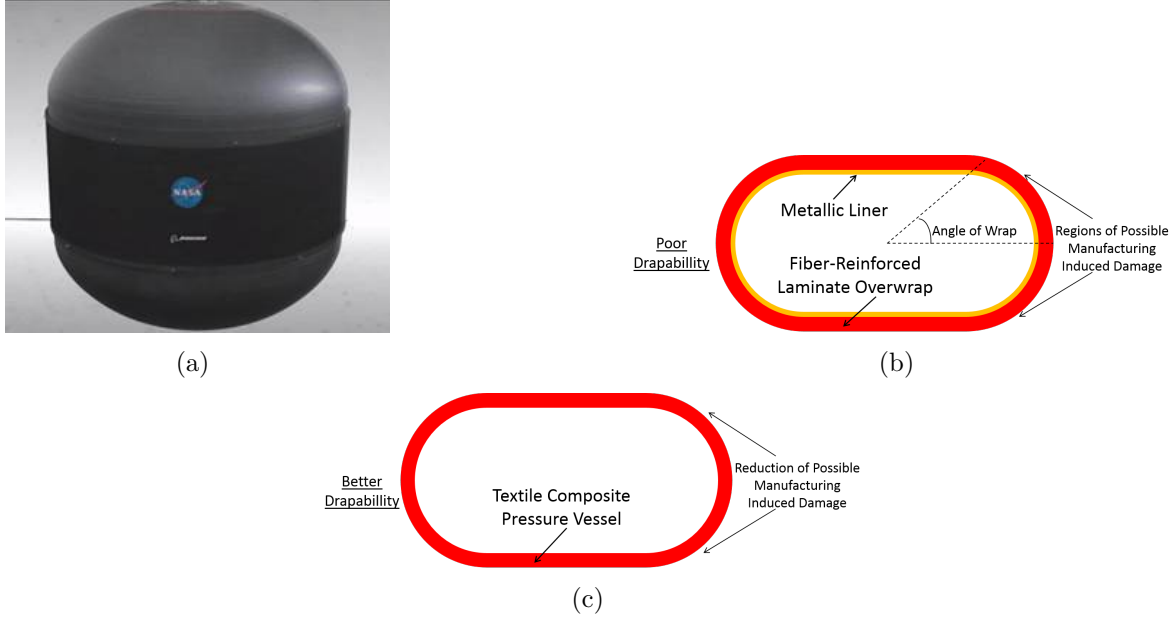


Figure 2.1: (a) NASA's Composite Cryogenic Fuel Tank, (b) Schematic of Fiber-Reinforced Laminate Overwrap and (c) Schematic of Textile Composite Pressure Vessel

was investigated in this paper. Textile composites have better drapability [10, 12], which would potentially result in smaller (localized) regions of damage that might occur around bends and edges in a pressure vessel (refer to Fig. 3.1(c)).

Designing unlined cryogenic composite tank materials is extremely challenging. The extreme temperature on the walls could result in damage in the material, thereby, reducing the safety and reliability of the tank. Failure modes, like delamination, transverse cracking, micro-buckling etc. within fiber reinforced laminates caused by the exposure to cryogenic temperatures may result in undesirable leakage and catastrophic failure [32]. That is, mismatch in the coefficient of thermal expansion between the layers and the interlaminar matrix region may initiate delamination between the layers. Further, the inter-tow matrix regions may experience stress concentration due to mechanical and thermal property mismatch, causing transverse micro-cracking within the layers of the composite. Therefore, it is extremely important to investigate the failure and damage behavior of such composites

subjected to cryogenic temperatures. Therefore, the focus of this paper is to explore the possibility of using textile composites for constructing cryogenic fuel tanks by unveiling their response to cryogenic exposure.

The influence of cryogenic exposure on the stiffness and strength of woven carbon and Kevlar[®] fiber reinforced composites each are experimentally investigated as potential materials for constructing unlined cryogenic tanks. The paper is divided into the following sections: Experimental procedure that includes the details on the manufacturing process, cryogenic exposure and mechanical testing methodology; Discussion of results from the mechanical tests; Pictographic analysis of the material post cryogenic exposure and mechanical testing, followed by conclusions.

2.2 Experimental Procedure

2.2.1 Material System

Dry fabrics of woven (plain weave) carbon fiber and Kevlar[®] fiber tows were used as reinforcement with Epon 862/ Epikure 9553 hardener as matrix material. The carbon and Kevlar[®] fabric were purchased from fibreglast.com and their properties are given in Table 3.6. The hardener was mixed with the resin at a ratio (weight) of 16.9:100 as recommended by the manufacturer.

Table 2.1: Fabric properties (fibreglast.com)

Properties	Carbon Fabric	Kevlar [®] Fabric
Warp Raw Material	3K-Multifilament Continious Tow	1140 denier Kevlar [®] 49
Filling Raw Material	3K-Multifilament Continious Tow	1140 denier Kevlar [®] 49
Weave Pattern	Plain Weave	Plain Weave
Warp Ends/Inch (approx.)	12.5±1.0	17
Fabric Areal Weight	5.4-5.9 oz/yd ²	5.3 oz/yd ²
Nominal Thickness	0.012 inches	0.011 inches

2.2.2 Manufacturing Process: Vacuum Assisted Resin Transfer Molding

Vacuum Assisted Resin Transfer Molding (VARTM) process is an advanced fabrication process for polymer-matrix textile composite structures. It is very cost effective to produce large scale composites while maintaining the quality of the final composite [9, 33, 34, 35, 36]. Fig. 2.2 provides an overview of the VARTM process. Dry fabric was first placed between two metal plates along with nylon release peel ply, flow media and breathers (refer to Fig. 2.2(a)). Since, woven fabric was used, there is no ply orientation associated with it. However, the layers were arranged such that the direction of tows in different layers were parallel to each other. The complete mold (Fig. 2.2(b)) was then enclosed in a vacuum bag and the preform was impregnated with resin through an inlet port and transferred into the preform by a pressure gradient induced by a vacuum pressure. The dry fabric preform were debulked under vacuum prior to resin infusion, and the resin was allowed to settle down until most bubbles were at the top of the mixing bowl. After infusing the resin, the mold was placed inside an oven for curing [9, 34, 37]. For the current material system, the resin was cured at room temperature for 24 hours. The manufactured laminate was transversely isotropic and the approximate fiber weight fraction for carbon and Kevlar[®] fiber was 37 % and 43 %, respectively. In the current study, the main objective was to explore the feasibility of these composites to sustain cryogenic temperatures overall. A future work will investigate the effect of temperature gradient through the thickness of the tank wall.

2.2.3 Exposure to Cryogenic Environment

The composite specimens were exposed to cryogenic environment by submerging them in a container (Fig. 3.12(a)) filled with liquid nitrogen (LN_2) at a temperature of -196°C (77 K). Although, the actual fuel to be stored in the tank might be liquid methane or oxygen, nitrogen was used because it is easier to handle and possesses temperature similar to the others in its liquid state. The test specimens were exposed to LN_2 for 6 hours, which is

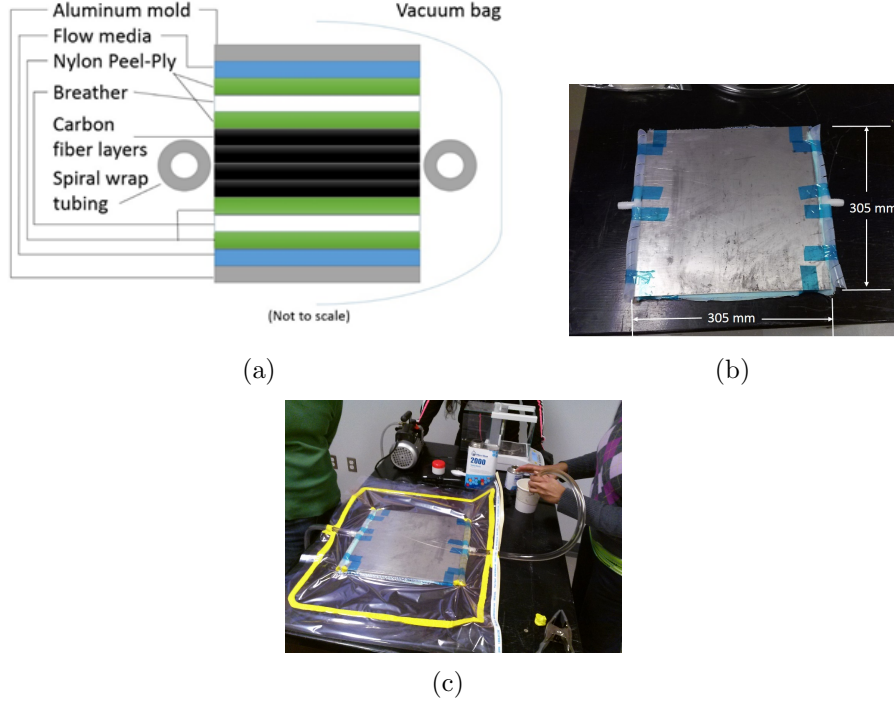


Figure 2.2: VARTM process: (a) Material Layup for the Mold; (b) Mold with Dry Fabric; (c) Vacuum Bag with Resin Infusion

approximately twice the time taken to fill up a X-33 liquid hydrogen tank [38, 39]. The specimens were then subjected to tensile and flexural loading after allowing them to return to room temperature upon removal from the cryogenic container. It is **hypothesized that the initial exposure to cryogenic environment would have an adverse effect on the stiffness and/or strength of the composite**. That is, the matrix tends to deform (shrink and harden) after cryogenic conditioning, but, is resisted by the stiff fibers causing residual stresses at the fiber/matrix interface resulting in transverse cracks and debonds.

2.2.4 Tensile Tests

Tensile tests on the two types of composites (carbon and Kevlar[®] reinforced) were conducted. A total of 16 samples (8 of each material type) were prepared for the tensile tests according to ASTM D3039 standard [40]. Tensile test specimens were cut parallel

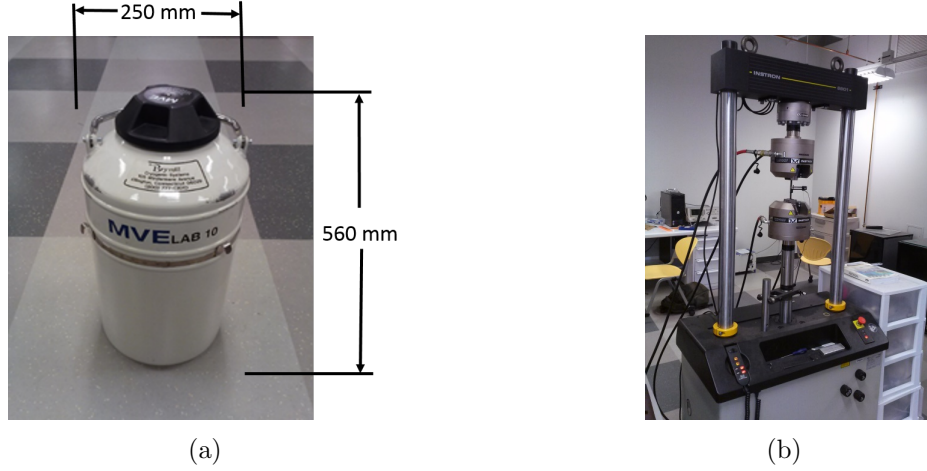


Figure 2.3: (a) Cryogenic Exposure Container; (b) Instron Test Frame

to the tow direction with the following dimensions: length 250 mm x width 25 mm x thickness 1.2 mm. During the test, specimens were loaded in the Instron 8801 Servohydraulic Fatigue Testing System (Fig. 3.12(b)) at a loading rate of 2 mm/min until failure. The load-displacement responses were determined for each case, and the corresponding tensile stress-strain responses were calculated using the area of cross-section and the gauge length (25 mm) of the extensometer (Instron 2620-601). Four specimens each of carbon and Kevlar[®] materials were tested as pristine and the other four were exposed to liquid nitrogen for 6 hours and then tested.

2.2.5 Flexural Test

Three-point bending tests were carried out on both carbon and Kevlar[®] composite specimen to determine the flexural properties of the composites. A total of 8 specimens (4 pristine and 4 cryogenic exposed) were tested for both carbon and Kevlar[®] fiber composites each according to ASTM D7264 standard [41]. Specimens were cut parallel to the tow direction and dimensions were: length 150 mm x width 13 mm x thickness for carbon composite was 3.3 mm and for Kevlar[®] composite was 4.33 mm. Three point bending tests were also carried out on the same Instron 8801 machine at a loading rate of 1 mm/min. A

constant span length to width ratio of 32:1 maintained for both types of composites that resulted in a span length of 105 mm and 138 mm for carbon and Kevlar[®], respectively. The total length of the specimen for Kevlar[®] fiber was less than the specified value in ASTM D7264. In order to calculate the flexural chord modulus of elasticity, strain range from 0.001 to 0.003 was selected from the stress-strain diagram as recommended in ASTM D7264 [41].

2.2.6 Short Beam Shear Test

Short Beam Shear (SBS) tests were conducted next to measure the Interlaminar Shear Strength (ILSS) of the composite. The total number of specimens tested were the same as mentioned in section 2.2.4 and 2.2.5. The specimens were prepared according to ASTM D2344 standard [42] with specimen dimensions of length 40 mm x width 12.36 mm x thickness 5.87 mm for carbon fiber and length 40 mm x width 12.81 mm x thickness 6.35 mm for Kevlar[®] fiber. SBS tests were also carried out on the same Instron 8801 machine with a loading rate of 1.0 mm/min.

2.3 Results and Discussion

Woven composites with carbon and Kevlar[®] fiber tows as stiffeners were investigated in this paper in order to understand their respective mechanical behaviors upon cryogenic exposure for 6 hours as mentioned in section 3.4.2. Results from the different experimental investigations mentioned above are discussed in this section. It should be noted that, tensile properties are fiber dominated, which implies that influence of degradation of matrix on tensile properties are not as evident as that on flexural properties. Flexural properties are matrix dominated, which means that the shear loading induced in the matrix in the compression region during flexural deformation of the composite acts as a catalysis for micro-buckling type failure in the fiber tows and splitting/delamination type failure along the load direction [43, 44]. Therefore, matrix degradation manifests itself at the composite

scale by reducing the flexural properties of a composite more compared to tensile properties. That is, due to the fiber dominated nature of tensile loading, minimal property loss would be expected from any delamination damage. Flexural and ILSS testing is much more sensitive to delamination damage that would typically result in a slight to moderate reduction in modulus and moderate to severe reduction in flexural strength.

2.3.1 Tension Test Results

As stated in Section 2.2.4, tension tests were conducted to determine and compare the material responses with and without cryogenic exposure. Fig. 2.4 displays the tensile chord modulus and tensile strength of both carbon and Kevlar[®] composites in both pristine and cryogenic conditions. It was observed that the cryogenic exposure does not have significant influence on the tensile chord modulus and ultimate tensile strength for both carbon and Kevlar[®] laminates which is summarized in Table 2.2. It was observed that the tensile chord modulus remains unaltered while the tensile strength reduced by 2.6 % (refer to Table 2.2) for carbon composite after cryogenic exposure. Whereas, the initial stiffness reduced by 4.5 % while the tensile strength reduced by only 1.7 % for Kevlar[®] composite.

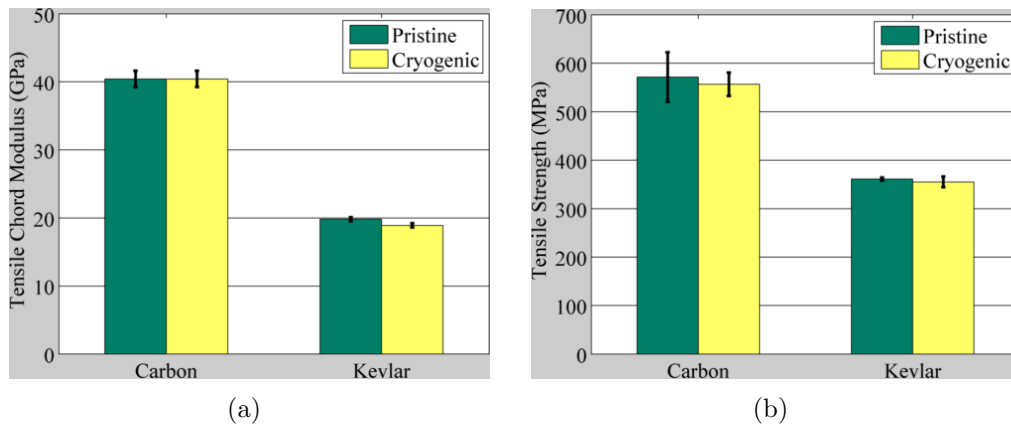


Figure 2.4: Bar Chart showing (a) Tensile Chord Modulus and (b) Tensile Strength for both Composites with Standard Deviation

Table 2.2: Tensile test results with standard deviation

Material	Condition	Tensile Chord Modulus (GPa)	% Reduction	Tensile Strength (MPa)	% Reduction
Carbon	Pristine	40.4 \pm 1.2	-	571 \pm 51	-
Carbon	Cryogenic	40.4 \pm 1.2	0	556 \pm 24	2.6
Kevlar [®]	Pristine	19.8 \pm 0.3	-	361 \pm 3	-
Kevlar [®]	Cryogenic	18.9 \pm 0.3	4.5	355 \pm 11	1.7

2.3.2 Flexural Test Results

Flexural response of the two types of composites upon exposure to cryogenic conditions is compared to pristine material response. Fig. 2.5 shows the flexural chord modulus and flexural strength of both carbon and Kevlar[®] composite from the 3-point bending test. It was observed from Fig. 2.5(a) and Fig. 2.5(b) that the flexural properties do not change significantly after cryogenic exposure. Table 2.3 summarizes the results from the flexural tests. The flexural chord modulus and strength reduced by 3.7 % and 3.5 %, respectively for carbon composite. Whereas, for Kevlar[®] composite, the flexural chord modulus and strength reduced by 1.2 % and 1.9 %, respectively.

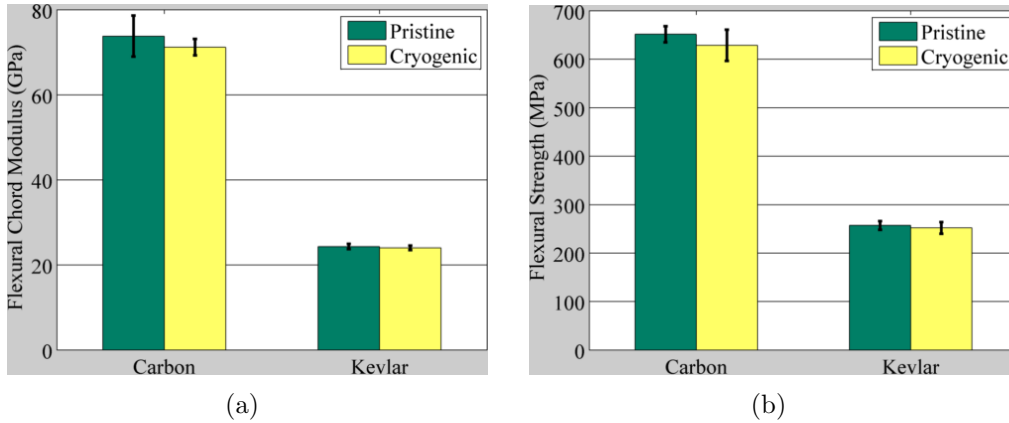


Figure 2.5: Bar Chart showing (a) Flexural Chord Modulus and (b) Flexural Strength for both Composites with Standard Deviation

Table 2.3: Three point bending test results with standard deviation

Material	Condition	Flexural Chord Modulus (GPa)	% Reduction	Flexural Strenth (MPa)	% Reduction
Carbon	Pristine	73.8 \pm 4.8	-	651.0 \pm 16.7	-
Carbon	Cryogenic	71.1 \pm 1.9	3.7	628.1 \pm 32.3	3.5
Kevlar [®]	Pristine	24.3 \pm 0.6	-	257.1 \pm 8.9	-
Kevlar [®]	Cryogenic	24.0 \pm 0.5	1.2	252.1 \pm 11.9	1.9

2.3.3 SBS Test Results

SBS tests were conducted to determine the ILSS of the composites. Fig. 2.6 shows the ILSS of both types of composites, where the ILSS values for carbon fiber composites do not change significantly after cryogenic exposure, while it reduced by 16.8% for Kevlar[®] fiber composites.

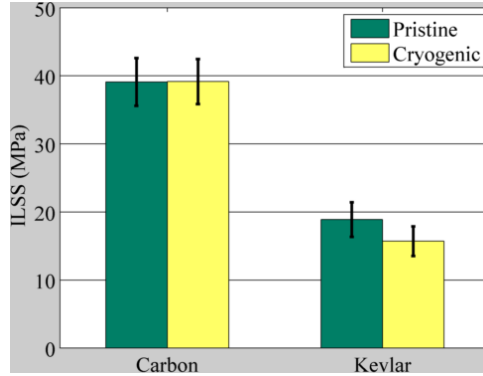


Figure 2.6: Bar Chart showing ILSS for both Composites with Standard Deviation

2.4 Pictographic Analysis

Further analysis of the samples exposed to cryogenic conditions followed by mechanical loading was conducted to explore the corresponding failure mechanisms. Carbon and Kevlar[®] composite samples (pristine and exposed) were analyzed using Scanning Electron Microscope (SEM). Figures 2.7 and 2.8 show the SEM (12 kV potenial and same condition

was used to take all the images) images of surfaces of carbon and Kevlar[®] composites of pristine and cryogenic exposed samples. Evidently, there were no growth or propagation of cracks in either case. There was hardly any surface matrix degradation observed and hence the figures look almost the same. Also, their failure modes were similar. The reduction in mechanical properties was negligible under tensile loading and within 4% under flexural loading as discussed in section 2.3.1 and 2.3.2.

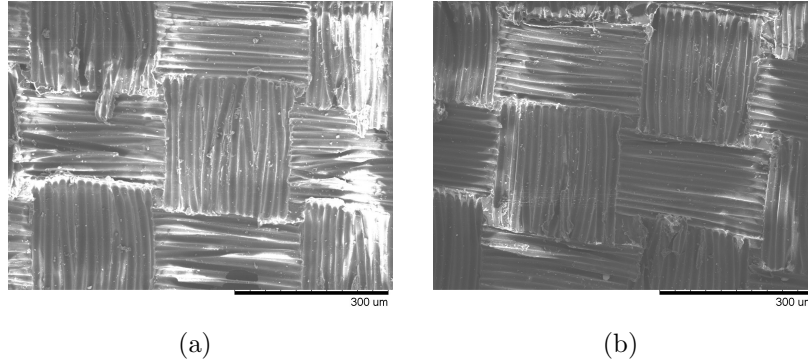


Figure 2.7: Scanning Electron Microscope (SEM) Images of Carbon Composite (a) at Room Temperature; (b) after Cryogenic Exposure

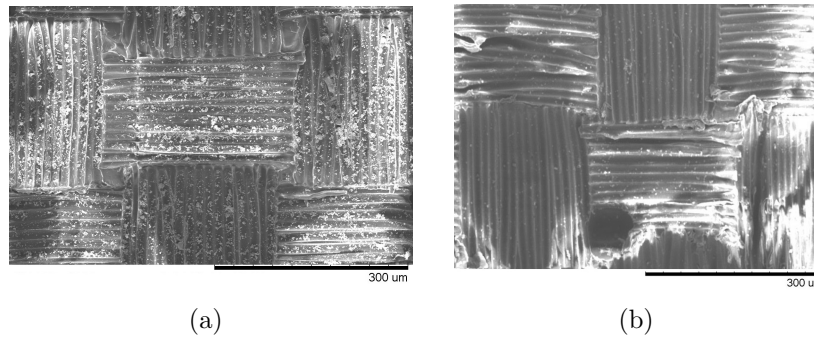


Figure 2.8: Scanning Electron Microscope (SEM) Images of Kevlar[®] Composite (a) at Room Temperature; (b) after Cryogenic Exposure

Microscopic analysis of the polished cross-section of the failed specimens from the flexural tests was conducted. Fig. 2.9(a) (pristine) and Fig. 2.9(b) (cryogenic exposed) show the optical microscope images of failed carbon specimen after 3-point bending test. It is

observed that failure patterns are similar in both the specimens that failed due to the formation of kink band under the loading point (region A on Fig 2.11) which is accompanied by fiber breakage of brittle carbon fiber tows. In the case of Kevlar[®] composite (Fig. 2.10), the specimens failed due to the formation of shear band with rotated Kevlar[®] fiber tows under the load point of the specimen (region A on Fig 2.11). The failure patterns remain unaltered in the pristine and cryogenic exposed specimen.

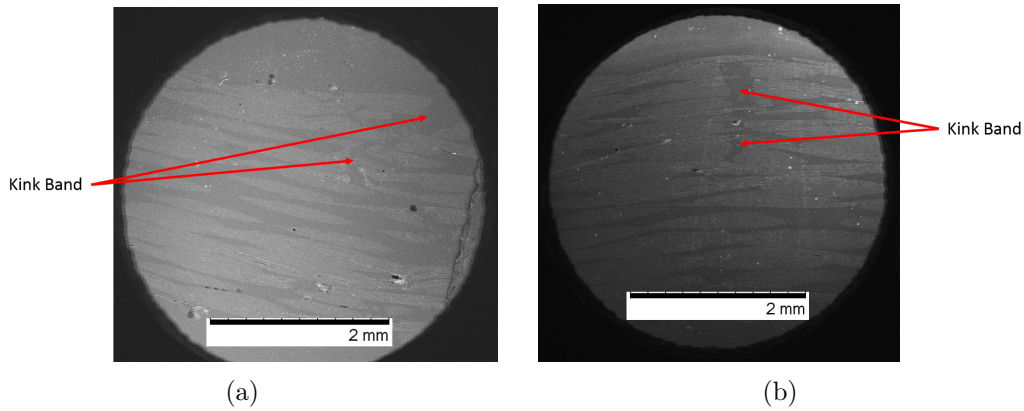


Figure 2.9: Optical Microscope Images of Failed Carbon Composite (a) at Room Temperature; (b) after Cryogenic Exposure

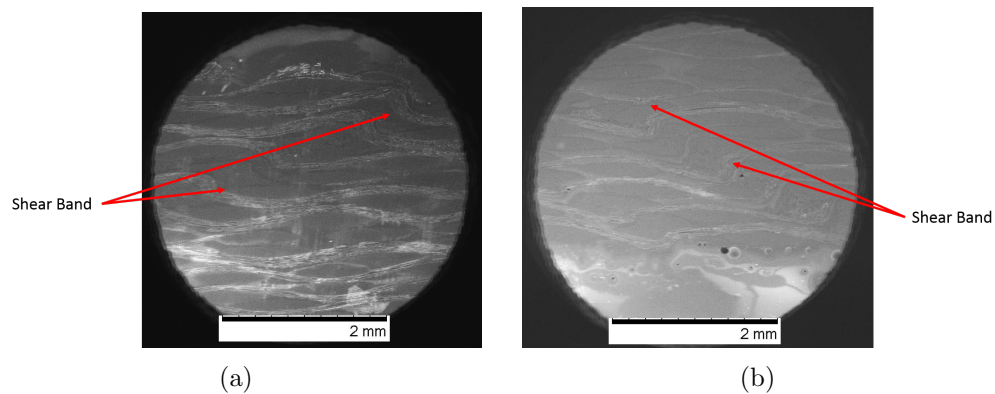


Figure 2.10: Optical Microscope Images of Failed Kevlar[®] Composite (a) at Room Temperature; (b) after Cryogenic Exposure

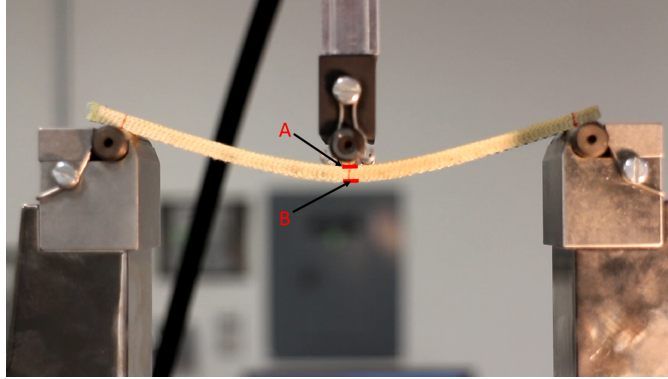


Figure 2.11: Three Point Bending Test of Kevlar[®] Fiber Specimen

2.5 Conclusions

Woven fiber reinforced (carbon and Kevlar[®]) composite materials exposed to cryogenic environment were investigated in this paper with the objective of using them in cryogenic propellant tanks. Tensile and flexural experiments were followed to determine the thermo-mechanical responses of Kevlar[®] and carbon composites. This preliminary study indicated that woven thermosetting composites could have a potential use in cryogenic tanks. Further research is required to examine if any failure mechanisms, like delamination effects, occur due to hoop and corner strains caused by expansion and contraction when a constrained tank is subjected to cryogenic environment. Smart design of these composites would allow for lighter, stiffer, tougher and damage resistant propellant tanks. However, there are other aspects like extended and gradient exposure to cryogenic conditions that need to be studied before a definite conclusion can be reached.

Chapter 3

Hybrid Textile Composites as Potential Cryogenic Tank Materials

Hybrid textile composites with carbon-Kevlar[®] fabric are explored in this chapter as means to reduce the through-thickness thermal gradient effect in cryogenic fuel tanks and enhance the material performance under cryogenic conditions. These tanks carry and store cryogenic propellants (oxygen, methane, hydrogen) at subfreezing temperatures in order to generate highly combustible liquids. The temperature gradient across the wall thickness is the result of an extremely cold temperature in its interior and ambient temperature on its external surface. Previous studies have indicated that carbon and Kevlar[®] textile composites are suitable materials for initial exposure to cryogenic temperatures (77 K), where the inter laminar shear strength (ILSS) of carbon composites decreased by a maximum of 3-4 % after cryogenic exposure and ≈ 17 % for Kevlar[®] composites. Computational models of hybrid carbon-Kevlar[®] composites are generated and subjected to cryogenic temperature, including gradient temperatures, for extended periods to investigate the influence of thermal gradient and optimize the design of layup stacking. Six hybrid combinations are selected that manifested low interface stresses and fewer number of peak stresses through the composite thickness. Computational and experimental work conducted here aided in determining optimum composite hybridization for cryogenic wall designs.

3.1 Introduction

Cryogenic tanks are commonly used to store extremely low temperature fluids, like liquid oxygen (-183°C), liquid methane (-161°C) or liquid hydrogen (-252°C) in their condensed

form in order to generate highly combustible liquids. This type of tank is generally composed of different layers of insulators and metal liners [3, 4] and is exposed to an extremely cold temperature in its interior and to ambient temperature on its external surface. A large temperature gradient across the thickness of the wall often cause differential expansion and contraction across the tank walls resulting in an uneven expansion or contraction of the material. The stresses caused by this differential expansion can exceed the strength of the material causing cracks to initiate and propagate in the direction of least resistance. In addition, if the boundaries of the material do not impede crack propagation, the tank's structure will ultimately fail resulting in an undesirable leakage [5] that can consequently lead to the catastrophic fuel tank failure in the case of a rocket or spacecraft being launched into space.

National Aeronautics and Space Administration (NASA) recently (August 2014) completed a major space technology development milestone by successfully testing a large pressurized composites cryogenic propellant tank [3]. The advancements made in the scope of composite materials have allowed for improvements in designs that were restrained in the past by a limited material selection. In the case of NASA, switching from metallic to composite construction has the potential to dramatically increase the performance capabilities of future space systems through significant reduction in weight [3, 4, 6]. The applications and benefits that could be derived from further developing composite materials for cryogenic applications are countless. It would be of paramount interest to design better composite structures using material systems like textile composites with superior structural [7, 8, 9, 10, 11, 12] and thermal properties compared to traditional laminates, as well as better draping compared to continuous fiber reinforced composites [10, 12]. Draping is the ability of woven textile fabric to conform to complex curved shapes. That is, regardless of the weave pattern, the fabric tows rotate freely to take the shape of the underlying structure [13]. Further, a study by Potter [14] on the influence of stretching/draping of various reinforcements, like woven fabric (textiles), unidirectional and cross-ply layers on complex geometry has shown that the slippage capability between tows in woven fabric

allows for more stretch/easy draping compared to others without applying undue force.

Previous research regarding the use of composite materials as cryogenic tank materials mainly dealt with thermal cycling of unidirectional composites, and their damage behavior and permeability under fatigue-thermal loads [15, 16, 17, 18, 19, 20, 21, 22, 23, 24]. Gong et al. [25] studied the mechanical properties of unidirectional E-glass fiber/epoxy and carbon fiber/epoxy laminates at cryogenic temperatures and Disdier et al. [26] studied helium permeation through woven E-glass fabric composites. Verstraete et al. [27] investigated hydrogen fuel tank with foam core and multilayer insulations (MLI) along with aluminum tank wall and composite fairing. Aceves et al. [28] explored aluminum-lined fiber wrapped cryogenic hydrogen storage tank at different temperature and pressure cycles. Shindo et al. [29] evaluated the interlaminar shear strength (ILSS) of G-10CR glass-cloth/epoxy laminates at room temperature, 77 K, and 4 K temperatures and observed a slight increase in ILSS with reduced temperature. Further, Kumar et al. [30] probed the influence of cryogenic conditioning of woven carbon/epoxy laminates and found a reduction in ILSS at high fiber volume fraction. In addition, Islam et al. [45] investigated the influence of cryogenic temperatures on carbon and Kevlar[®] fibers and found out that this fibers were suitable materials for initial exposure to cryogenic environment.

NASA's Composite Overwrapped Pressure Vessel (COPV refer to Fig. 3.1(a)) is a well established cryogenic tank with metallic liner and continuous fiber/matrix system wrapped around it (refer to Fig. 3.1(b)). The main purpose of liner in cryogenic tanks is to prevent or minimize the permeation of cryogenic liquid through the walls of the external structure as well as minimize thermal stresses. Embrittlement in metallic liners and significant mismatch in coefficient of thermal expansion between liner and tank structure pose issues of microcracking in liner and delamination between the two [31]. Therefore, if an unlined composite tank structure is designed efficiently to prevent possible microcracking while maintaining the overall structural integrity will result in lightweight cryogenic tanks. The overarching goal of the study conducted in this paper is to investigate the effect of cryogenic exposure on hybrid composites in order to design cryogenic tanks without metallic liner or

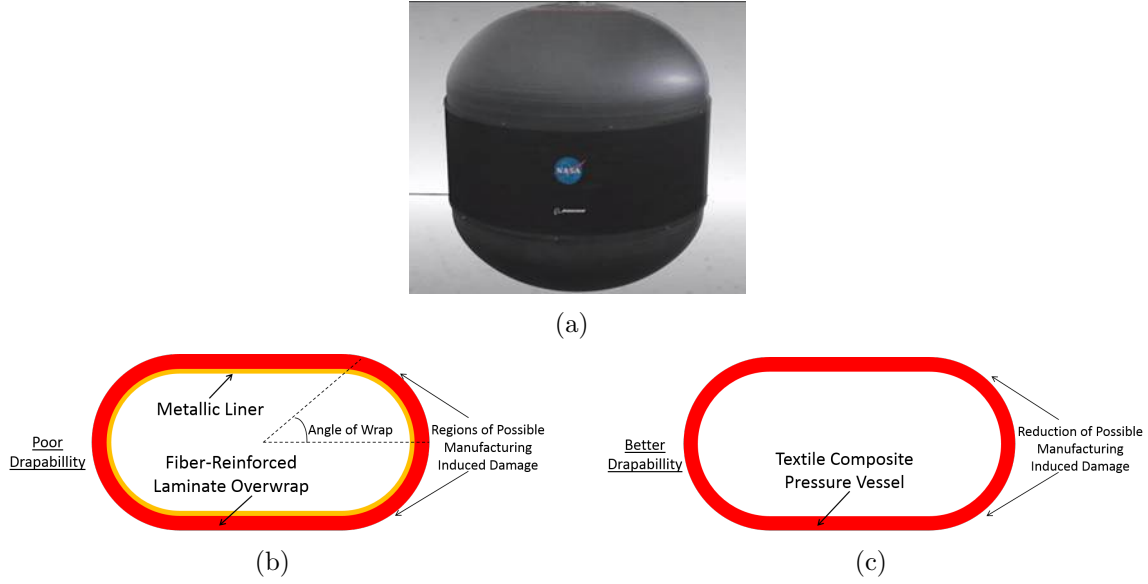


Figure 3.1: (a) NASA's Composite Cryogenic Fuel Tank, (b) Schematic of Fiber-Reinforced Laminate Overwrap and (c) Schematic of Textile Composite Pressure Vessel

insulator, thus, further reducing the overall weight of the cryogenic tank while sustaining cryogenic temperatures and in-service mechanical loads. Towards that end, hybridization of textile composites is investigated in this paper. Textile composites have shown better drapability [10, 12], which would potentially result in smaller (localized) regions of damage that might occur around bends and edges in a pressure vessel (refer to Fig. 3.1(c)).

Designing unlined cryogenic composite tank materials is extremely challenging. The extreme temperature on the walls could result in damage in the material, thereby, reducing the safety and reliability of the tank. Failure modes, like delamination, transverse cracking, micro-buckling, etc. within fiber reinforced laminates caused by the exposure to cryogenic temperatures may result in undesirable leakage and catastrophic failure [32]. Mismatch in the coefficient of thermal expansion between the layers and the inter laminar matrix region may initiate delamination between the layers. Further, the inter-tow matrix regions may experience stress concentration due to mechanical and thermal property mismatch, causing transverse micro-cracking within the layers of the composite. Therefore, it is extremely

important to investigate the failure and damage behavior of such composites subjected to cryogenic temperatures. Therefore, the focus of this paper is to experimentally validate and computationally explore the possibility of using hybrid textile composites for constructing cryogenic fuel tanks by unveiling their response to cryogenic exposure.

In this paper, the influence of gradient cryogenic exposure on the inter laminar shear strength (ILSS) of hybrid woven carbon and Kevlar[®] fiber reinforced composites are experimentally investigated as potential materials for constructing unlined cryogenic tanks. The hybridization process consists of an initial computational study of the influence of cryogenic exposure on the stress distribution on various hybrid combinations, which assists in selecting a few optimum layup designs, followed by experiments. The paper is divided into the following sections: Experimental procedure that includes the details of the manufacturing process, cryogenic exposure and mechanical testing methodology; Multi-physics computational modeling of composite layup hybridization exposed to cryogenic environment; Discussion of results from the mechanical tests on hybrid composites; Pictographic analysis of the material post cryogenic exposure and mechanical testing, followed by conclusions.

3.2 Levels of Hybridization

A preliminary study by Islam et al. [45] demonstrated that woven carbon and Kevlar[®] fiber composites have the potential to be used as cryogenic tank materials. The purpose of the hybridization process is to understand the response of hybrid composites exposed to uniform and gradient cryogenic environment. Towards that end, a 24 layer hybrid composite was considered for analysis with 5 different levels of hybridization based on the percentage of carbon reinforcement within a hybrid carbon/Kevlar[®] composite. 10 different layer combinations were design for each level of hybridization, except for the 100 percent combinations. Multiple computational models were generated to simulate and understand the behavior of different levels of hybridization. Table 3.1 shows the layer combinations

corresponding to each hybridization level. Fig. 4.1(b) shows a schematic of the cross-section of a laminate to elucidate the terminology used to describe layer combinations with an example of $[K6C6]_s$ laminate.

Table 3.1: Layer Combinations with Volume Fraction

100% Carbon	75% Carbon 25% Kevlar®	50% Carbon 50% Kevlar®	25% Carbon 75% Kevlar®	100% Kevlar®
C24	$[C3K3C6]_s$ $[C4K2C3KC2]_s$ $[C5K2C4K]_s$ $[C6K3C3]_s$ $[C9K3]_s$ $[K2C9K]_s$ $[K3C9K3C9]$ $[K3C9]_s$ $[K4C10K2C8]$ $[KCKCKC7]_s$	$[K6C6]_s$ $[C6K6]_s$ $[K4C6K2]_s$ $[C4K6C2]_s$ $[C3K2C2K4C]_s$ $[K3C2K2C4K]_s$ $[K4C7K8C5]$ $[K5C7K2C5K5]$ $[K4C5K2C]_s$ $[KCKCK4C4]_s$	$[K9C3]_s$ $[K6C3K3]_s$ $[K5C2K4C]_s$ $[K4C2K3CK2]_s$ $[K3C3K6]_s$ $[C4K10C2K8]$ $[C3K9]_s$ $[C3K9C3K9]$ $[C2K9C]_s$ $[CKCKCK7]_s$	K24

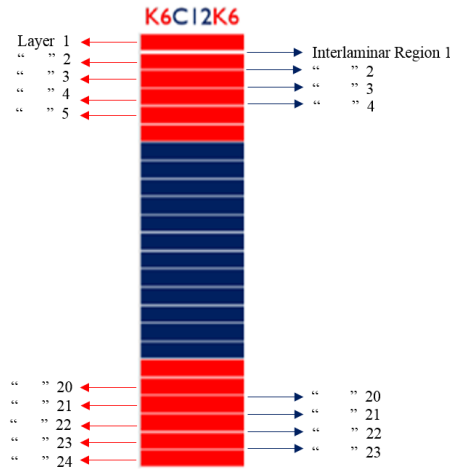


Figure 3.2: Cross Section of $[K6C6]_s$ Hybrid Composite

3.3 Computational Analysis for Hybridization Process under Cryogenic Exposure

Computational analysis was first conducted to determine the influence of cryogenic exposure on the development of stresses and possible damage incurred due to high thermal gradients through the wall thickness of a tank. The computational modeling framework was divided into the following two main steps: (1) Determine the temperature distribution in the model as a result of cryogenic exposure; (2) Determine the stress distribution in the model generated by the temporal and spatial temperature distribution. Thus, a heat transfer analysis was conducted first on a layered composite model to determine the temperature distribution upon cryogenic exposure. This was followed by a stress analysis with temperature distribution as an input to explore its influence on the stress distribution in the layers and at their interfaces. A schematic of the computational framework is shown in Fig. 3.3(a), which consists of the transient heat transfer model along with stress analysis.

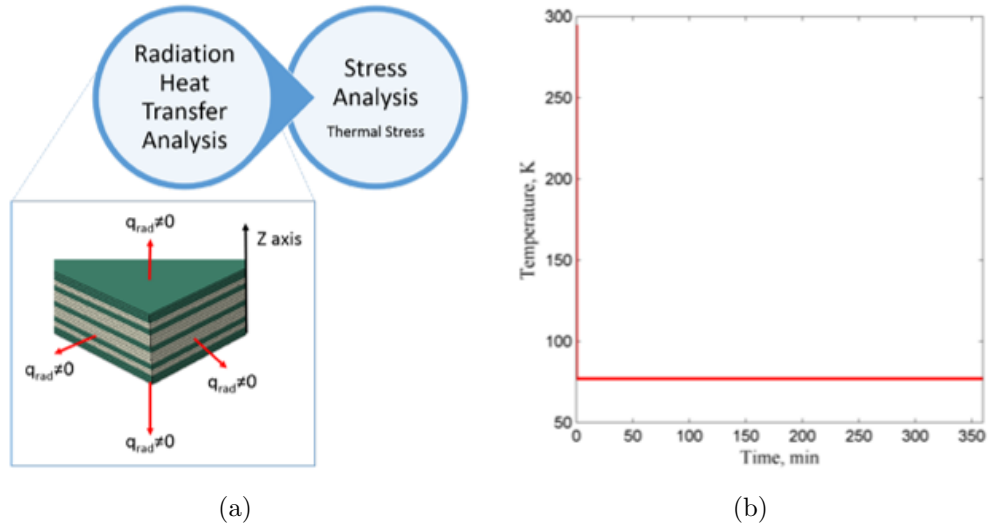


Figure 3.3: (a) Steps involved in the Computational Framework (b) Cryogenic Thermal Exposure of Hybrid Composites

3.3.1 Transient Heat Transfer Analysis

As will be explained in detail in the experimental section of this paper, the specimens were submerged in Liquid Nitrogen LN_2 for a period of 6 hrs. During the immersion process, the instantaneous change of temperature from room (295 K) to cryogenic (77 K) on the external surfaces of a specimen is represented as shown in Fig. 3.3(b). Therefore, the temperature distribution within the model was obtained after 5 minutes of cryogenic exposure in order to capture the thermal shock effect upon submersion into LN_2 .

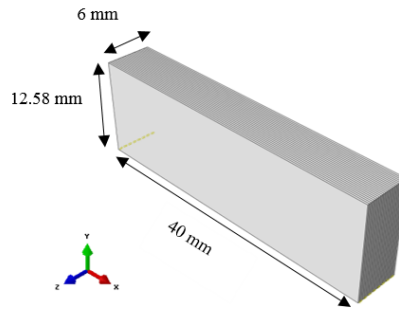


Figure 3.4: Hybrid Composite Model in ABAQUS

Fig. 3.4 shows a 3D model of a hybrid specimen with dimensions that consists of 24 homogenized reinforcement/matrix material layers. The entire model was initially prescribed to be at room temperature and then exposed to cryogenic temperature (77 K) on all external surfaces simulating instantaneous cryogenic exposure on its exterior as shown in Fig. 3.3. ABAQUS (a commercially available finite element software) was used to solve the transient heat transfer problem. Table 3.2 shows the thermo-physical properties of laminae or layers used in the computational model, which were calculated using rule of mixtures approach utilizing the fiber volume fraction of reinforcement in each layer.

Table 3.2: Thermo-Physical Properties of Carbon and Kevlar[®] Lamina

Properties	Carbon	Kevlar [®]
Conductivity, W/mK	3.106	0.139
Density, Tonnes/ mm^3	1.358×10^{-9}	1.29×10^{-9}
Specific Heat, mJ/tonnes K	1.085×10^9	7.41×10^8

3.3.2 Stress Analysis

Using the temperature distribution determined from the heat transfer analysis described in the previous section, the stresses developed due to cryogenic thermal distribution were determined for each model. Table 3.3 shows the mechanical properties of the carbon and Kevlar[®] fiber lamina or layers. Each layer of carbon and Kevlar[®] reinforcement in the model was assumed to be transversely isotropic in the plane of the composite with weaker through-thickness direction properties.

Table 3.3: Mechanical Properties of Carbon and Kevlar[®] Lamina

Properties	Carbon Fiber Lamina	Kevlar [®] Fiber Lamina
$E_{11}=E_{22}, GPa$	81.67	45.96
E_{33}, GPa	6.44	9.3
ν_{12}	0.37	0.37
$\nu_{13}=\nu_{23}$	0.53	0.33
G_{12}, GPa	2.7	3.8
$G_{13}=G_{23}, GPa$	2.1	3.5

Tables 3.4 and 3.5 show the coefficient of thermal expansions of Kevlar[®] and carbon lamina, respectively, which were calculated using the rule of mixtures. The carbon properties were obtained from [44] and Kevlar[®] properties from www.dupont.com.

Table 3.4: Coefficient of Thermal Expansion for Kevlar[®] Lamina

α_{11}, K^{-1}	α_{22}, K^{-1}	α_{33}, K^{-1}
7.4×10^{-6}	7.4×10^{-6}	4.0×10^{-5}

The stress distribution in the model after cryogenic thermal exposure of initial 5 minutes was examined for each hybrid composite. The model was free to deform upon thermal loading and the stresses along specified paths on the edges of the model were compared between different hybridization to make an informed choice for optimum combinations.

Table 3.5: Coefficient of Thermal Expansion for Carbon Lamina

Temperature, K	α_{11}, K^{-1}	α_{22}, K^{-1}	α_{33}, K^{-1}
90	1.68×10^{-6}	2.71×10^{-6}	1.61×10^{-5}
100	1.77×10^{-6}	2.73×10^{-6}	1.71×10^{-5}
120	1.89×10^{-6}	2.81×10^{-6}	1.91×10^{-5}
140	1.96×10^{-6}	2.9×10^{-6}	2.11×10^{-5}
160	1.92×10^{-6}	3.0×10^{-6}	2.29×10^{-5}
180	1.89×10^{-6}	3.11×10^{-6}	2.48×10^{-5}
200	1.92×10^{-6}	3.25×10^{-6}	2.65×10^{-5}
220	2.0×10^{-6}	3.41×10^{-6}	2.81×10^{-5}
240	2.13×10^{-6}	3.62×10^{-6}	2.97×10^{-5}
260	2.23×10^{-6}	3.9×10^{-6}	3.11×10^{-5}
280	2.28×10^{-6}	4.24×10^{-6}	3.24×10^{-5}
300	2.35×10^{-6}	4.18×10^{-6}	3.46×10^{-5}

3.3.3 Results from the Computational Study for Uniform Surface Cryogenic Exposure

Stress distribution along a specified path across layers of all hybrid combination of composites was determined. Fig. 3.6, Fig. 3.7, and Fig. 3.8 show the maximum principle stresses in the through-thickness direction along the path shown in Fig. 3.3.3 for all combinations of carbon and Kevlar[®] layered composites.

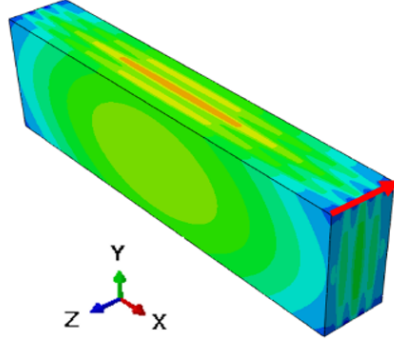


Figure 3.5: Cryogenic Thermal Exposure of Composites

Among the 30 combinations of hybrid laminates shown in Fig. 3.6, Fig. 3.7 and Fig. 3.8, six combinations shown in Fig. 3.9 were chosen for manufacturing and testing. Three of the selected combinations were chosen based on minimum peak stress values (Fig. 3.9(a))

and the other three were chosen based on minimum number of peak stresses along the chosen path (refer to Fig. 3.9(b)). The selection criteria for the chosen laminates was to understand the influence of the magnitude and quantity of peak stresses on the ILSS in composites subjected to cryogenic exposure. Fig. 3.9 incorporates the maximum principle stress distributions for C24 and K24 in order to compare the behavior of the selected laminates to the behavior of the laminates with just one material (100 % Kevlar[®] and 100 % Carbon).

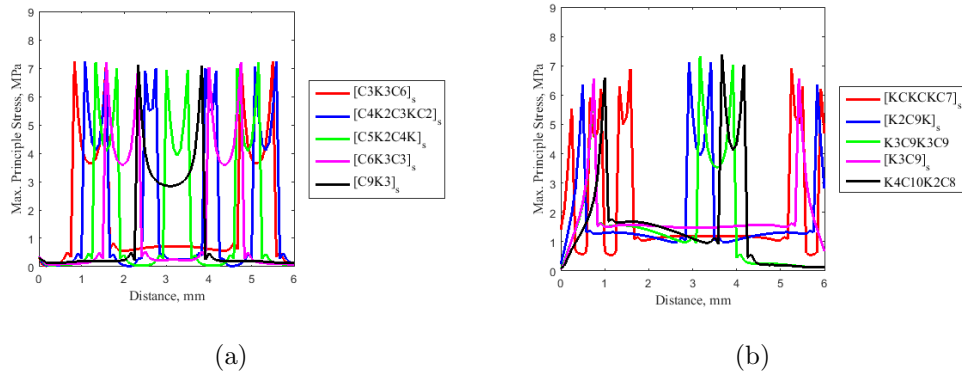


Figure 3.6: Maximum Principal Stress for 75% Carbon - 25% Kevlar[®]

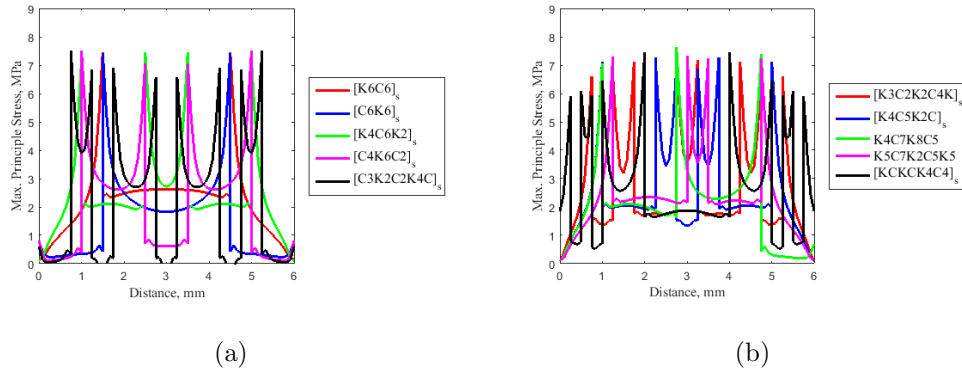


Figure 3.7: Maximum Principal Stress for 50% Carbon - 50% Kevlar[®]

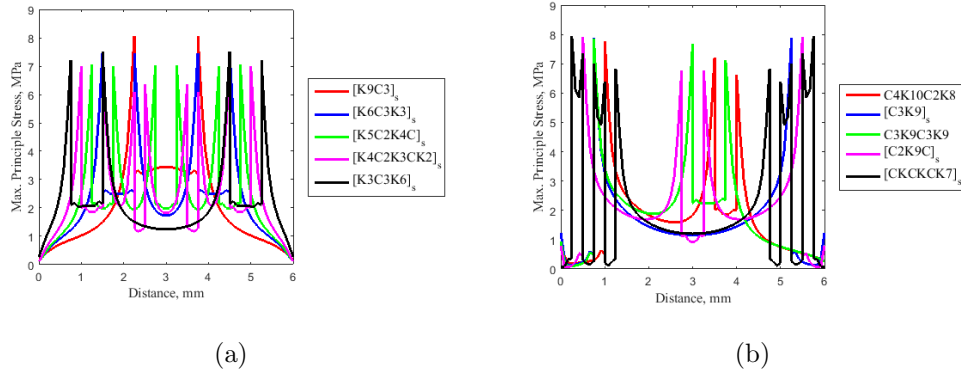


Figure 3.8: Maximum Principal Stress for 25% Carbon - 75% Kevlar[®]

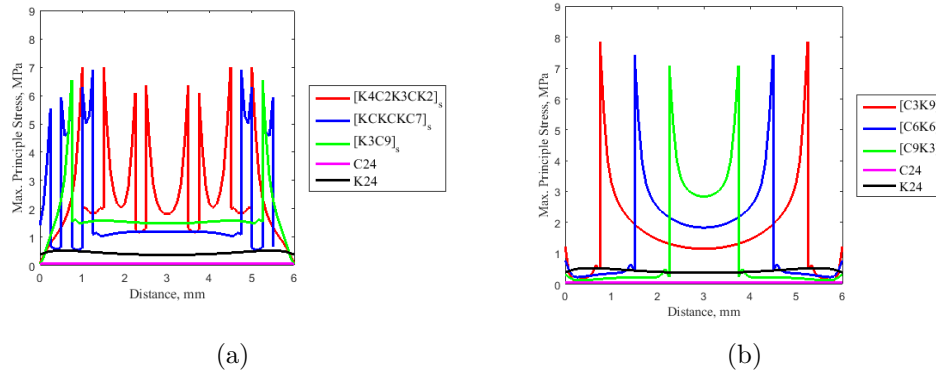


Figure 3.9: Hybrid Composite Based on (a) Minimum Peak Stress Values and (b) Minimum Number of Peak Values

3.3.4 Computational Stress Analysis with Interlaminar Matrix Layer

In order to understand the behavior of the interlaminar matrix, an additional computational model was created that consists of thin interlaminar matrix regions along with reinforcing lamina layers. The six selected combinations were simulated in ABAQUS and the results of the stresses developed by the cryogenic exposure are shown in Fig A.2. Heat transfer and stress analysis were conducted as described in the previous section with matrix layer properties shown in Table 3.7. From the plots displayed in Fig. A.2, a fairly uniform

distribution of stress is observed in all models except for the model with $[K4C2K3CK2]_s$ layup. This is attributed to a change in material distribution eight times within the layup, and expected to have a similar response as the one in Fig. 3.9(a), where eight stress peaks are observed. This simulation reveals the relative difference in stresses present in the model due to the change in layer and material properties through the thickness direction.



Figure 3.10: Schematic of Composite with Interlaminar Epoxy Matrix

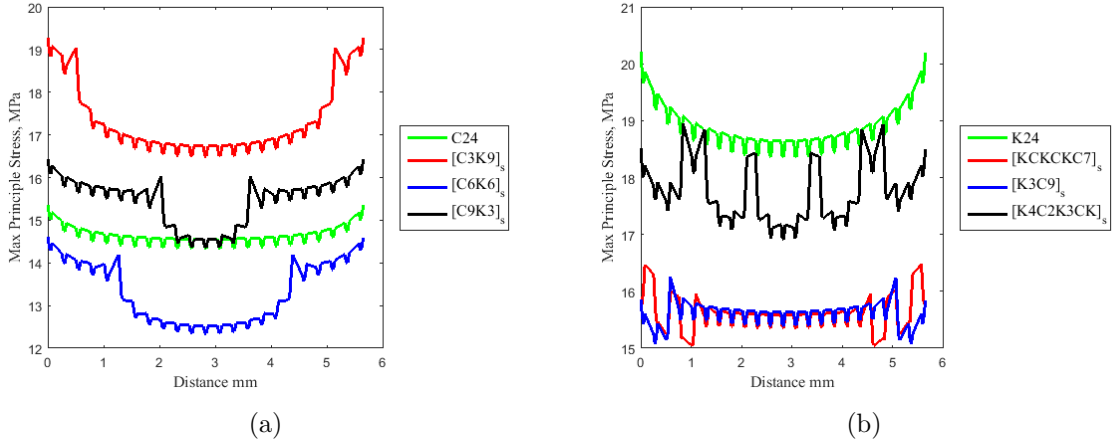


Figure 3.11: Maximum Principal Stress Computed in the Matrix Section for the Optimal Cases Mentioned in Fig 3.9.

3.4 Experimental Procedure

3.4.1 Manufacturing

Composite plates were manufactured using vacuum assisted resin transfer molding (VARTM) process, which is an advanced fabrication process for polymer-matrix textile composite

Table 3.6: Fabric Properties (fibreglast.com)

Properties	Carbon Fabric	Kevlar [®] Fabric
Warp Raw Material	3K-Multifilament Continious Tow	1140 denier Kevlar [®] 49
Filling Raw Material	3K-Multifilament Continious Tow	1140 denier Kevlar [®] 49
Weave Pattern	Plain Weave	Plain Weave
Warp Ends/Inch (approx.)	12.5±1.0	17
Fabric Areal Weight	5.4-5.9 oz/yd ²	5.3 oz/yd ²
Nominal Thickness	0.012 inches	0.011

Table 3.7: Epoxy Matrix Properties

Properties	Epoxy Matrix
E, GPa	4950
ν	0.375
Conductivity, W/mK	0.2
Density, Tonnes/mm ³	1.2 x 10 ⁻⁸
Specific Heat, mJ/tonnes K	1.7 x 10 ⁷
α_{11} , K ⁻¹	5.58 x 10 ⁻⁵

structures. It is very cost effective to produce large scale composites while maintaining the quality of the final composite [9, 33, 34, 35, 36]. Dry fabrics of woven (plain weave) carbon fiber and Kevlar[®] fiber tows were used as reinforcement with Epon 862/ EPIKURE 9553 hardener as the matrix material. Carbon and Kevlar[®] fabric were purchased from fibreglast.com and their properties are given in Table 3.6. The hardener was mixed with the resin at a ratio (weight) of 16.9:100 as recommended by the manufacturer.

3.4.2 Exposure to Cryogenic Environment

Composite specimens were exposed to cryogenic environment by submerging them in a 10 L dewar (Fig. 3.12(a)) filled with liquid nitrogen (LN_2) at a temperature of -196°C (77 K). Although, the actual fuel to be stored in the tank might be liquid methane or oxygen, nitrogen was used due to reduced handling and possessing difficulties compared to others in their liquid state. The test specimens were exposed to LN_2 for 6 hours, which is approximately twice the time taken to fill up a X-33 liquid hydrogen tank [38, 39]. The specimens were then subjected to flexural loading after allowing them to return to room

temperature upon removal from the cryogenic container. It is hypothesized that the initial exposure to cryogenic environment would have an adverse effect on the stiffness and/or strength of the composite. That is, the matrix tends to deform (shrink and harden) after cryogenic conditioning, but, is resisted by the stiff fibers causing residual stresses at the fiber/matrix interface resulting in transverse cracks and debonds.

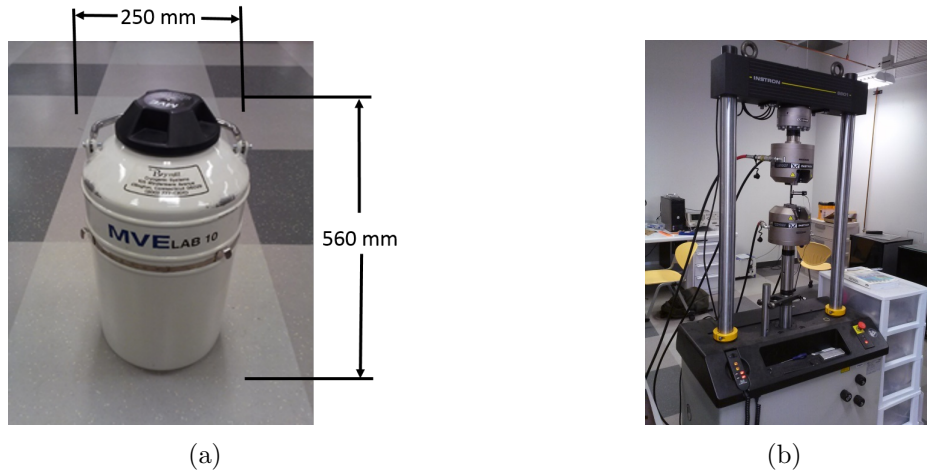


Figure 3.12: (a) Cryogenic Exposure Container; (b) Instron Test Frame

3.4.3 Short Beam Shear Test

Short Beam Shear (SBS) tests were conducted next to measure the Inter Laminar Shear Strength (ILSS) of the hybrid composite. A total of 15 (5 for Pristine, 5 for Uniform Cryogenic Exposure, and 5 for Gradient Exposure) specimens were tested in accordance to ASTM D2344 standard [42] with specimen dimensions of 40 mm long x 12.36 mm wide x 5.87 mm thick for carbon composites and 40 mm long x 12.81 mm wide x 6.35 mm thick for Kevlar[®] composites. SBS tests were conducted on Instron 8801 machine at a loading rate of 1.0 mm/min. Results of the SBS tests are discussed in section 3.6.

3.5 Computational Analysis of Gradient Cryogenic Exposure

An additional computational model was created with cryogenic exposure on one of the surfaces of the specimens with the other surfaces insulated in order to simulate the differential temperature across a tank wall. Such a gradient exposure can cause differential expansion or contraction across the tank wall. The stress distribution was computed in each model to identify the layups that display lower stress concentration along the through-thickness direction of the composite. Fig. 3.13 shows the direction of gradient exposure along the thickness of the hybrid composite, along which the thermal stresses were computationally determined.



Figure 3.13: Schematic of Gradient Exposure in a Hybrid Composite

3.5.1 Temperature Distribution

Figure 3.14(a) displays the temperature profiles of the selected hybrid composites after gradient cryogenic exposure. The temperature distribution for the hybrid composites lie within that of the C24 and the K24 composites. The composites that performed better are $[C3K3C6]_s$ and $[KCKCKC7]_s$, which had low volume percentage of Kevlar[®] fiber. The effect of thermal shock is more pronounced in Kevlar[®] compared to that observed in carbon due to the thermal properties of Kevlar[®]. The nodal temperature distribution in the computational domain obtained in this step was then used as an input to the thermal stress analysis next to determine the stresses caused by gradient exposure.

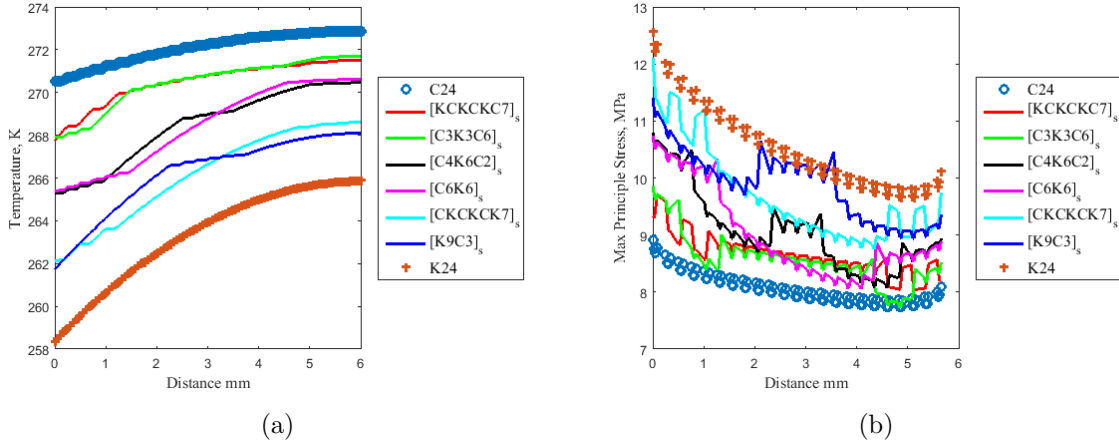


Figure 3.14: (a) Temperature Distribution of the Composites after Gradient Exposure (b) Stress Distribution of the Composites after Gradient Exposure

3.5.2 Stress Distribution

Figure 3.14(b) shows the thermal stress distributions of the hybrid composites after gradient cryogenic exposure, where [C3K3C6]_s and [KCKCKC7]_s composite appear to display the best overall behavior. This result is in correlation with the thermal distribution shown in Fig. 3.14(a) that displayed a favorable response for the hybrid composites with only 25 % Kevlar[®] compared to other levels of hybridization. The thermal stress distribution along the thickness direction is lower for the composites that experience a lower thermal shock effect and vice versa.

3.5.3 ABS Plastic Holder Computational Design and Manufacturing

Based on the suggestions from the computational models, experiments to corroborate the selection of optimum designs of hybrid composites were conducted, which is explained in detail in Section 3.6. An ABS plastic insulating holder was computationally designed as shown in Fig. 3.15(a) and 3D printed to hold the specimens during gradient exposure to

LN_2 . A total of eight composite layups were exposed to LN_2 using the plastic holder to study their response to gradient cryogenic exposure.

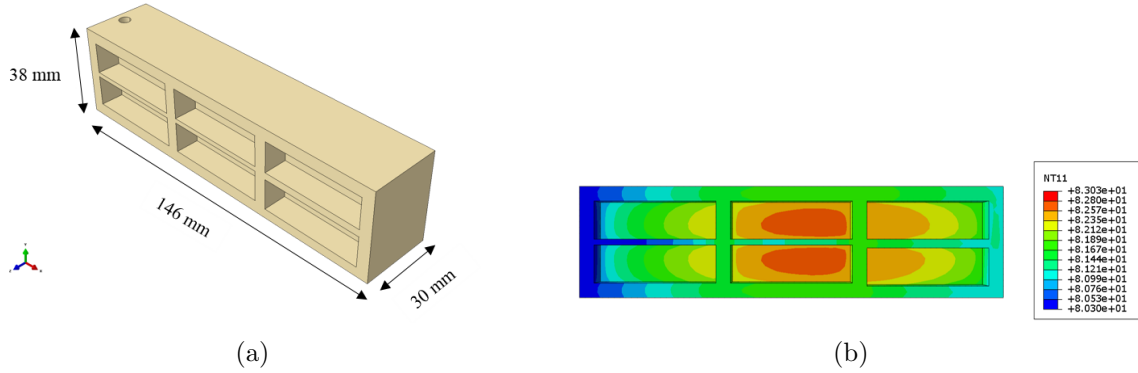


Figure 3.15: (a) ABS Plastic Holder Model (b) Temperature Distribution Inside the Plastic Holder

The ABS composite holder was virtually subjected to cryogenic environment in order to computationally determine the nodal temperature distribution, which displayed the areas of the plastic holder where the temperature was close to 77 K. The main purpose of the plastic holder is to isolate five of the six surfaces of the composite and allow the cryogenic exposure on one surface only. Fig. 3.15(b) shows the computed temperature profile on the plastic holder based on a simulation of cryogenic exposure for 6 hours, where the lowest temperature was approximately 80 K without any additional insulation material. The plastic holder was manufactured using fused deposition modeling (Fig. 3.16(a)) and the specimens were further insulated as shown in Fig. 3.16(b).

The plastic holder was further covered with an extra layer of tape in order to ensure that the temperature will remain as expected from the simulation. The hybrid composites were then positioned in the openings and attached into the plastic holder using a sealant tape as shown in Fig. 3.16(b). A total of 8 combinations (including C24 and K24) were exposed to gradient cryogenic environment using the plastic holder as previously described. The thermal gradient exposure lasted for 6 hours and the steps followed are represented in Fig. 3.17.

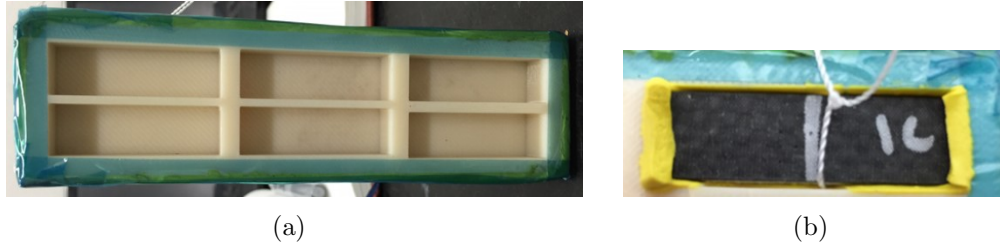


Figure 3.16: (a) ABS Holder After Layers of Insulation (b) Final Hybrid Composite Position

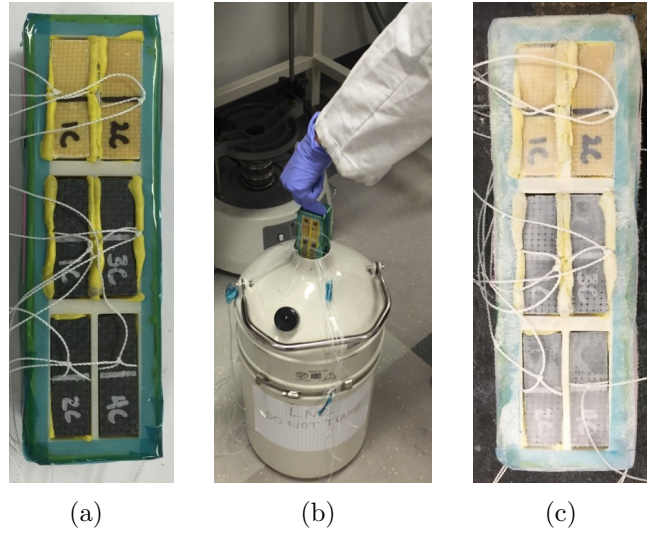


Figure 3.17: (a) ABS Holder Before Cryogenic Exposure (b) Liquid Nitrogen Exposure (c) ABS Holder After Gradient Cryogenic Exposure

3.6 Experimental Study of Gradient Cryogenic Exposure on Composites

Short Beam Shear (SBS) tests were conducted to determine the ILSS of the composites. 8 combinations from the 5 levels of hybridization were examined for room temperature, uniform cryogenic and gradient cryogenic exposures. It was observed in Fig. 3.18 that the ILSS of the composites decreases with decreasing volume percentage of carbon fiber

in the composite. The comparison of 8 different composite layups is divided into one 100 % carbon, two 75% carbon- 25% Kevlar[®], two 50% carbon-50% Kevlar[®], two 25% carbon- 75% Kevlar[®] and one 100% Kevlar[®]. The 50% carbon-50% Kevlar[®] hybridization displayed a deficient performance compared to the other hybridized composites.

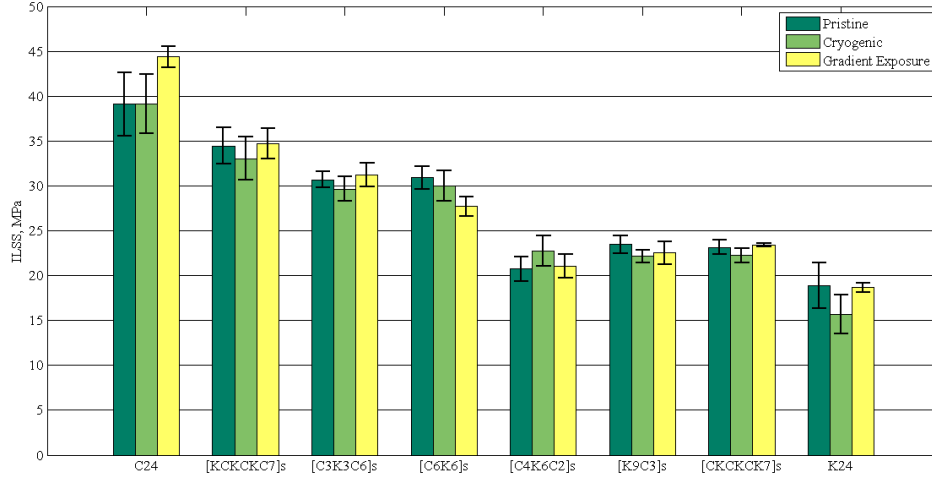


Figure 3.18: ILSS for the Hybrid Composites under Different Conditions

On the contrary, the 75% carbon- 25% Kevlar[®] [KCKCKC7]_s hybridization displayed the highest ILSS of 33-35 MPa in comparison to all the other combinations, including [C3K3C6]_s from the same hybridization level that exhibits an ILSS of 29.7- 30.7 MPa. The difference between [KCKCKC7]_s and [C3K3C6]_s hybrid composites is merely the layer stacking, where [KCKCKC7]_s laminate has more alternating material layers. The SBS tests reveal that [C3K3C6]_s composite showed delamination type failure in interlaminar region 17 between layers 18 and 19, while [KCKCKC7]_s composite did not exhibit any delamination type failure. Lastly, the two 25% carbon- 75% Kevlar[®] behaved poorly with a low ILSS compared to other hybridized composites. Based on the SBS test results, it can be concluded that a volume fiber percentage of 75% carbon- 25% Kevlar[®] with alternating distributed material layups away from the neutral axis of the composites will be most effective in mitigating the adverse effects of cryogenic temperatures on the ILSS

of a composite.

3.7 Fractographic Analysis of Gradient Exposed Hybrid Composites

Fractographic analysis of different hybridization levels after gradient exposure was performed on fractured surfaces to understand the failure mechanisms associated with cryogenic hybrid composite materials. The analysis corroborated the selection of the optimal hybrid composite with the highest volume percentage of carbon fiber for cryogenic fuel tanks. Fiber kink banding and delaminations can be observed in non hybridized composites in Fig. 3.20 and for hybrid composites in Fig. 3.21, Fig. 3.22 and Fig. 3.23. The interlaminar regions mentioned in the following sections are shown in Fig. 4.1(b). Furthermore, Fig. 3.19 displays typical load-deflection responses for each composite, where the results are favorable towards a higher volume percentage of carbon fiber. The peak load sustained by K24 was $\approx 50\%$ as compared to C24.

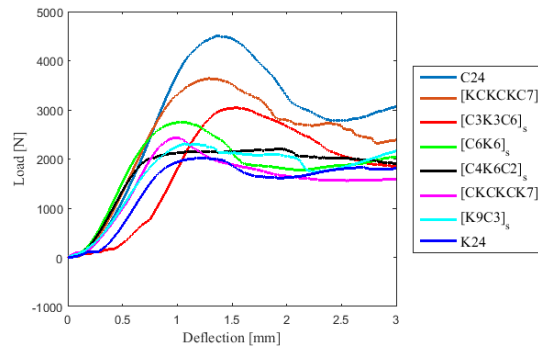


Figure 3.19: Load vs Deflection curves for the Hybrid Composites after Gradient Exposure

3.7.1 100 % Carbon and 100 % Kevlar®

Fig. 3.20 displays the failure mechanisms for C24 and K24 laminates after gradient exposure. Kink band formation can be observed in Fig. 3.20(a) for C24 in the region where the load was applied, which appears to extend through all layers of the composite. Kink band is accompanied with fiber breakage between interlaminar regions 5 and 15 as denoted by Fig. 3.20(a). On the contrary, the K24 composite performed the poorest among all the composites, which exhibits delamination type failure after ≈ 2000 N of load as shown in Fig. 3.20(b). Severe damage occurred at interlaminar regions 6, 7 and 8 with total separation of the layers.

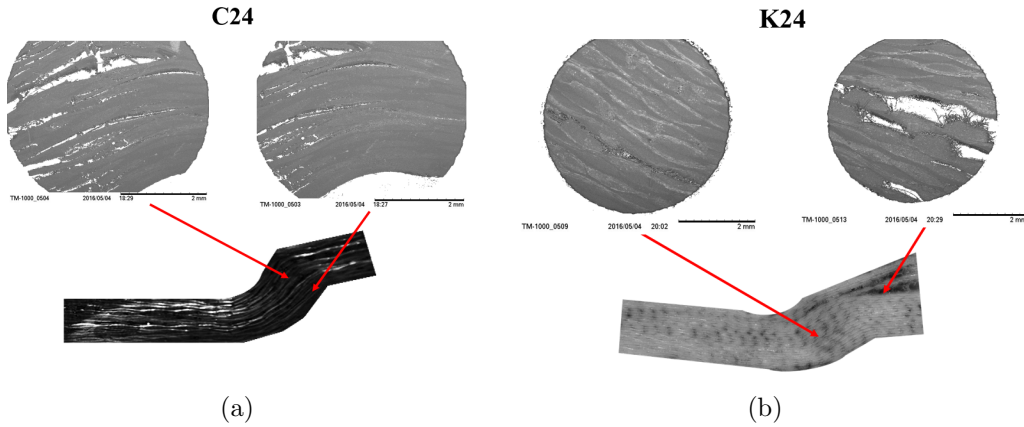


Figure 3.20: (a) C24 Fractographic Analysis (b) K24 Fractographic Analysis

3.7.2 75 % Carbon - 25 % Kevlar®

Fig. 3.21 displays the failure patterns of $[KCKCKC7]_s$ and $[C3K3C6]_s$ after gradient exposure. Composite $[KCKCKC7]_s$, which is the optimal hybridization based on the results from section 3.6 displayed a similar failure mechanism to C24 laminate mentioned in section 3.7.1. Kink band formation with minimal fiber separation between interlaminar regions 12 and 13 is observed as shown in Fig. 3.21(a). This hybrid combination sustained the second highest load before failure, and the damage in the fibers is insignificant compared to other

hybridization levels described in sections 3.7.3 and 3.7.4. Composite $[C3K3C6]_s$ exhibits delamination type failure in the interlaminar regions, where the material changes from carbon to Kevlar[®]. A peak load of 3000 N is observed beyond which the material completely debonds at the interfaces where the material layers alternate. Both composites with 75 % Carbon - 25 % Kevlar[®] combination performed the best as compared to other hybridizations; however $[KCKCKC7]_s$ was selected as the optimal case due to the desirable failure mechanism and performance under gradient cryogenic exposure.

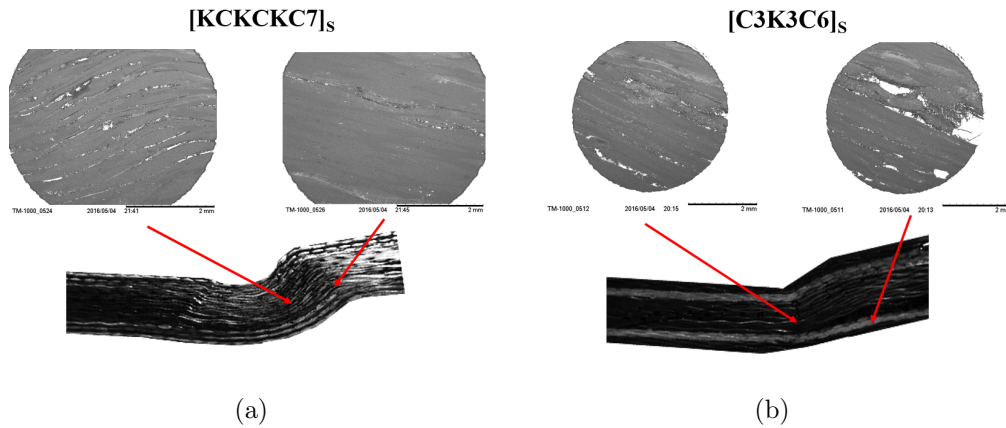


Figure 3.21: (a) $[KCKCKC7]_s$ Fractographic Analysis (b) $[C3K3C6]_s$ Fractographic Analysis

3.7.3 50 % Carbon - 50 % Kevlar[®]

Fig. 3.22 displays the failure mechanisms for $[C6K6]_s$ and $[C4K6C2]_s$ composites after gradient cryogenic exposure. Composite $[C6K6]_s$ exhibits fiber breakage and delamination at the interlaminar regions 5 and 18 where a material change occurs as shown in Fig. 3.22(a), and sustained a peak load of 2800 N. Similarly, composite $[C4K6C2]_s$ exhibits severe delamination at interlaminar region 3 and minor damage between interlaminar regions 5 and 9 where Kevlar[®] fiber is present beyond 2200 N of load.

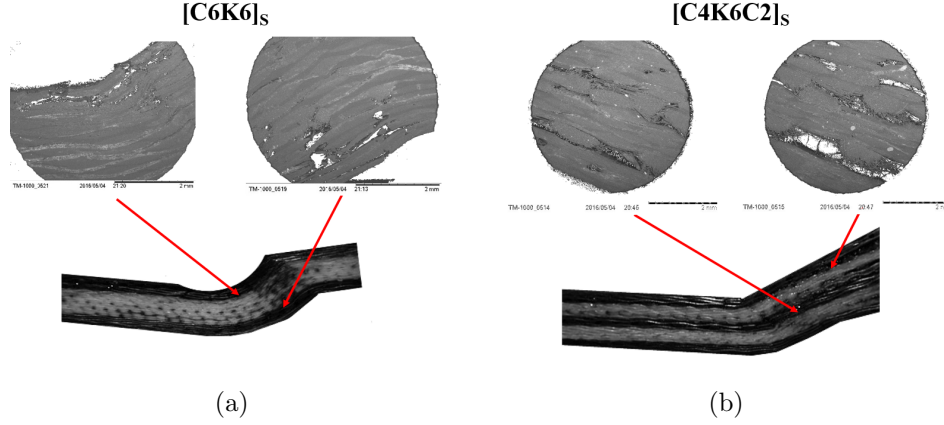


Figure 3.22: (a) [C6K6]_s Fractographic Analysis (b) [C4K6C2]_s Fractographic Analysis

3.7.4 25 % Carbon - 75 % Kevlar[®]

Fig. 3.23 displays the failure mechanism for [CKCKCK7]_s and [K9C3]_s composites after gradient exposure. Composite [CKCKCK7]_s exhibits kink band formation as shown in Fig. 3.23(a). Minor delamination and fiber breakage is present between interlaminar region 6 and 13, where majority of the Kevlar[®] fiber layers are present in the composite. This layer combination failed after a load of ≈ 2400 N and the critical regions are at the higher Kevlar[®] fiber concentrations, which are susceptible to delamination type failure as shown in Fig. 3.20(b). Lastly, [K9C3]_s laminate exhibits severe delamination type failure at the interlaminar region 15 accompanied with fiber breakage, where there is a change in material from carbon to Kevlar[®] fiber. After discussing the different failure types and their load carrying capacities for the hybridizations considered, the 25% Carbon - 75% Kevlar[®] hybridizations are deemed as not desirable for cryogenic fuel tanks.

3.8 Conclusions

Woven carbon and Kevlar[®] fiber reinforced hybrid composites exposed to cryogenic environment were computationally and experimentally investigated in this paper. Transient heat transfer analysis followed by mechanical stress analysis were conducted on different

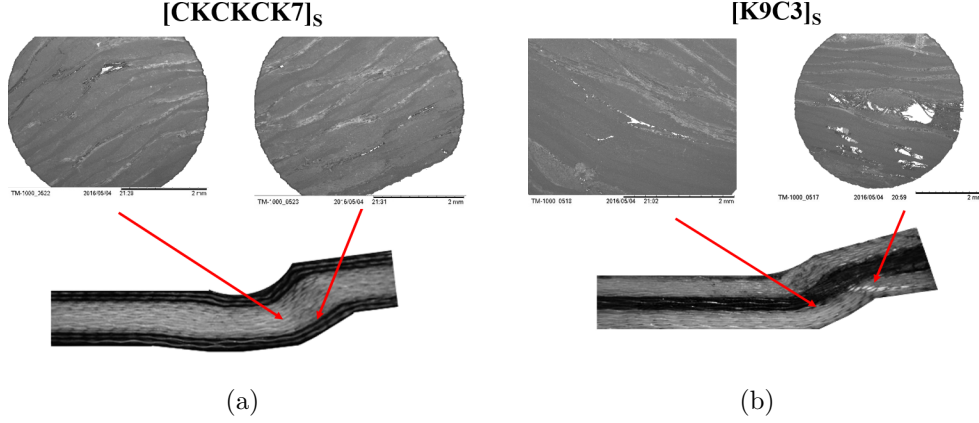


Figure 3.23: (a) [CKCKCK7]_s Fractographic Analysis (b) [K9C3]_s Fractographic Analysis

layer percentages and layer combinations of hybrid composites. Six combinations from the thirty combinations initially investigated were chosen for experimental testing along with 100% carbon and 100% Kevlar[®] fiber composites. Experiments were conducted for 100% carbon and 100% Kevlar[®] fiber composites, which revealed that there was an insignificant reduction in ILSS values for carbon composite, whereas, a reduction of 16.8% was observed for Kevlar[®]. The selected hybrid combinations were then computationally and experimentally investigated for cryogenic and gradient cryogenic exposure. Further, Short Beam Shear (SBS) tests were conducted to determine the ILSS of the composites and confirm the optimum hybrid composites that have been chosen based on computational modeling. 8 combinations were examined for Pristine, Cryogenic, and Gradient Exposure. It was observed that the overall ILSS tend to decrease with increasing volume percentage of Kevlar[®] fiber or decreasing volume percentage of carbon fiber in the composite. Further, the failure mechanisms are favorable towards a high concentration of carbon fiber in the levels of hybridization, making the 75% Carbon - 25% Kevlar combination [KCKCKC7]_s an optimum hybrid combination.

Chapter 4

Novel Model for Free Edge Effects in Laminates under Thermo-Mechanical Loading

In this chapter, a Quasi-2D plane strain formulation capable of predicting interface stresses is developed, which is implemented within the finite element method framework. The analysis of free edge stresses of composite laminates subjected to uniform axial loading and/or thermal loading are conducted. The simplified modeling approach is validated by comparing the predicted interlaminar stresses with previously published results and 3D analysis, which have shown excellent correlation. Thus, the framework presented here can be used as a computational tool to efficiently predict the interlaminar stresses of different laminates subjected to thermo-mechanical loading, which can assist in determining key interlaminar regions susceptible to free edge delamination.

4.1 Introduction

Interlaminar regions in polymer based layered carbon fiber composites are the critical regions that are most susceptible to delamination under static and dynamic loading. Mechanical response to load types like edge-wise and through-thickness compression, bending, and dynamic impact on layered composites is influenced by interlaminar strength and toughness, the geometry and the extent of loading. Debonding or delamination is observed to be a significant failure mechanism in layered composites with considerable visible damage. Significant localized interlaminar stresses occur at the free edges of laminated composite materials due to mismatch in property between plies, which is referred to as the “free edge

effect” [46]. Accurate determination of stress distribution near the free edges is very important due to their significant impact on delamination or transverse cracking. Stress state near the free edge is three dimensional in nature and classical lamination theory (CLT) is unable to determine these stresses accurately [46, 47]. Therefore, various analytical and numerical approaches such as finite difference, finite element, closed form analytical approach, boundary layer theories and layer-wise theories have been used to calculate the interlaminar stresses near the free edges.

Puppo and Evensen [48] proposed the first analytical method to determine the interlaminar stresses in a composite laminate. Pagano [49] developed a higher order plate theory to evaluate the interlaminar stresses. Few other analytical methods are: Perturbation method by Hsu and Herakovich [50]; Boundary layer theory by Tang [51], Davet and Destuynder [52], and Lin and Ko [53]; An approximate elasticity solution by Pipes and Pagano [54]; Variational principle by Pagano [55], Lekhnitskii and Fern [56]; Stress potential method by Wang and Choi [57, 58, 59, 60], Kassapoglou and Lagace [61, 62] and Webber and Morton [63]. Becker [64] used a particular warp deformation mode to investigate the free edge effects in laminates. Kassapoglou [65] generalized the principle of minimum complementary energy and force balanced method to analyze laminates under in-plane and out-of-plane loading. Yin [66, 67] used a variational method using Lekhnitskii's stress function for laminates under combinations of mechanical loading. Later, Yin [68] used the principle of complementary energy based on polynomial stress functions to evaluate the interlaminar stresses in laminates subjected non-uniform thermal loading.

Pipes and Pagano [69] developed the first numerical method to solve the two dimensional governing elasticity equations, where finite difference method was used to calculate the interlaminar stresses of long symmetric laminate under uniform axial strain. Later, Atlus et al. [70], Bhaskar et al. [71] and Salamon [72] used three dimensional finite difference method to determine the interlaminar stresses in angle-ply laminate. Wang and Crossman [73, 74] studied symmetric composite laminate subjected to uniform axial strain and thermal loading using finite element method. Herakovich et al. [75], Isakson and Levy [76], Rybicky

[77], Kim and Hong [78], Icardi and Bertetto [79], Lessard et al. [80] and Yi and Hilton [81] also used finite element method to study free edge effects in laminates. Spilker and Chou [82] used hybrid stress finite element method, Lee and Chen [83] used layer reduction technique, Robbins and Redy [84] used displacement based variable kinematic global local finite element method, Gaudenzi et al. [85] used three dimensional multilayer higher order finite element method to study similar problems.

From previous studies mentioned above, it is well established that free edge effects are dominant in multidirectional laminates and lead to very high interlaminar stresses that prematurely initiate inter-layer delamination. Therefore, determining interfaces with very large interlaminar stresses is critical for the assessment of delamination driven failure. By doing so, the interfaces most susceptible to delamination can be determined and strengthened accordingly during manufacturing to reduce their susceptibility to failure. Towards that, a Quasi-2D formulation within the finite element method (FEM) framework is established in this paper to determine delamination prone interlaminar regions in multidirectional laminates subjected to thermo-mechanical loading.

In the current paper, the variational formulation presented by Martin et al. [86] is extended for combined thermal and axial loading, referred to as “Quasi-2D” (Q-2D) formulation. The Q-2D formulation is implemented within the FEM framework to accurately determine the stress distribution near the free edges for cross-ply ($[0/90]_s$) and quasi-isotropic ($[45/-45/90/0]_s$) laminates. Comparison of the current results with previously published results and corresponding 3D model results establishes the validity and accuracy of the Q-2D model. This paper is divided into the following sections: Section 4.2 describes the mathematical formulation for the Q-2D followed by the details of the implementation within the finite element framework in Section 4.3. Discussion of results from several case studies are presented in Section 5.4 followed by conclusions.

4.2 Mathematical Formulation

Consider a laminate of length $2L$, width $2b$ and lamina/layer thickness of h as shown in Fig. 4.1(a). Tensile load is applied on the edges at Σ_{+L} and Σ_{-L} along the x_1 direction, and the edges at Σ_0 and Σ_{2b} are the free edges. Further, a temperature change of ΔT occurs uniformly within the laminate. Cross-section of the laminate consisting of N layers is shown in Fig. 4.1(b).

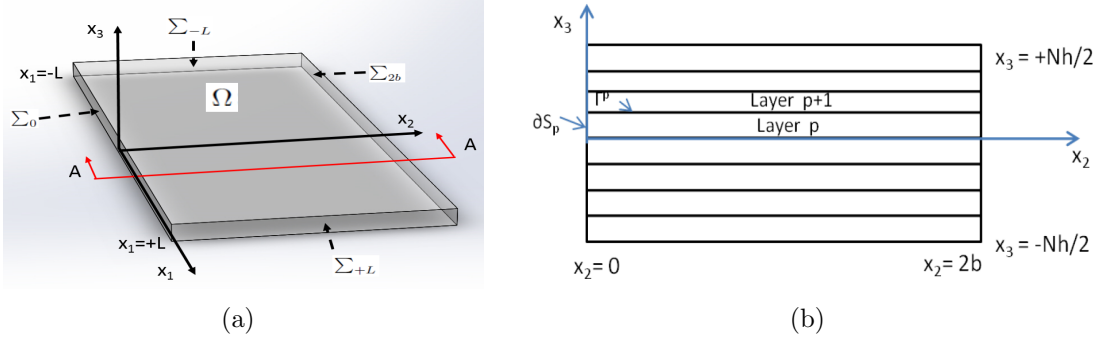


Figure 4.1: (a) 3D Laminate; (b) Cross-section of a 3D laminate

The stress components are assumed to be independent of x_1 in regions sufficiently far from the loading surface [69, 86], such that the displacement field $\{U\}$ can be defined as,

$$\begin{aligned}
 U_1(x_1, x_2, x_3) &= \tilde{U}_1(x_2, x_3) + \epsilon_{11}x_1 \\
 U_2(x_1, x_2, x_3) &= \tilde{U}_2(x_2, x_3) \\
 U_3(x_1, x_2, x_3) &= \tilde{U}_3(x_2, x_3)
 \end{aligned} \tag{4.1}$$

Here, ϵ_{11} is the uniform strain applied to the laminate along the x_1 direction. The displacement field $\{U\}$ and corresponding stress field $\{\sigma\}$ adhere to the following equations:

$$\frac{\partial \sigma_{ij}}{\partial x_j} = 0, \sigma_{ij} = a_{ijkh} \epsilon_{kh}^m, \forall i = 1, 2, 3 \text{ within } \Omega, \tag{4.2}$$

$$\epsilon_{ij}(U) = \frac{1}{2} \left(\frac{\partial U_i}{\partial x_j} + \frac{\partial U_j}{\partial x_i} \right) \text{ within } \Omega; \tag{4.3}$$

$$[U_i] = 0, [\sigma_{ij}n_j] = 0 \text{ on the interfaces } \Gamma^p; [\sigma_{ij}n_j] = 0 \text{ on } \sum_{2b} \text{ and } \sum_0 \quad (4.4)$$

$$[\sigma_{ij}n_j] = F_i \text{ on } \sum_{+L} \text{ and } \sum_{N\frac{h}{2}}; [\sigma_{ij}n_j] = -F_i \text{ on } \sum_{-L} \text{ and } \sum_{-N\frac{h}{2}} \quad (4.5)$$

Defined by equation (4.1), introducing a trial field V with $\epsilon_{11} = 0$ and averaging equation (4.2) gives,

$$\int_{\Omega} \frac{\partial \sigma_{ij}}{\partial x_j} V_i d\Omega = 0, \forall V_i \text{ with } i=1, 2, 3. \quad (4.6)$$

Applying divergence theorem to the above equation yields,

$$\int_{\Omega} \sigma_{ij} \frac{\partial V_i}{\partial x_j} d\Omega = \int_{\Sigma_{+L}} F_i V_i dS - \int_{\Sigma_{-L}} F_i V_i dS \quad (4.7)$$

Since, V_i does not depend on x_1 :

$$\int_{\Omega} \sigma_{il} \frac{\partial V_i}{\partial x_l} d\Omega = 0, \forall V_i \text{ with } l = 2, 3. \quad (4.8)$$

Using $\sigma_{ij} = a_{ijkh}\epsilon_{kh}^m$ yields,

$$\int_{\Omega} a_{ilkh} \left(\frac{\partial U_k}{\partial x_h} - \alpha_{kh} \Delta T \right) \frac{\partial V_i}{\partial x_l} d\Omega = 0, \forall V_i \text{ for } i, k, h=1, 2, 3; l=2, 3 \quad (4.9)$$

where, $\{\epsilon^m\} = \{\epsilon\} - \{\alpha\} \Delta T$.

Substituting the displacement field assumption given in equation (4.1),

$$\int_{\Omega} a_{ilkh} \left(\frac{\partial \tilde{U}_k}{\partial x_h} - \alpha_{kh} \Delta T \right) \frac{\partial V_i}{\partial x_l} dx_1 dx_2 dx_3 + \epsilon_{11} \int_{\Omega} a_{il11} \frac{\partial V_i}{\partial x_l} dx_1 dx_2 dx_3 = 0 \quad (4.10)$$

Dividing the volume integral into two integrals, one along the x_1 direction, and the

other in the plane of the cross section (x_2, x_3) gives,

$$\begin{aligned} & \int_{-L}^{+L} dx_1 \int_S a_{ilk\beta} \left(\frac{\partial \tilde{U}_k}{\partial x_\beta} - \alpha_{k\beta} \Delta T \right) \frac{\partial V_i}{\partial x_l} dx_2 dx_3 - \\ & \int_{-L}^{+L} dx_1 \int_S a_{ilk1} \alpha_{k1} \Delta T \frac{\partial V_i}{\partial x_l} dx_2 dx_3 + \epsilon_{11} \int_{-L}^{+L} dx_1 \int_S a_{il11} \frac{\partial V_i}{\partial x_l} dx_2 dx_3 = 0, \end{aligned} \quad (4.11)$$

with $l, \beta = 2, 3$.

$$\int_S a_{ilk\beta} \left(\frac{\partial \tilde{U}_k}{\partial x_\beta} - \alpha_{k\beta} \Delta T \right) \frac{\partial V_i}{\partial x_l} dx_2 dx_3 = \Delta T \int_S a_{ilk1} \alpha_{k1} \frac{\partial V_i}{\partial x_l} dx_2 dx_3 - \epsilon_{11} \int_S a_{il11} \frac{\partial V_i}{\partial x_l} dx_2 dx_3 \quad (4.12)$$

Applying divergence theorem on the right hand side

$$\int_{S^p} a_{ilk\beta} \left(\frac{\partial \tilde{U}_k}{\partial x_\beta} - \alpha_{k\beta} \Delta T \right) \frac{\partial V_i}{\partial x_l} dx_2 dx_3 = \Delta T \int_{\partial S} a_{ilk1} \alpha_{k1} V_i n_l ds - \epsilon_{11} \int_{\partial S} a_{il11} V_i n_l ds \quad (4.13)$$

where, “s” represents a coordinate that denotes the boundary ∂S , starting at the origin of the $x_2 - x_3$ axes for the region S and traversing in counter clockwise direction. Therefore, “s” is either “ x_2 ” or “ x_3 ” depending on the edge on the boundary being traversed.

The above equation is modified to account for layers with different orientation in a multidirectional laminate as given below,

$$\sum_{p=1}^N \int_{S^p} a_{ilk\beta}^p \left(\frac{\partial \tilde{U}_k^p}{\partial x_\beta} - \alpha_{k\beta}^p \Delta T \right) \frac{\partial V_i^p}{\partial x_l} dx_2 dx_3 = \Delta T \sum_{p=1}^N \int_{\partial S^p} a_{ilk1}^p \alpha_{k1}^p V_i^p n_l^p ds - \epsilon_{11} \sum_{p=1}^N \int_{\partial S^p} a_{il11}^p V_i^p n_l^p ds \quad (4.14)$$

Developing the right hand side of 4.14, contribution of each edge

$$\begin{aligned} \Delta T \sum_{p=1}^N & \left(\int_{-Nh/2+(p-1)h}^{Nh/2+ph} a_{i2k1}^p \alpha_{k1}^p V_i^p(2b, x_3) dx_3 - \int_{-Nh/2+(p-1)h}^{Nh/2+ph} a_{i2k1}^p \alpha_{k1}^p V_i^p(0, x_3) dx_3 \right) \\ & - \epsilon_{11} \sum_{p=1}^N \left(\int_{-Nh/2+(p-1)h}^{Nh/2+ph} a_{i211}^p V_i^p(2b, x_3) dx_3 - \int_{-Nh/2+(p-1)h}^{Nh/2+ph} a_{i211}^p V_i^p(0, x_3) dx_3 \right) \end{aligned} \quad (4.15)$$

Contribution of each interface,

$$\begin{aligned} \Delta T \sum_{p=1}^{N-1} & \left(- \int_0^{2b} (a_{i3k1}^{p+1} \alpha_{k1}^{p+1} - a_{i3k1}^p \alpha_{k1}^p) V_i^p(x_2, N\frac{h}{2} + ph) dx_2 \right) \\ & - \epsilon_{11} \sum_{p=1}^{N-1} \left(- \int_0^{2b} (a_{i311}^{p+1} - a_{i311}^p) V_i^p(x_2, N\frac{h}{2} + ph) dx_2 \right) \end{aligned} \quad (4.16)$$

and contribution of top and bottom

$$\begin{aligned} \Delta T & \left(- \int_0^{2b} a_{i3k1}^1 \alpha_{k1}^1 V_i^1(x_2, -N\frac{h}{2}) dx_2 + \int_0^{2b} a_{i3k1}^N \alpha_{k1}^N V_i^N(x_2, N\frac{h}{2}) dx_2 \right) \\ & - \epsilon_{11} \left(- \int_0^{2b} a_{i311}^1 V_i^1(x_2, -N\frac{h}{2}) dx_2 + \int_0^{2b} a_{i311}^N V_i^N(x_2, N\frac{h}{2}) dx_2 \right) \end{aligned} \quad (4.17)$$

Equation 4.14 is a generalized 2D formulation which has the displacement field along the x_1, x_2 and x_3 directions. The input to the above formulation is the fourth order elasticity tensor of each layer of the laminate for a linear elastic material, coefficient of thermal expansions, applied external strain and change in temperature. The effective loads calculated for a laminate are applied to the 2D generalized representation of the laminate in the finite element method model explained in the following section.

4.3 Implementation of the Quasi-2D Formulation

The above formulation can be implemented in several ways within finite element method. The method developed in this paper is to modify a thin slice of a 3D model to behave like a generalized 2D model. A 3D model with a small thickness (1 mm in this case) in the x_1 -direction is considered as shown in Fig. 4.2. Multi-point constraints are applied between the front and back face of the model such that the displacement fields are independent of x_1 -direction. In Fig. 4.2(a), m is a nodal point on the front surface and n is the corresponding nodal point on the back surface. These two points (m and n) are tied together such that the displacements u, v and w are identical for the pair nodes. Similarly, all the nodal points on the front surface are tied with their corresponding points on the back surface, which satisfies the requirement of displacement fields being independent of the x_1 -direction. This simulates the left hand side of equation (4.14). The external loads established by the right hand side of equation (4.14) are applied to the model on the edges in the $x_2 - x_3$ plane and the interfaces between the layers.

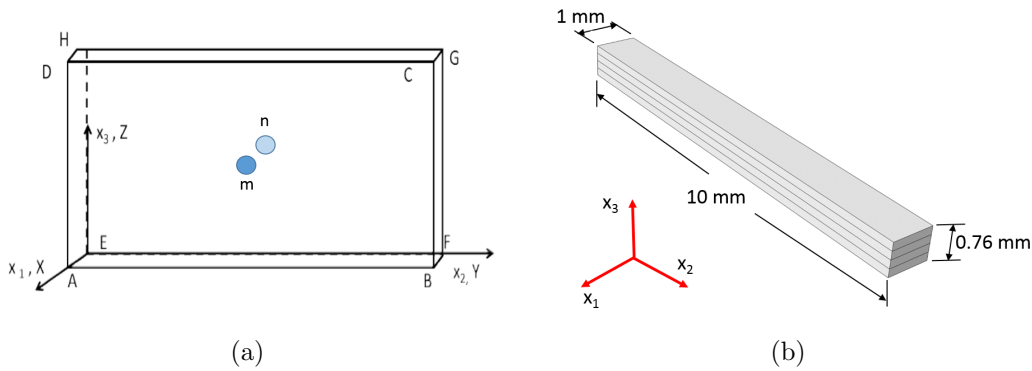


Figure 4.2: 3D slice of a laminate

Eight noded linear hexahedral elements (C3D8 in ABAQUS notation) are used to mesh the Q-2D model as shown in Fig. 4.3(a). Very fine mesh is used near the interfaces and free edge to sufficiently capture the stress singularities within these regions. However, only one element is used along the x_1 direction to enforce multi-point constraint described above.

Due to significantly large number of nodes on the front and back faces, enforcing multi-point constraints manually is cumbersome.

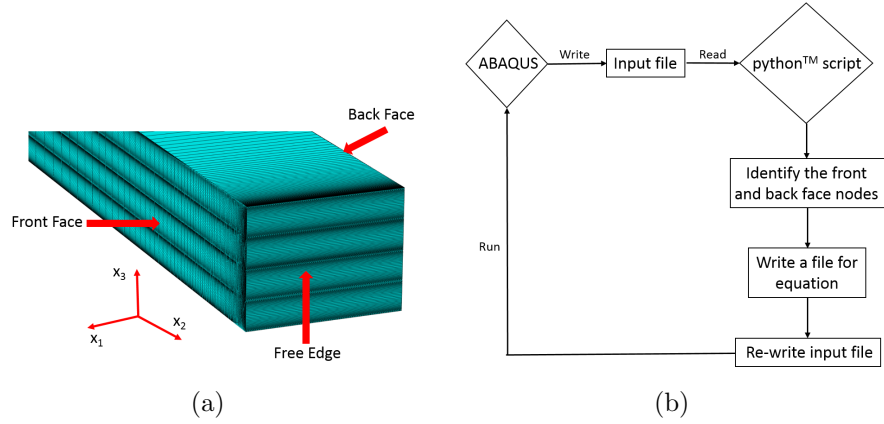


Figure 4.3: (a) Typical mesh in the Q-2D model; (b) Working principle of python™ script

A python™ script is written that reads the ABAQUS input file and writes the multi-point constraints. Working procedure of the python™ script is shown in Fig. 4.3(b). The input file obtained from ABAQUS without constraints is read by the python™ script, which identifies the corresponding nodes from the front and back faces. The script then writes the constraint equations for every node in a different file and finally it rewrites the main input file, which is capable of accessing the equation file generated. Fig. 4.4(a) shows a snapshot of the re-written input file which includes the equation file as an “input” and Fig. 4.4(b) shows a snapshot of the equation file where the equation constraints are written.

As an example, Fig. 4.5 shows the boundary conditions for $[45/-45/90/0]_s$ laminate subjected to an uniform axial strain, which is derived from Equation 4.14. As mentioned in the previous section, the input to the Q-2D model is the 4th order elasticity tensor of the individual layer and the applied strain. The effective loads that depend on the elastic constants are applied as pressure along the normal directions and surface traction in the parallel directions as shown in Fig. 4.5. \vec{x}_1 , \vec{x}_2 and \vec{x}_3 indicate the directions of load being applied, and are represented by the arrows showing the directions of load acting on

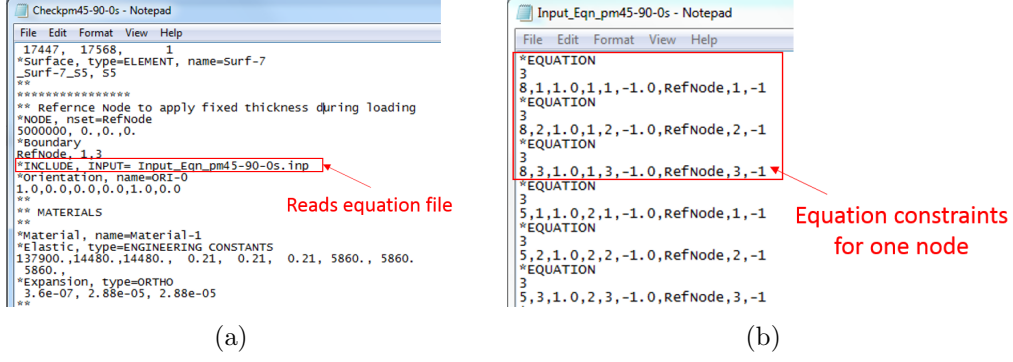


Figure 4.4: Snapshot of (a) input file and (b) equation file

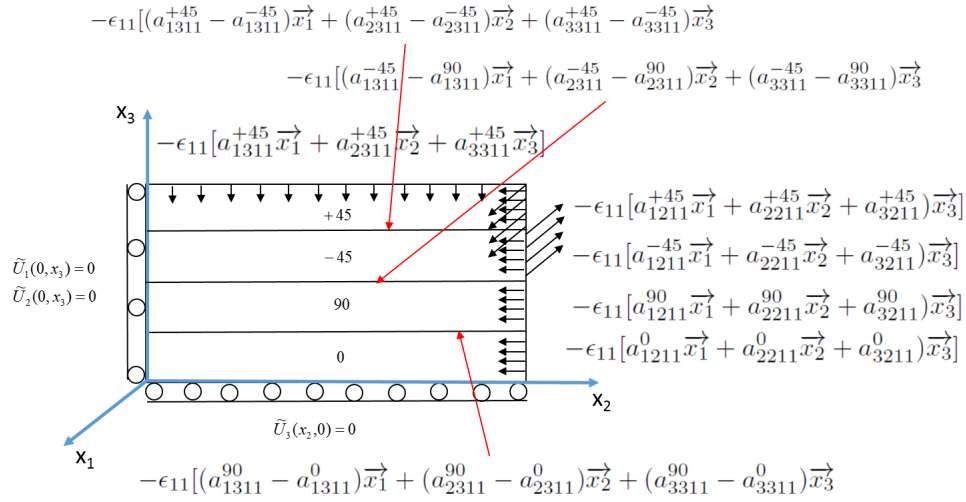


Figure 4.5: Boundary conditions for uniaxial extension

different layers. The loads corresponding to \vec{x}_3 direction are not shown in the figure since the associated elastic constants are equal to zero in the current example. Accordingly, the effective interface loads are applied along the interfaces between the layers.

4.4 Results and Discussions

The Q-2D model is applied to several laminates subjected to three main types of loading: uniform axial extension (Section 4.4.1), uniform thermal loading (Section 4.4.2) and combined axial and thermal loading (Section 4.4.3). The results are compared with published

(where available) and 3D model results to establish the reliability of the current modeling approach.

4.4.1 Case 1: Axial Loading

In this section, $[0/90]_s$ and $[45/-45/90/0]_s$ laminate subjected to an uniform axial (x-direction) strain is considered. The following material properties were used: $E_{11} = 137.9$ GPa, $E_{22} = E_{33} = 14.48$ GPa, $G_{12} = G_{13} = G_{23} = 5.86$ GPa and $\nu_{12} = \nu_{13} = \nu_{23} = 0.21$, which correspond to a high modulus graphite/epoxy laminate [87]. The $[0/90]_s$ cross-ply laminate subjected to an uniform axial (x_1 -direction) strain has been previously investigated by Zhang et al. [46], Tahani and Nosier [47], Wang and Crossman [74], Nguyen and Caron [87], Carreira et al. [88] and Zhen et al. [89]. Fig. 4.6 shows the comparison interlaminar stress distribution at the 0/90 interface of $[0/90]_s$ laminate subjected to a uniform axial strain with few previously published results. Even though, Fig. 4.6(a) shows that the present model predicts a slightly higher interlaminar normal stress at the edges compared to previous studies, the behavior is identical. The shear stress (σ_{23}) distribution is comparable to other models (Fig. 4.6(b)).

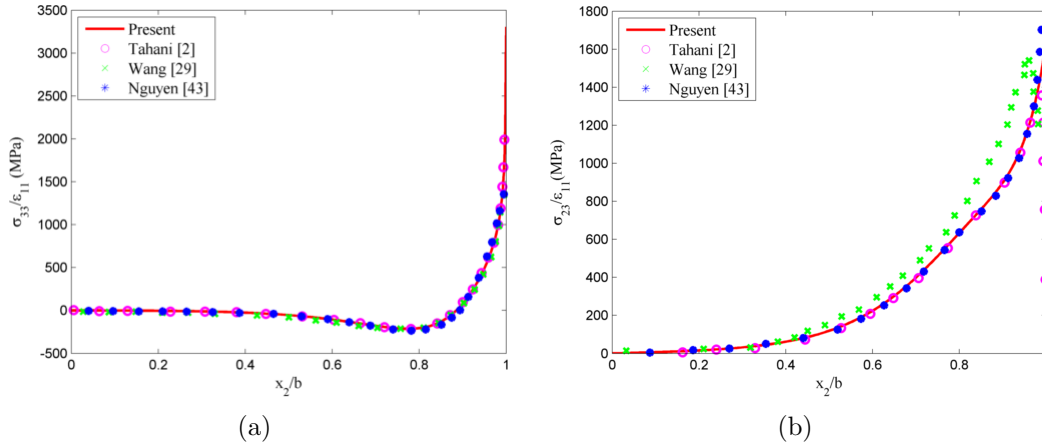


Figure 4.6: Distribution of interlaminar stresses along the 0/90 interface of $[0/90]_s$ laminate subjected to uniform axial extension (a) normal stress σ_{33} and (b) shear stress σ_{23}

For $[45/-45/90/0]_s$ laminate, seldom results were found in the literature to compare the results from the current Q-2D model. In this case, a full 3D model was analyzed and the results from the Q-2D model was compared with the corresponding 3D model. Fig. 4.7 shows the comparison of Q-2D and 3D model at different interfaces, which shows an excellent agreement between these two models.

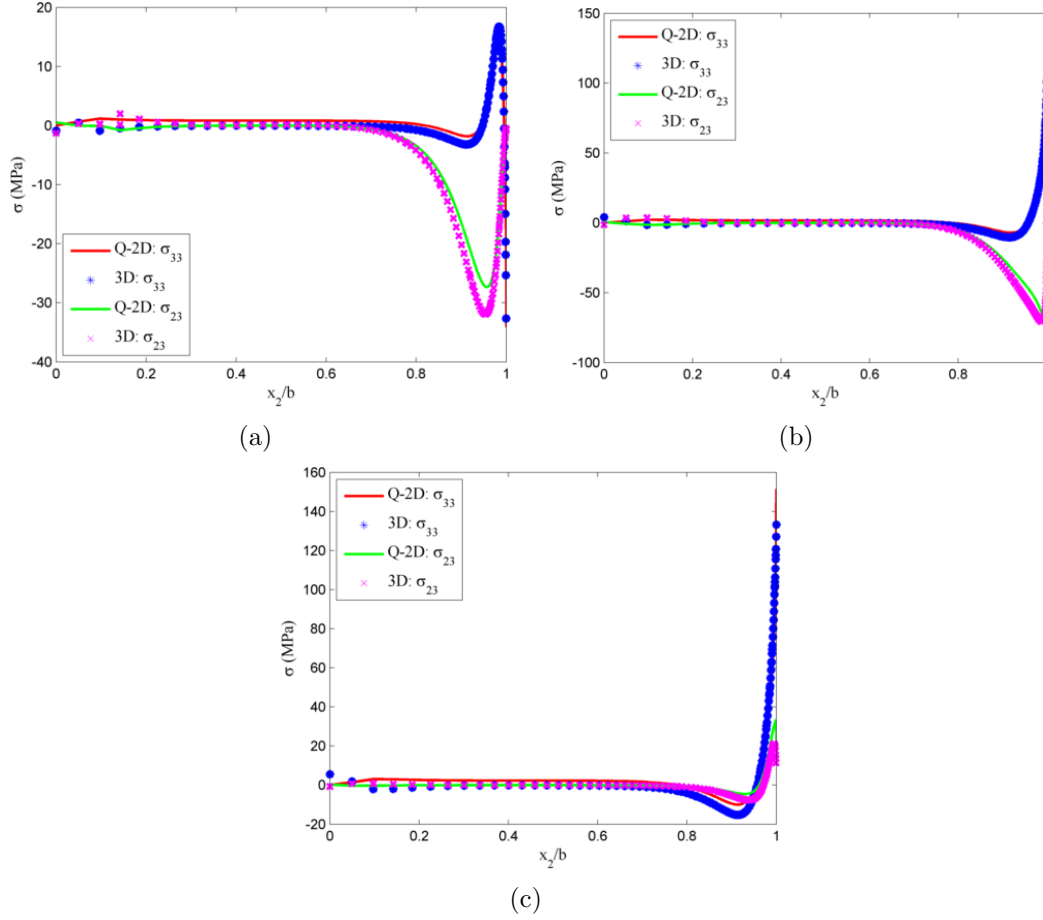


Figure 4.7: Distribution of interlaminar stress of $[45/-45/90/0]_s$ laminate subjected to uniform axial extension along (a) 45/-45, (b) -45/90 and (c) 90/0 interface

4.4.2 Case 2: Thermal Loading

In this section, $[0/90]_s$ and $[45/-45/90/0]_s$ laminates subjected to an uniform temperature change ΔT throughout the modeling domain is considered. For direct comparison with the previously published results, the following material properties were used: $E_{11} = 137.9$ GPa, $E_{22} = E_{33} = 14.48$ GPa, $G_{12} = G_{13} = G_{23} = 5.86$ GPa, $\nu_{12} = \nu_{13} = \nu_{23} = 0.21$, $\alpha_1 = 0.36 \times 10^{-6} \text{ } ^\circ\text{C}^{-1}$ and $\alpha_2 = \alpha_3 = 28.8 \times 10^{-6} \text{ } ^\circ\text{C}^{-1}$. Fig. 4.8 shows the distribution of σ_{33} (Fig. 4.8(a)) and σ_{23} (Fig. 4.8(b)) for $\Delta T = 1 \text{ } ^\circ\text{C}$. It is observed from Fig. 4.8 that the current results are in excellent agreement with those determined by previous investigators [47, 68, 87].

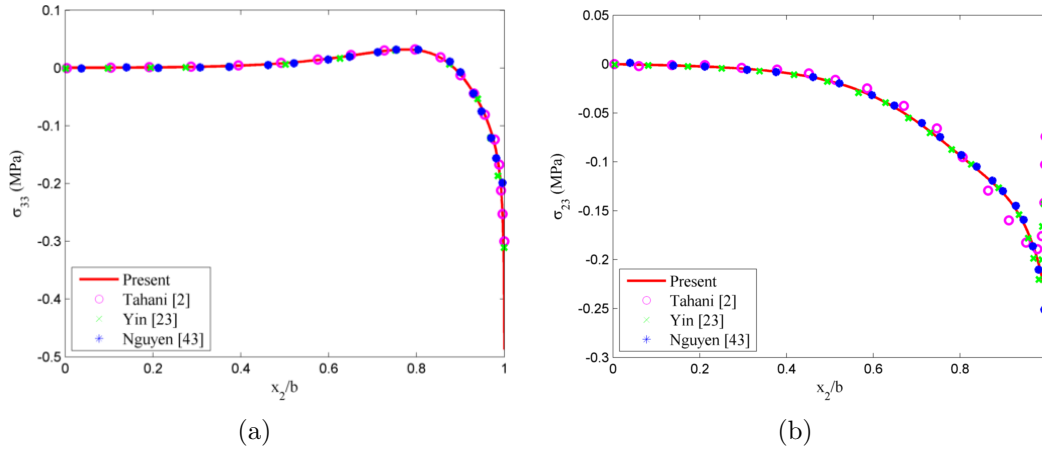


Figure 4.8: Distribution of interlaminar stresses along the $0/90$ interface of $[0/90]_s$ laminate due to a temperature change $\Delta T = 1 \text{ } ^\circ\text{C}$ (a) normal stress σ_{33} and (b) shear stress σ_{23}

Fig. 4.9 shows the distribution of interlaminar stresses for $[45/-45/90/0]_s$ laminate along $45/-45$ (Fig. 4.9(a)), $-45/90$ (Fig. 4.9(b)) and $90/0$ interfaces (Fig. 4.9(c)) subjected to an uniform temperature change $\Delta T = 1 \text{ } ^\circ\text{C}$. It is observed from Fig. 4.9 that the current results are in good agreement with the corresponding 3D model results.

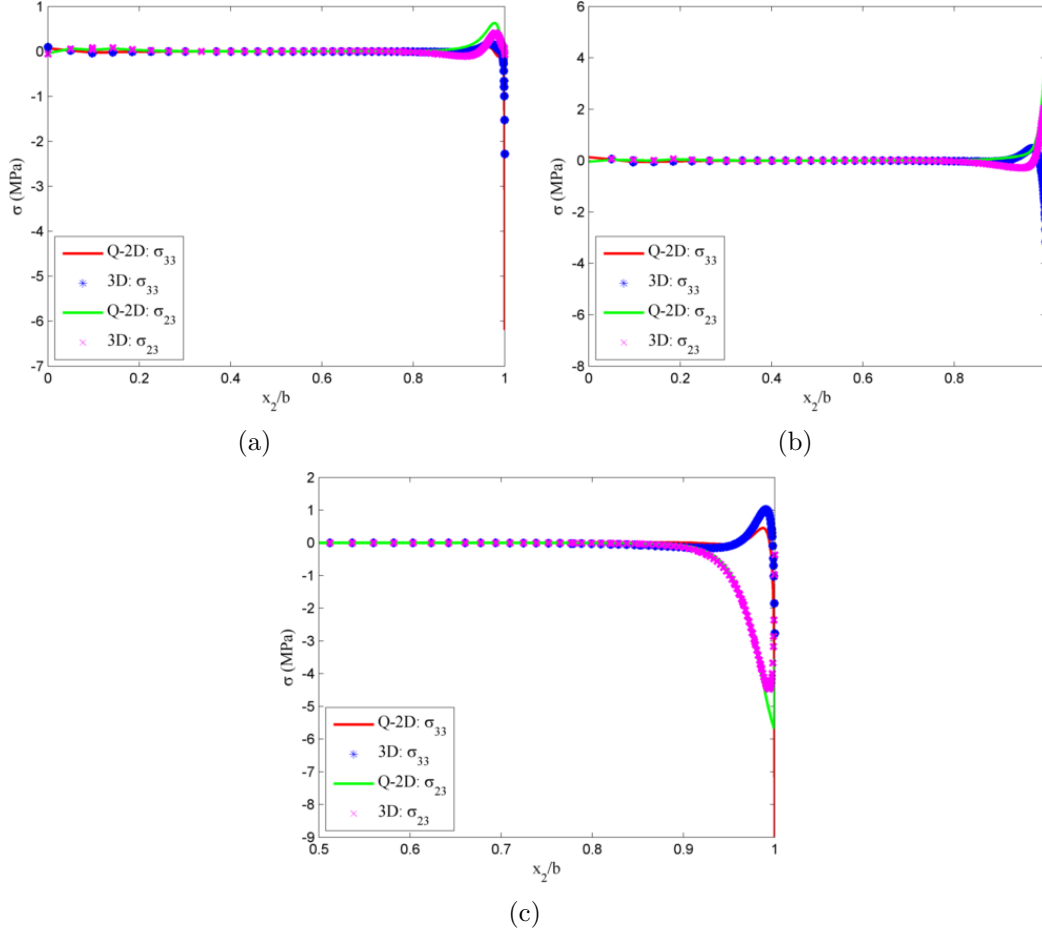


Figure 4.9: Distribution of interlaminar stress of $[45/-45/90/0]_s$ laminate due to a temperature change $\Delta T = 25^\circ\text{C}$ (a) 45/-45, (b) -45/90 and (c) 90/0 interface

4.4.3 Case 3: Combined Axial and Thermal Loading

In this section, $[0/90]_s$ and $[45/-45/90/0]_s$ laminates subjected to a uniform axial strain ($\epsilon_{11} = 0.01$) and uniform temperature change ($\Delta T = 1^\circ\text{C}$) is considered. The material properties were the same as mentioned in Section 4.4.2. Fig. 4.10 and Fig. 4.11 show the distribution of interlaminar stresses for $[0/90]_s$ and $[45/-45/90/0]_s$ laminates subjected to $\epsilon_{11} = 0.01$ and $\Delta T = 25^\circ\text{C}$. These results are compared with their corresponding 3D model and is observed (Fig. 4.10 and Fig. 4.11) that the current results are in excellent

agreement with the 3D results.

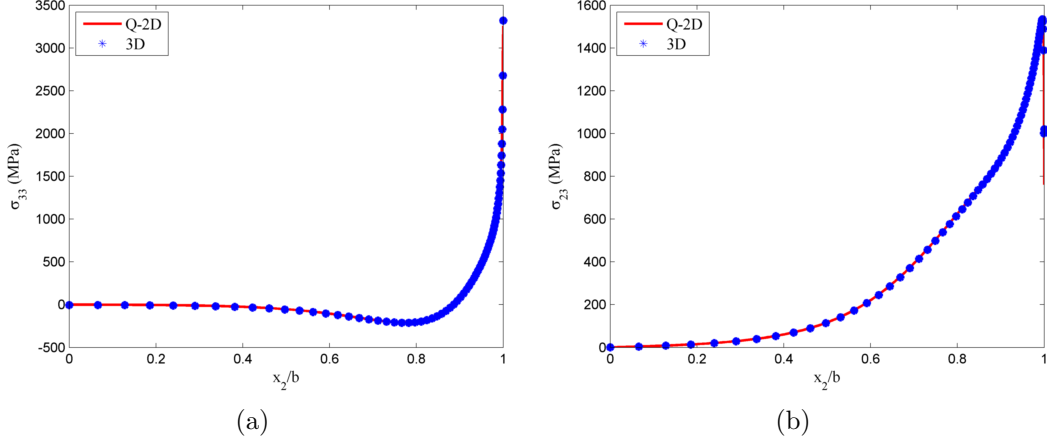


Figure 4.10: Distribution of interlaminar stress along the 0/90 interface of $[0/90]_s$ laminate subjected to $\epsilon_{11} = 0.01$ and $\Delta T = 25^\circ\text{C}$ (a) normal stress σ_{33} and (b) shear stress σ_{23}

4.4.4 Efficiency of Q-2D Model

The Q-2D modeling framework developed in this paper utilizes a fairly straight forward derivation and an easy implement within finite element method. It is also highly efficient in computational cost compared to the 3D counterpart models. Table 4.1 shows a comparison of the computational time required by the Q-2D and 3D models of $[45/-45/90/0]_s$ laminate (it takes same time for all loading cases). The total computational time required by Q-2D model is approximately 2 minutes and for the 3D model is approximately 60 minutes using the same Intel® Core™ i7-3540M 3.00 GHz CPU. Although, 60 minutes seems like a reasonable time for a 3D model, it is for only 8 layers laminate ($[45/-45/90/0]_s$). The time required will scale up with increased number of layers in the case of a thicker laminate (for example 48 layers). Hence, the Q-2D model can save the computational time significantly while accurately predicting the interlaminar stress distribution.

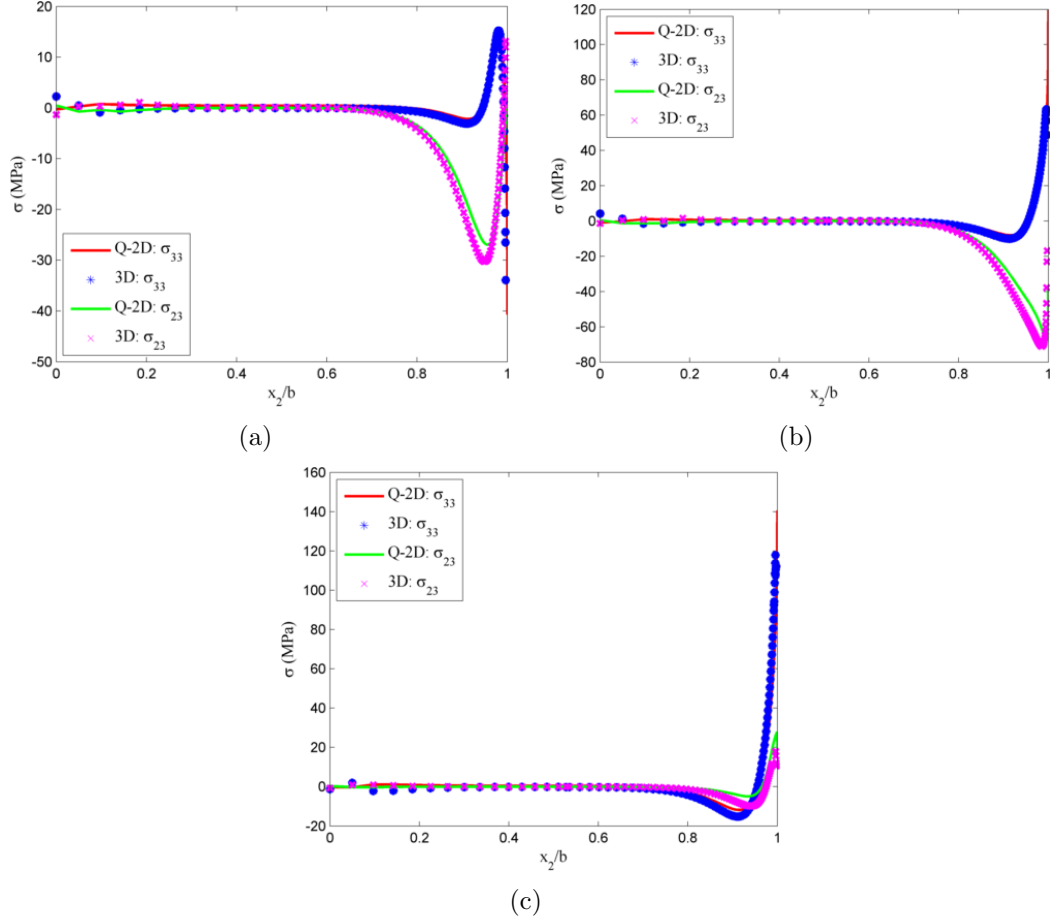


Figure 4.11: Distribution of interlaminar stress of $[45/-45/90/0]_s$ laminate subjected to $\epsilon_{11} = 0.01$ and $\Delta T = 25^\circ C$ along (a) 45/-45, (b) -45/90 and (c) 90/0 interface

Table 4.1: Comparison of Q-2D and 3D model

Model	No. of Elements	Approximate Time (min)
Q-2D	23424	2
3D	318786	60

4.5 Conclusions

In this study, free edge laminates subjected to uniform axial extension and uniform temperature change are investigated with Quasi-2D model. This generalized plane strain model is

capable of predicting the interface stresses accurately compared to 3D model. The accuracy and effectiveness of the present Q-2D model is validated with the previously published results and 3D model. This Q-2D model is found to be capable of predicting the interlaminar stresses for different laminates subjected to uniform axial loading and/or thermal loading in a reliable and efficient way.

Chapter 5

Interface Strengthening of Multi-directional Laminates using Additive Manufacturing

A novel fabrication technique to improve the interlaminar shear strength (ILSS) of multi-directional prepreg laminates using additive manufacturing technology is proposed in this paper. Additively manufactured (also known as 3D printed) patterns are fabricated on pre-pregs, which are used to manufacture the laminate. Critical inter-laminar regions that are most susceptible to delamination type failure are first determined to selectively reinforce those inter-laminar regions. The effect of 3D printed lines on the ILSS of modified laminates is compared to that of pristine laminates using short beam shear (SBS) test. A significant improvement in the ILSS is observed with the 3D printed inter-laminar regions, which proves the effectiveness of modified inter-laminar regions using additive manufacturing technology towards improving the interlaminar strength of multi-directional laminates.

5.1 Introduction

Fiber reinforced laminated polymer matrix composites have a wide range of applications predominantly in the aerospace, automobile and nuclear industries. Specially, polymer matrix composites (PMC) are known for their high strength-to-weight and stiffness-to-weight ratios [90]. However, interlaminar regions between reinforcing layers in PMCs are critical regions that are highly susceptible to delamination under mechanical loading [91, 92]. One of the most common failure mechanisms in laminated composites is delamination [93], which maybe caused due to weak matrix, bad layup, mechanical loading types such as static, impact or fatigue [94, 95, 96, 97, 98]. Delamination often causes premature failure

of composites, which in turn, results in the global failure of a component with reduced strength and stiffness .

Earlier researchers have explored different routes to improve the interlaminar strength of a composite, such as, stitching, weaving, z-pins [99] and braiding [94]. Although, these methods are capable of increasing the through-thickness properties of a composite, they have shown to reduce the in-plane properties due to the damage of the reinforcing fiber or by creating resin rich zones [94, 100]. Other methods to improve the interlaminar properties include carbon nanotubes (CNTs) dispersed in the matrix [101, 102] and nanowires synthesized on fabric [103, 104, 105, 106, 107, 108, 109, 110]. CNTs pose major challenges due to their uneven distribution and tendency to agglomerate [92, 111]. The existing methods of dispersion of CNTs in a composite damage the fiber [92, 101, 102] due to high temperature during fabrication.

In this paper, a novel fabrication technique using additive manufacturing (AM) is proposed to improve the interlaminar properties of fiber reinforced laminated polymer composites. It is hypothesized that the interlaminar shear strengths (ILSS) of pre-preg laminates can be improved by imparting reinforcing patterns at the interlaminar regions using AM, also called 3D printing. Short beam shear (SBS) tests are conducted on unreinforced (called pristine laminates) and reinforced (with 3D printed interlaminar regions) laminates to determine their ILSS. A significant improvement in the ILSS values is observed in the reinforced laminates as compared to the unreinforced laminates.

The paper is organized in the following sections: Section 5.2 presents a finite element analysis used to determine delamination prone interlaminar regions in a multi-directional pre-preg laminate. Section 5.3 describes the experimental details and section 5.4 discusses the results followed by conclusions.

5.2 Determination of Delamination Prone inter-laminar regions

Edge effects in a multi-directional laminated composite refers to the high inter-laminar stresses developed due to property mismatch between different plies [46]. This inter-laminar region stress plays a vital role on delamination or transverse cracking and it is very important to determine it accurately. Classical lamination theory (CLT) is unable to determine this inter-laminar region stress accurately since this stress state is three dimensional in nature [46, 47]. Therefore, various analytical and numerical approaches such as finite difference, finite element, closed form analytical approach, boundary layer theories and layer-wise theories have been used to calculate the inter-laminar stresses.

Martin et al. [86] presented a variational formulation of Pipes and Pagano's [69] formulation, which is used here to determine the inter-laminar region stresses. This generalized plane strain formulation allows us to determine the stress distribution on the inter-laminar regions accurately with the help of numerical method. ABAQUS (a commercially available software) is used for numerical modeling in this paper. A sixteen layer laminate with a stacking of $[+45_2/-45_2/90_2/0_2]_s$ is used and the schematic cross section of this laminate is shown in Fig. 5.1. Fig. 5.2(a) shows the inter-laminar normal stress (σ_{33}) and Fig. 5.2(b) shows the shear stress (σ_{23}) distribution of this sixteen layer laminate. It is observed from Fig. 5.2 that the inter-laminar region stress is higher for inter-laminar regions 2, 4 and 6 compared to other inter-laminar regions, which implies that dissimilar inter-laminar regions (+45/-45, -45/90 etc.) experience more stress than similar inter-laminar region (+45/+45, 90/90 etc.). So, this dissimilar inter-laminar regions will be modified to increase the inter-laminar region strength of the laminate as discussed in the following section.

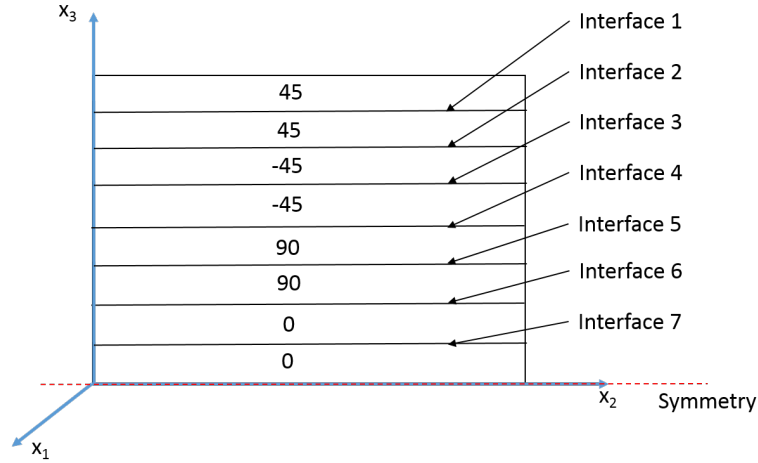


Figure 5.1: Schematic cross section of laminate

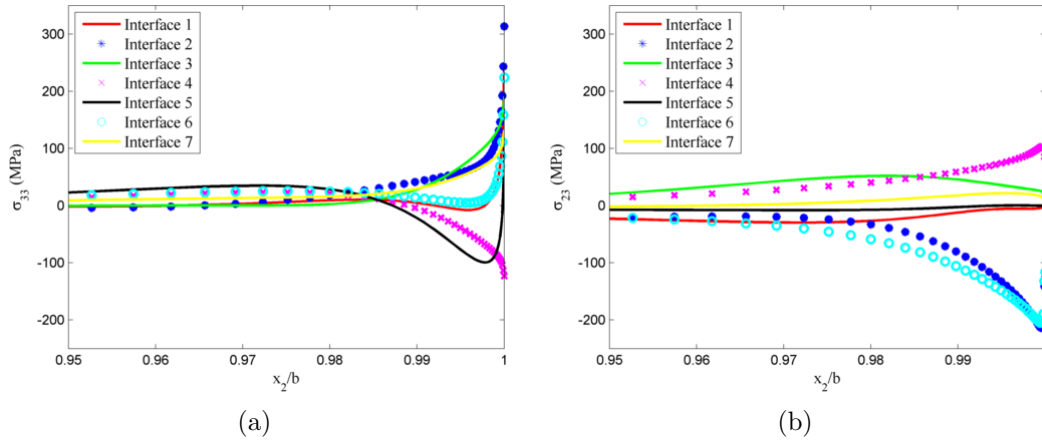


Figure 5.2: Distribution of interlaminar stress along different inter-laminar regions of $[45_2/-45_2/90_2/0_2]_s$ laminate (a) normal stress σ_{33} and (b) shear stress σ_{23}

5.3 Experimental Details

5.3.1 Types of laminate investigated

Two types of laminate with 40 layers are investigated in this paper; type A and type B. For type A laminate, the stacking is $[+45_5/-45_5/90_5/0-5]_s$ and for type B the stacking

is $[+45_3 / -45_3 / 90_3 / 0_3 / +45_2 / -45_2 / 90_2 / 0_2]_s$. Both types of laminate are made using three different conditions and they are pristine, 3D printed inter-laminar region and 3D printed inter-laminar region with additional resin. On pristine condition, no modifications are made on the pre-pregs and this pristine condition is used as a baseline for comparison. On 3D printed laminates, dissimilar inter-laminar regions (for example $+45 / -45$, $-45 / 90$ etc.) are 3D printed (refer to section 5.3.3). On 3D printed laminate, some voids are observed on the 3D printed inter-laminar region (as will be explained in section 5.4). To get rid of these voids, additional resin is used and this condition is referred to as 3D printed with additional resin.

5.3.2 Material system

Unidirectional carbon fiber pre-preg tape, which is purchased from CST Composites (www.cstsales.com), is used. The material properties of carbon fiber pre-preg are given in Table 5.1. Epon 862 with EPIKURE 9553 hardener is used as additional matrix material. The hardener is mixed with the resin at a ratio (weight) of 16.9:100, as recommended by the manufacturer.

Table 5.1: Pre-pregs properties (www.cstsales.com)

Properties	Pre-pregs
Fiber aerial weight	150 gm/m^2
Resin content	35 %
Thickness	0.005-0.006 in.

5.3.3 3D printing on pre-pregs

The 3D printing process starts with printing a base which acts as a support for the actual structure to be printed. MakerBot Replicator desktop 3D printer is used to print on pre-pregs as shown in Fig. 5.3(a). Pre-pregs are attached to the printer plate with scotch tape as shown in Fig. 5.3(b). Polylactic Acid (PLA) is used as 3D printing material at Temperature of 215 °C . Usually this 3D printer always starts printing on top of the printer plate. For better adhesion with the printer plate, it always prints a raft which acts as a

base; after printing, it is possible to take off the raft from the actual part. One big challenge in printing on top of the pre-pregs is it needs to print without any raft or support. The adhesion between pre-pregs and the lines (to be printed on pre-pregs) is not good without the raft, so the printed lines do not stick to the pre-pregs. The interesting thing is that, lines with a raft on pre-pregs prints well, which is not desirable. One thing is clear here; that printing a raft on pre-pregs is possible because the adhesion between pre-pregs and raft is good. Our design is just printing some lines on the pre-pregs so we have modified the raft settings and this new setting gives us some printed lines on the pre-pregs. Fig. 5.4 shows the customized raft settings along with the default one. Usually the raft has 3 layers, but in our case, once the printer is done with printing a single layer, the printing is cancelled manually to stop the printer from printing more layers of raft along with actual line design. Fig. 5.5 shows printed raft both default and custom. The default raft is a combination of small, thick and wide zigzag line while the customized raft is large, thin lines. Fig. 5.6(a) shows the 3D printed lines on pre-pregs and Fig. 5.6(b) shows the schematic cross section with dimensions. The 3D printed line width is 0.65 mm, thickness is 0.25 mm and the gap between two successive lines is 2.6 mm as shown in Fig. 5.6(b).

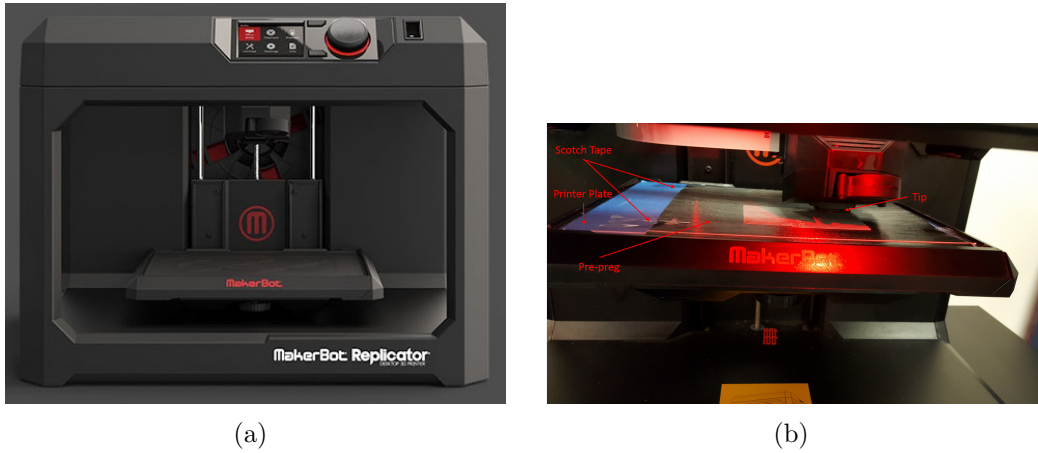


Figure 5.3: (a) MakerBot Replicator desktop 3D printer and (b) 3D printing on pre-pregs

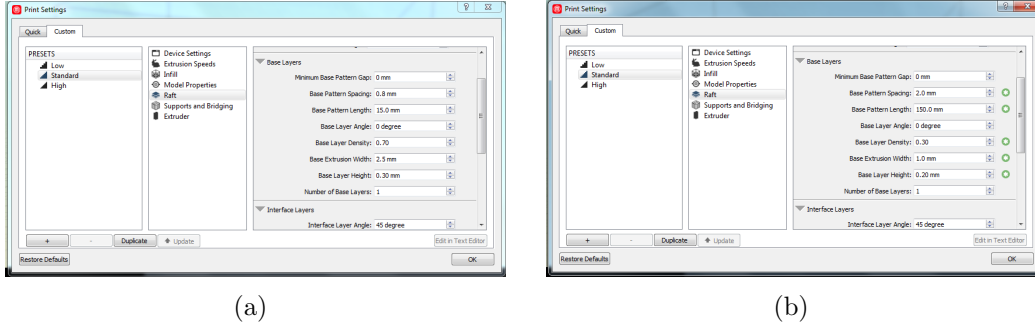


Figure 5.4: Raft settings (a) default and (b) custom

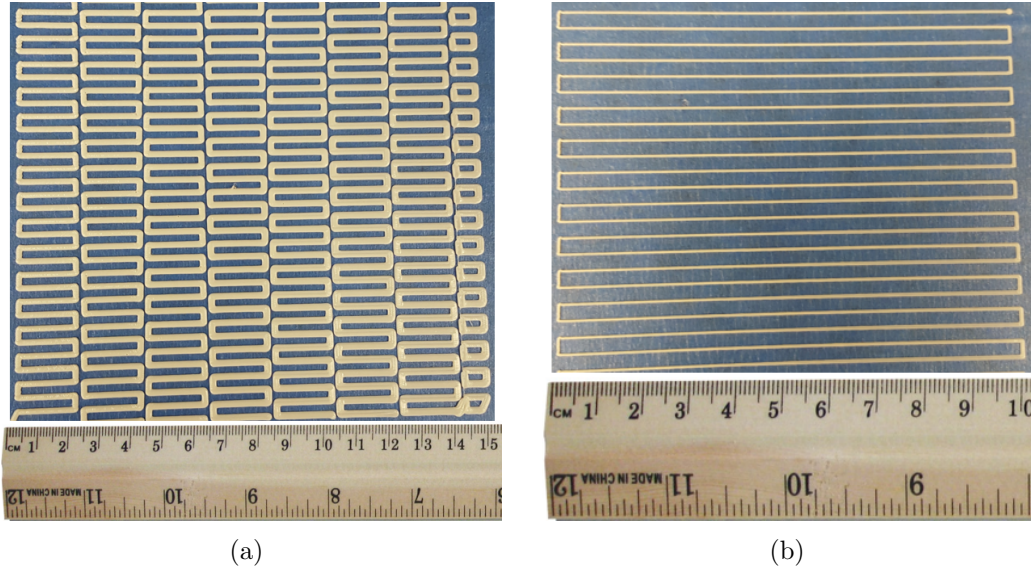


Figure 5.5: Printed raft (a) default and (b) custom

5.3.4 Laminate Fabrication

Autoclave molding process is used to manufacture the composite laminates. Fig. provides an overview of the manufacturing process. Pre-pregs are placed between two Aluminum mold plates and the completed mold is then enclosed in a vacuum bag. Vacuum is created by using a vacuum pump and the mold is placed inside an oven for curing. For the current material system, the resin is cured at 135 °C for 1 hour. In case of 3D printed interface with additional resin laminate, a brush is used to apply the additional resin on the 3D printed inter-laminar region.

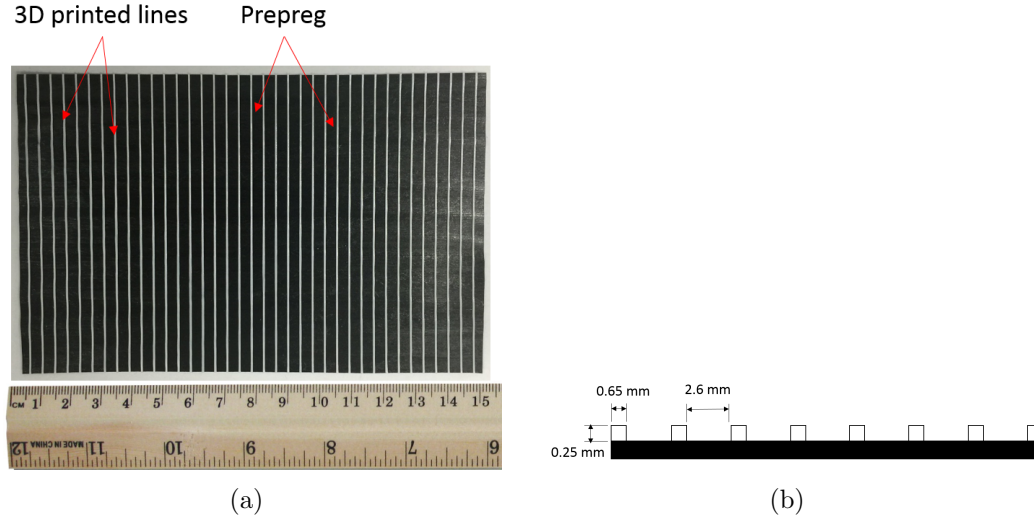


Figure 5.6: (a) 3D printed lines on prepreg and (b) Schematic cross-section of 3D printed prepreg

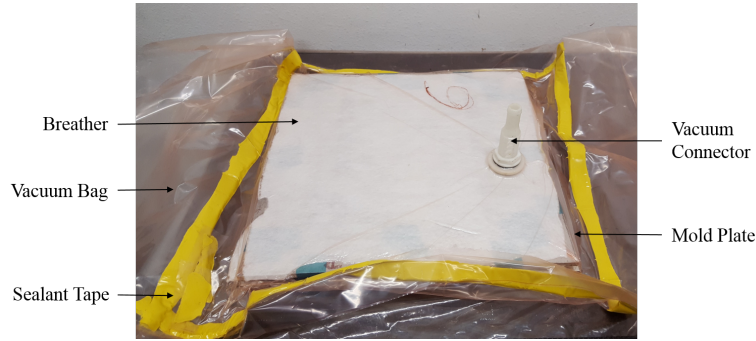


Figure 5.7: Manufacturing of laminate

5.3.5 Short beam shear test

Short beam shear (SBS) tests are conducted to measure the interlaminar shear strength (ILSS) of the composite. A total number of five specimens are tested for each type of laminate and specimens are prepared according to ASTM D2344 standard [42]. SBS tests are carried out on Instron 8801 machine with a loading rate of 1.0 mm/min.

5.4 Results and Discussions

Multi-directional prepreg laminates with and without the modified inter-laminar region are investigated in this paper in order to analyze their ILSS. It should be noted that, tensile properties are fiber dominated properties and ILSS is matrix dominated properties [112]. In this paper, SBS test is conducted since the focus of this paper is the modification of inter-laminar region, which is a matrix dominated region. Fig. 5.8 shows the cross section of 3D printed laminate for both type A and type B; more voids are observed for type B (Fig. 5.8(b)) compared to type A (Fig. 5.8(a)). This is because prepregs are used in this experiment and these prepregs are already impregnated with resins. For type A, there are only 6 inter-laminar regions which are 3D printed and it seems from Fig. 5.8(a) that the resin sufficiently covers the 3D printed lines in the inter-laminar regions. However, for type B 14 inter-laminar regions are 3D printed and the resin is not sufficient to cover all the 3D printed lines, which creates more voids as shown Fig. 5.8(b). To get rid of these voids, additional resins are used as mentioned in section 5.3.1. Fig. 5.9 shows the cross section of 3D printed laminates with additional resins for both types. Comparing Fig. 5.8 and Fig. 5.9, it is observed that less voids are found by using additional resins in the 3D printed inter-laminar region.

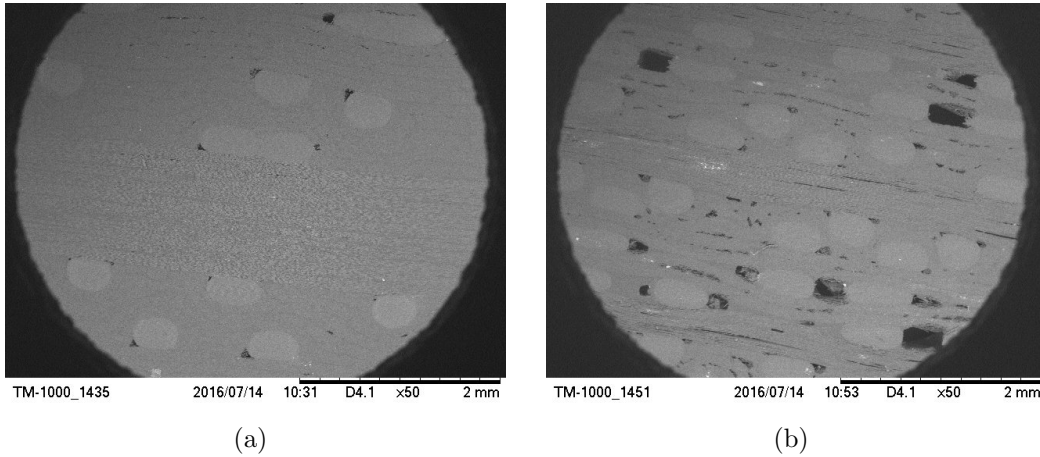


Figure 5.8: Cross section of 3D printed laminate (a) type A and (b) type B

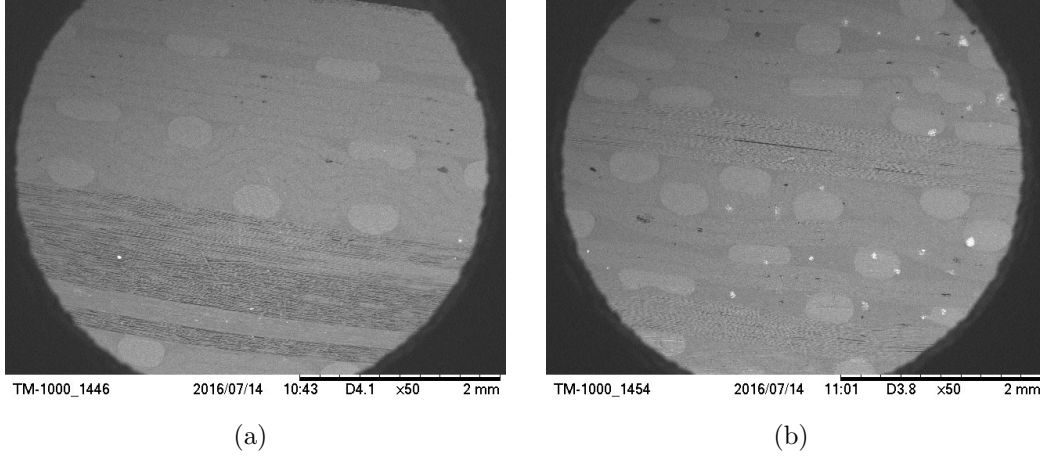


Figure 5.9: Cross section of 3D printed laminate with additional resins (a) type A and (b) type B

Fig. 5.10 shows the ILSS of both type A and type B laminates in three different conditions (pristine, 3D printed inter-laminar region and 3D printed inter-laminar region with additional resins). It is observed for type A, that for the 3D printed inter-laminar region laminate, the ILSS is increased by 21.30 % compared to pristine laminate, while for 3D printed with additional resin, the ILSS is increased by 28.35 %. This increase in ILSS with 3D printed inter-laminar region is because of formation of teeth along the inter-laminar region as shown in Fig. 5.11 and this 3D printed lines increases the bridging effect along the inter-laminar regions, which in turn increases the ILSS. One thing to notice here is that there is little difference in ILSS for type A with 3D printed inter-laminar region and 3D printed inter-laminar region with additional resin. This is due to the fact that the use of additional resin in the inter-laminar regions really does not make a significant difference to get rid of the voids (refer to Fig. 5.8(a) and 5.9(a)). For type B, in the case of the 3D printed inter-laminar region, the ILSS is decreased by 38.86 % compared to pristine laminate because of the voids observed (refer to Fig. 5.8(b)), which acts as a damage catalyzing region and reduces the ILSS. However, the 3D printed inter-laminar region with additional resin increased the ILSS by 11.26 % compared to the pristine one because it

significantly reduces the void contents. All these results are summarized in Table 5.2 along with the percentage increase in laminate thickness for different inter-laminar region modifications.

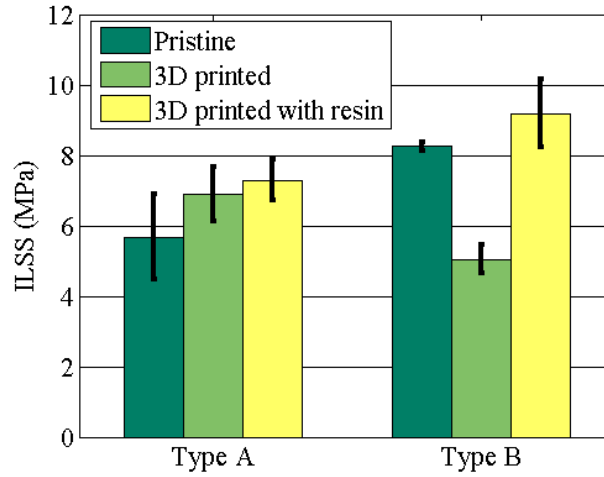


Figure 5.10: Bar chart showing ILSS for composites with standard deviation

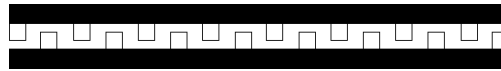


Figure 5.11: Formation of teeth along the 3D printed inter-laminar region

Table 5.2: Comparison of ILSS of different laminates

Type	Thickness (mm)	% Increase	ILSS (MPa)	% Increase
A pristine	5.31	-	5.68 ± 1.2	-
A 3D printed	6.39	20.34	6.89 ± 0.78	21.30
A 3D printed with resin	6.66	25.42	7.29 ± 0.58	28.35
B pristine	5.44	-	8.26 ± 0.12	-
B 3D printed	7.03	29.94	5.05 ± 0.41	-38.86
B 3D printed with resin	7.92	46.70	9.19 ± 0.96	11.26

Fig. 5.12 and 5.13 show the cross section of failed specimen along with top and bottom surface for type A and B respectively. From Fig. 5.12, for all three conditions of type A laminate, the same failure patterns are observed which includes mostly delamination with some fiber splitting. However, more delaminations are observed for pristine condition (Fig.

5.12(a)) compared to the 3D printed inter-laminar region (Fig. 5.12(b)) and 3D printed inter-laminar region with additional resin (Fig. 5.12(c)). This is because of the bridging effect that is created by the 3D printed lines along the inter-laminar regions. Similar failure patterns i.e. delamination dominated failure along with some fiber splitting, are also observed for type B laminate as well, as shown in Fig. 5.13.

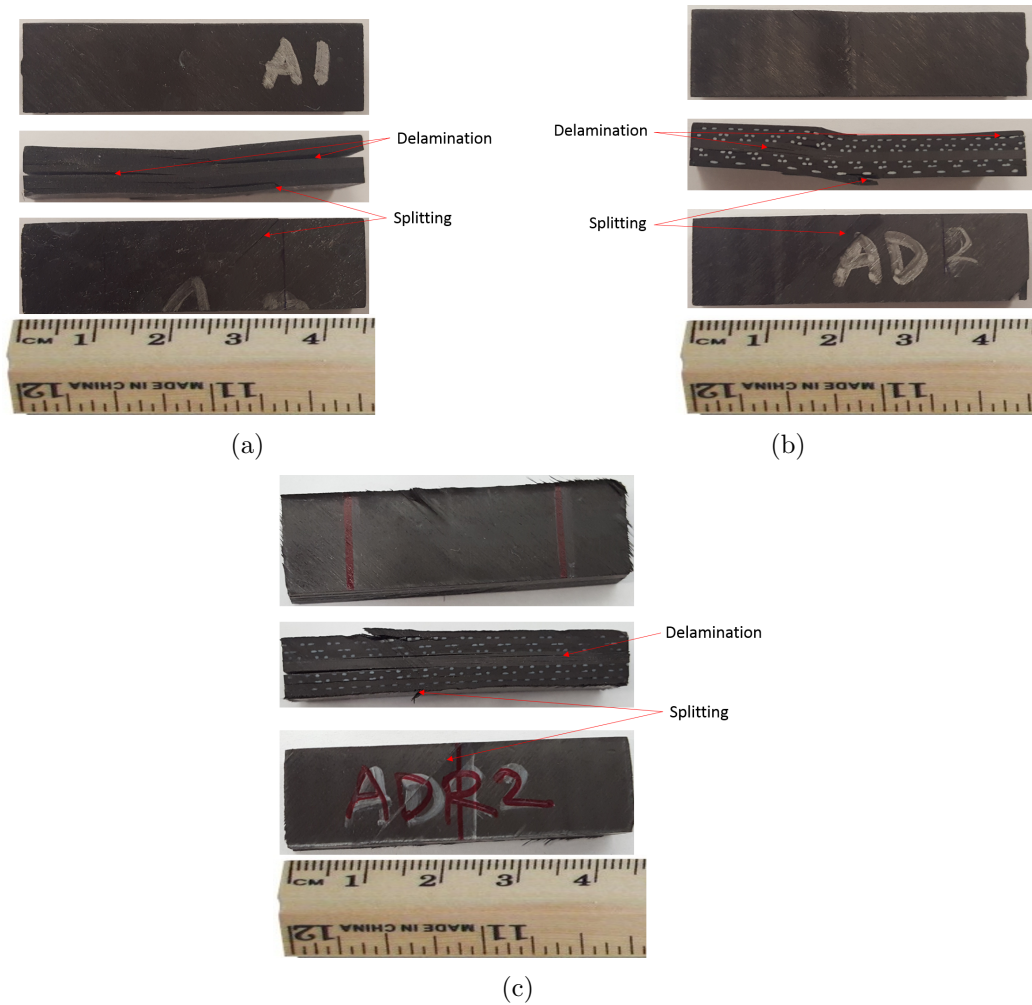


Figure 5.12: Cross section along with top and bottom surfaces of type A laminate (a) pristine, (b) 3D printed inter-laminar region and (c) 3D printed inter-laminar region with additional resin

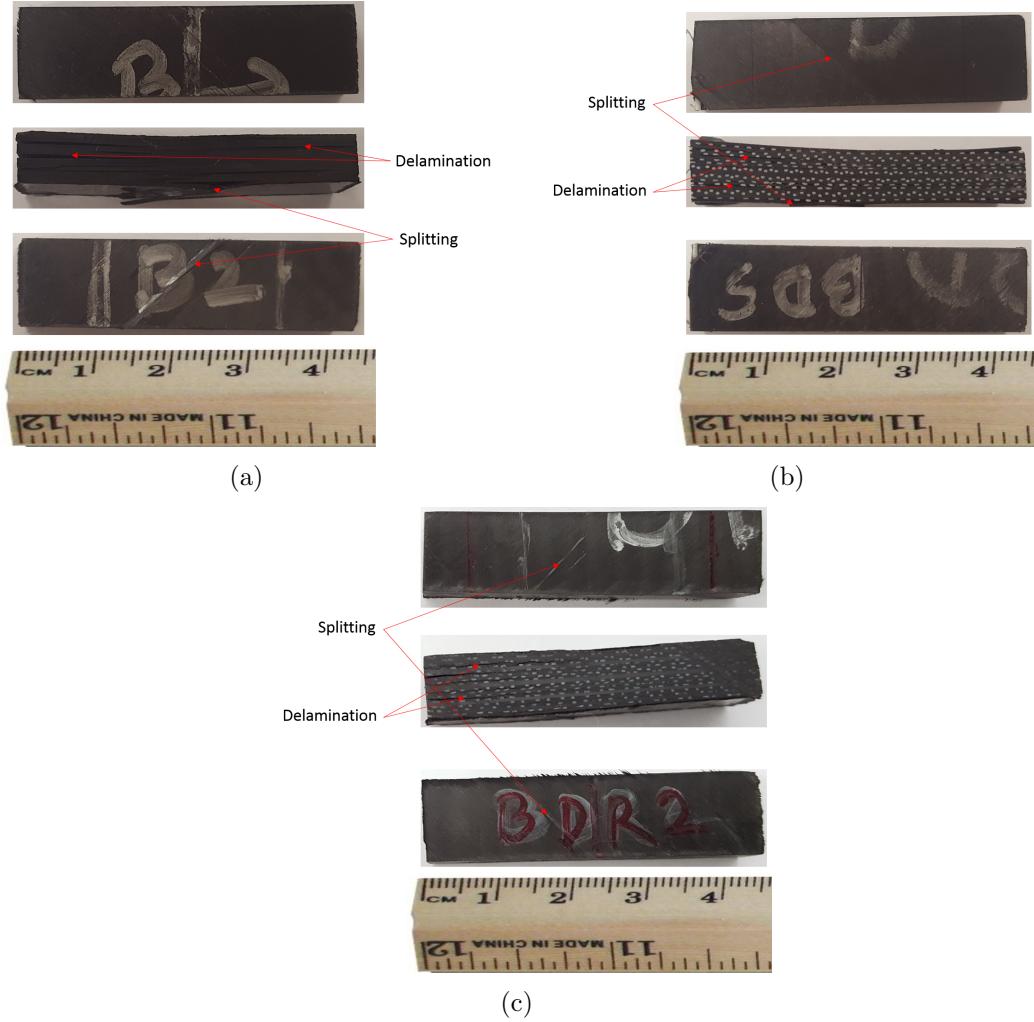


Figure 5.13: Cross section along with top and bottom surfaces of type A laminate (a) pristine, (b) 3D printed inter-laminar region and (c) 3D printed inter-laminar region with additional resin

5.5 Conclusions

In this paper, a novel method to enhance the interlaminar properties of multidirectional laminate is investigated. Additive manufacturing technology is used to increase the ILSS of laminate. Two types of laminate investigated under three different conditions. The ILSS of a 3D printed inter-laminar region laminate is compared to the pristine laminate

and it is found that, for the 3D printed inter-laminar region, the ILSS of type A laminate is increased by approximately 28% and for type B the increase is about 11%. So, use of additive manufacturing technology can significantly increase the ILSS of multi-directional laminate and this method can be used to increase the interlaminar properties.

Chapter 6

Concluding Remarks

6.1 Conclusions

Woven fiber reinforced (carbon and Kevlar[®]) composite materials are exposed to cryogenic environment to study the usefulness of these materials as cryogenic propellant tanks. Tensile, flexural and SBS tests are conducted to determine the thermo-mechanical responses of Kevlar[®] and carbon composites. It is found that, the mechanical properties do not reduce significantly after the cryogenic exposure. Smart design of these composites would allow for lighter, stiffer, tougher and damage resistant propellant tanks.

It is found that woven carbon and Kevlar[®] fiber reinforced composites have the potential to be used in cryogenic tank and then the feasibility of hybrid composites (reinforced by the combination of these two types of fiber) is investigated. Transient heat transfer analysis followed by mechanical stress analysis are conducted on different layer percentages and layer combinations of hybrid composites. Six combinations from the thirty combinations initially investigated are chosen for experimental testing along with 100% carbon and 100% Kevlar[®] fiber composites. Experiments are conducted for 100% carbon and 100% Kevlar[®] fiber composites, which revealed that there is an insignificant reduction in ILSS values for carbon composite, whereas, a reduction of 16.8% is observed for Kevlar[®] fiber composite. The selected hybrid combinations are then computationally and experimentally investigated for cryogenic and gradient cryogenic exposure. Further, Short Beam Shear (SBS) tests are conducted to determine the ILSS of the composites and confirm the optimum hybrid composites that have been chosen based on computational modeling. 8 combinations are examined for Pristine, Cryogenic, and Gradient Exposure. It was observed that the overall ILSS tend to decrease with increasing volume percentage of Kevlar[®] fiber in

the composite. Further, the failure mechanisms are favorable towards a high concentration of carbon fiber in the levels of hybridization, making the 75% Carbon - 25% Kevlar combination [KCKCKC7]_s an optimum hybrid combination.

A modeling framework capable of predicting the interface stress in a multi-directional laminate under thermo-mechanical loading is developed. The accuracy and effectiveness of the present Q-2D model is validated with the previously published results and full 3D model results. Later, this Q-2D model is used to determine the delamination prone interfaces. The interfaces that are most susceptible to delamination, is strengthened by using additive manufacturing technology. Thin lines are 3D printed on pre-pregs and used in the delamination prone interfaces. It is found that this modification of the interface can improve the ILSS by 28 % which is a breakthrough invention in the field of composite materials.

6.2 Future Work

The following are some of the suggestions for future studies-

- Full cryogenic exposure and gradient exposure for short period (6 hours) are studied in this thesis but it is necessary to study the cryogenic exposure for long time and also cyclic exposure study should be conducted to reach into a concrete conclusion.
- Liquid nitrogen is used to study the cryogenic exposure, it is necessary to investigate the permeability of LN_2 through this composites. Also, only mechanical properties are considered but it is also necessary to study the thermal properties of the composites.
- Only one pattern of the 3D printed lines are studied in this thesis. The different properties of 3D printed lines such as line width, line thickness, spacings etc. and also different material such ABS, Nylon etc. should be studied to get an optimum combination of material and line properties.

Appendix A

Computational Modeling of Curing Induced Damage due to Compaction on Woven Fabric Composites

This appendix is published in [113, 114, 115, 116] and addresses the curing induced damage during manufacturing of woven composite by VARTM method. Since, the focus of this thesis is on the cryogenic application and free edge effect in composite materials, the preliminary work carried out for manufacturing induced damage is presented here.

A.1 Introduction

Fiber reinforced polymer matrix composites (FRPCs) are manufactured using a variety of manufacturing processes, predicated on the type of FRPC considered. During this process, the mechanical behavior of the constituents is altered. Therefore, for better design of these laminates, a thorough understanding of the material state is required, and the influence of processing on the subsequent material response in service needs to be quantified. Therefore, along with design aspects like geometrical properties and layup, manufacturing induced effects have to be accounted for. In order to be able to predict the final properties of the structural material, a computational model should also include processing induced effects.

Cure induced stresses and possible micro-damage caused during the cure process are the two predominantly investigated manufacturing induced effects. During the manufacturing of a very thick component, spatial variation in cure development is observed. Rabearison et al. [117] investigated the curing process in thick carbon epoxy tube, and have concluded that the spatial variation during the curing process of thick components cause cracks.

Further, a curing model to predict the residual stress development during the resin transfer molding process in thick laminated cylinders has been studied by Corden et al. [118]. Chemical shrinkage due to cure was identified as a significant mechanism for residual stress generation in the cured components. Further, at the lamina level, interlaminar cracks were observed in the experimental specimens due to the differential shrinkage within layers of a laminate. Many more evidences of crack formation during the curing of composites have been reported in the literature. Plepys and Farris [119] observed crack development during the cure of 3-dimensionally constrained epoxy resin in a glass cylinder.

The curing process is commonly divided into two parts: The first is the chemical reaction, the heat generation and conduction. The second is the generation of stresses and the development of structural integrity. Both parts contribute to the curing process significantly, and need thorough investigation in order to optimize the manufacturing process. The heat equation and the Fouriers Law are commonly employed to model the temperature field. Kamal [120] proposed a phenomenological model which is predominantly used to model the chemical kinetics of curing.

A variety of approaches are followed to model the evolution of stresses during the cure of epoxy. Incremental elasticity theory was used by Plepys and Farris [119] and Plepys et al.[121], to model the evolution of stresses and the elastic properties as a function of the degree of cure. The constitutive law relating the incremental stresses and corresponding incremental strains during any time increment was given by the isotropic linear elastic modulus, which is a function of cure. A theory utilizing the degree of cure, the elastic modulus of uncured and fully cured resin, and a parameter to quantify stress relaxation and chemical hardening was used by Bogetti and Gillespie [122]. Linear viscoelasticity is another commonly used material model for epoxy, where integral constitutive equations are used to evolve cure dependent material properties, was used by Adolf and Chambers [123], Adolf et al.[124], Lange et al.[125]; White and Hahn [126]. Non-linear viscoelasticity theory for modeling curing was proposed by Adolf and Chambers [121]. This method, though very sophisticated in its formulation, requires large number of parameters that need extensive

experimental validation. In the current paper, curing process that includes the chemical and thermal curing of a thermoset polymer matrix along with the stress generation is modeled, which was introduced earlier by Mei [127], Mei et al. [128] and Heinrich et al.[129].

Mesoscale modeling of woven composites are considered in this paper. Previous studies by Song and Waas [130] on composites manufactured using a vacuum assisted resin transfer molding (VARTM) process have shown that the use of original virgin matrix properties in numerical predictions can lead to inaccurate determination of the composite response to loading. The virgin matrix material showed different behavior as opposed to in-situ matrix material behavior obtained from experiments [129]. That is, the presence of fibers in a composite and the curing cycle alter the behavior of the matrix during the curing process. The system undergoes shrinkage due to chemical processing, and thus, builds internal stresses. Depending on the constituent chemistry and thermal cycle that is used during the curing process, a fiber reinforced composite can and may undergo damage and cracking, most likely due to gradients in stress and strain fields, resulting in significant residual stresses. Therefore, it is important to account for curing induced effects on the response of the final laminate used in component design. In this paper, the evolution of temperature and the degree of cure for the matrix material system is determined through a coupled system that considers the heat equation and an empirical curing law [123].

To investigate the effects of curing on the ultimate material behavior, the influence of the curing cycle, the compaction and the constituent material properties on the pre-service stress distribution and possible damage formation through cracking is studied here. The residual stresses developed are a function of the cure progression in the system, and this progression which is related to the temperature field and compaction is also influenced by the presence of fibers within the matrix. Therefore, the temperature distribution, compaction pressure, cure evolution, residual stress development and damage in woven composites are all coupled, and this aspect is investigated in this paper.

A.2 Woven Composite-Mesoscale Model

A.2.1 Geometry of the Representative Volume Element (RVE)

Four layers of woven glass fiber reinforced composite is modeled as shown in Fig. A.1. The model is subjected to a temperature change that is representative of a typical cure cycle. Temperature is applied on all edges of the Representative Volume Element (RVE). Flat boundary conditions are maintained throughout, i.e., the edges are free to expand and contract while remaining straight/flat.

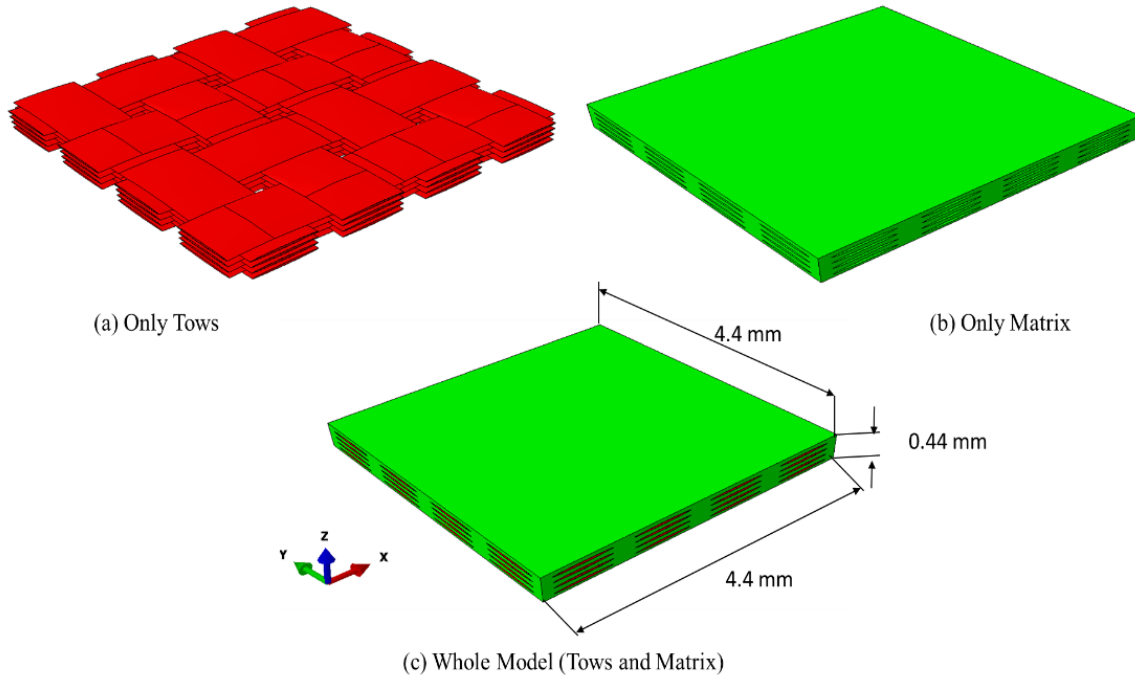


Figure A.1: RVE of woven composite used

A.2.2 Material System

The fiber tows are modeled as transversely isotropic linear elastic material. The properties of the glass fiber used in this model are $E_f = 85$ GPa and $\nu_f = 0.2$. The homogenized tow properties (shown in Table A.1), were calculated for the properties of fiber and matrix using the

concentric cylinder model [131]. Other tow properties required for the curing model are density, specific heat constant and thermal conductivity (refer to Table A.2).

Table A.1: Tow properties

E_1 (GPa)	$E_2 = E_3$ (GPa)	$\nu_{12} = \nu_{13}$	ν_{23}	$G_{12} = G_{13}$ (GPa)	G_{23} (GPa)	ρ (kg/m ³)	c_p (J/kg/K)	K (W/m/K)
51.034	0.254	0.307	0.2142	0.111	0.105	2480	737	1.3

The matrix material is initially a liquid resin, which is cured to form a solid material. That is, the elastic modulus of the matrix evolves with curing. The variation of the mechanical properties of the matrix with curing is explained in detail in the following sections. The density, specific heat and thermal conductivity of the epoxy are given in Table A.2.

Table A.2: Matrix properties

ρ (kg/m ³)	c_p (J/kg/K)	K (W/m/K)
1200	1200	0.2

A.3 Curing Model for Resin

A.3.1 Evolution of Temperature and the Degree of Cure

Curing of Epon862 (matrix material) with curing agent EPIKURE 9553 is modeled here. The degree of cure in the matrix is given by,

$$\phi(t) = \frac{H(t)}{H_r} \quad (\text{A.1})$$

where, $H(t)$ is the heat generated and $\phi(t)$ is the degree of cure at time t . Therefore, the rate of heat generated during the curing process is,

$$r = \frac{dH(t)}{dt} = \frac{d(\phi(t)H_r)}{dt} \quad (\text{A.2})$$

The process of curing of an epoxy is modeled by a curing kinetics equation of a highly exothermic chemical reaction given by,

$$\frac{\partial \phi(t)}{\partial t} = f(T, \phi) \quad (\text{A.3})$$

$$\begin{aligned} f(T, \phi) &= (k_1(T) + k_2(T)\phi^m)(1 - \phi)^n \\ k_1(T) &= A_1 \exp\left(-\frac{\Delta E_1}{TR}\right) \\ k_2(T) &= A_2 \exp\left(-\frac{\Delta E_2}{TR}\right) \end{aligned} \quad (\text{A.4})$$

where, m and n are constants, R is the gas constant, A_1 and A_2 are frequency like constants, ΔE_1 and ΔE_2 are activation energies.

From the first law of thermodynamics, the heat equation accounting for the heat generated and conducted during the process of curing is given by,

$$\rho c_p \frac{\partial T}{\partial t} = \frac{\partial}{\partial x} \left(K \frac{\partial T}{\partial x} \right) + \rho \frac{d(\phi(t)H_r)}{dt} \quad (\text{A.5})$$

The above equation is a one way coupled non-linear partial differential equation for spatial and temporal variation of temperature $T(x,t)$ and the corresponding degree of cure. A non-linear least squares approach was used to fit the experimental data. The parameters A_1 and ΔE_1 were free to vary, while fixing the remained parameters as: $n = 1$, and $A_2 = \Delta E_2 = m = 0$. Therefore, the only two parameters of the curing model are A_1 and ΔE_1 with values of $3.62 \times 10^{11} \text{ sec}^{-1}$ and $8.854 \times 10^{10} \text{ J}$ respectively. Using the above model, the temporal and spatial distribution of temperature within the model is determined by numerically solving equation A.5.

A.3.2 Evolution of Stresses during Curing

A model for the evolution of stress given in Heinrich et al. [129], and similar to models given in [127] and [132], incorporating the concept of network formation and its contribution to stress evolution is used here. In this model, the epoxy resin, which is the matrix used, is

initially mixed with a hardener in the liquid state. The mixture is poured over fibers in a mold. The pure epoxy starts to harden upon mixing through the formation of connections and cross links. The entire configuration is initially stress free, and at time t_1 , the first network forms, which is accompanied by cure shrinkage, along with additional strains due to external loads or other thermal effects. A second network forms at a later time t_2 , but with a different reference configuration. The process of network formation continues, and the reference configuration is different from the previous network formed. But, the current configuration is the same for all the networks, since they occupy the same volume. This results in different stresses in each network. The externally applied loads are balanced out by the sum of stresses in all of the networks formed at any time. The stress $\sigma(t, s)$ at time t in a network formed at time s is proportional to the mechanical strain $\epsilon_{mech}(t, s)$ relative its stress free configuration, with a proportionality constant $E(s)$, which is the elastic modulus of the network.

$$\sigma(t, s) = E(s)\epsilon_{mech}(t, s) \quad (\text{A.6})$$

The total strain at time t in a network formed at time s is given by the sum of all incremental strain since s , which is the time corresponding to its creation. Therefore, the total strain is given by,

$$\begin{aligned} \epsilon(t, s) &= \Delta\epsilon(s) + \Delta\epsilon(s + \Delta t) + \dots + \Delta\epsilon(t) \\ &= \epsilon_{mech}(t, s) + \alpha(s) \Delta (T(t) - T(s)) - \epsilon_c(s) \end{aligned} \quad (\text{A.7})$$

where, $\alpha(s)$ is the coefficient of thermal expansion and $\epsilon_c(s)$ is the cure shrinkage of the network formed at time s .

The evolution of stress with time (detailed derivation can be found in [129]) in 1D, is given by,

$$\sigma(t) = \int_0^t \frac{d\phi}{ds} E(s) (\epsilon(t) - \epsilon(s) - \alpha(T(t) - T(s)) + \epsilon_c(s)) ds \quad (\text{A.8})$$

The above equation can be generalized to 3D as given in [129]:

$$\begin{aligned} \sigma(t) = \int_0^t \frac{d\phi}{ds} \underline{1} \left[K(s) \text{tr} \left(\underline{\epsilon}(t) - \underline{\epsilon}(s) + \underline{\epsilon}_c(s) - \underline{1} \alpha(s) \triangle T(t, s) \right) \right. \\ \left. + 2\mu(s) \left(\underline{\epsilon}(t) - \underline{\epsilon}(s) + \underline{\epsilon}_c(s) - \underline{1} \frac{1}{3} \text{tr} \left(\underline{\epsilon}(t) - \underline{\epsilon}(s) + \underline{\epsilon}_c(s) \right) \right) \right] \\ + (1 - \phi(t)) K_{liquid} \underline{1} (\underline{\epsilon}(t) - \underline{1} \alpha_{liquid} \triangle T(t)) \end{aligned} \quad (\text{A.9})$$

where, K , μ , α and $\underline{\epsilon}_c$ are the per network bulk modulus, shear modulus, coefficient of thermal expansion and cure shrinkage, respectively are the inputs to the model. These per network input parameters are extracted from the plane wave modulus, shear modulus and degree of cure determined experimentally for the entire epoxy system. The variation of the elastic modulus E with respect to the degree of cure ϕ is shown in Fig. A.2.

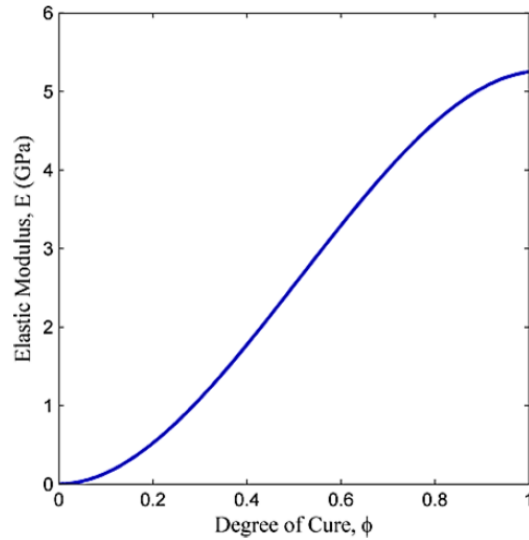


Figure A.2: Variation of elastic modulus with respect to the degree of cure

Variation of the plane wave modulus ($M_{tot}(\phi)$) and the shear modulus ($\mu_{tot}(\phi)$) with the

degree of cure (ϕ) for the epoxy system is given in A.2. It is shown that the corresponding per network quantities ($M_{tot}(\phi)$ and $\mu_{tot}(\phi)$) can be obtained as,

$$\begin{aligned} M(\phi) &= \frac{dM_{tot}(\phi)}{d\phi} + K_{liquid} \\ \mu(\phi) &= \frac{d\mu_{tot}(\phi)}{d\phi} \end{aligned} \tag{A.10}$$

The corresponding per network bulk modulus is $K = M - \frac{4}{3}\mu$. Therefore, using this approach, the variation of the per network bulk modulus and the shear modulus with respect to the degree of cure is obtained. This model is used here to determine the stress evolution and solidification of the matrix in the presence of fiber tows.

A.3.3 Modeling Damage due to Cure Shrinkage with Crack Band Model

Due to excessive cure shrinkage and residual stress build up during the curing process, matrix can degrade in the presence of fibers and fiber tows. Therefore, stress evolution should account for damage due to curing. A new methodology is formulated to incorporate the possible damage occurrence due to excessive strain in the epoxy. Towards that, a third dimension is added to the evolution of the material properties (like the elastic modulus, E) with degree of cure ϕ . That is, the material properties are a function of the degree of cure (ϕ) as well as the amount of strain accumulated in the material, beyond a chosen critical degree of cure (ϕ_{cr}). The critical degree of cure (ϕ_{cr}) can be chosen to be a value where the matrix has cured sufficiently.

The matrix properties are degraded through a physics based approach. The degradation of the material is dictated by the amount of energy dissipated over a fracture process zone during damage, which is governed by a cohesive law. Thus, the elastic modulus shown in Fig. 3(a), which is a function of ϕ only, is extended to a surface law as shown in Fig. 3(b)

(here, ϕ_{cr} is chosen to be 0.7) .

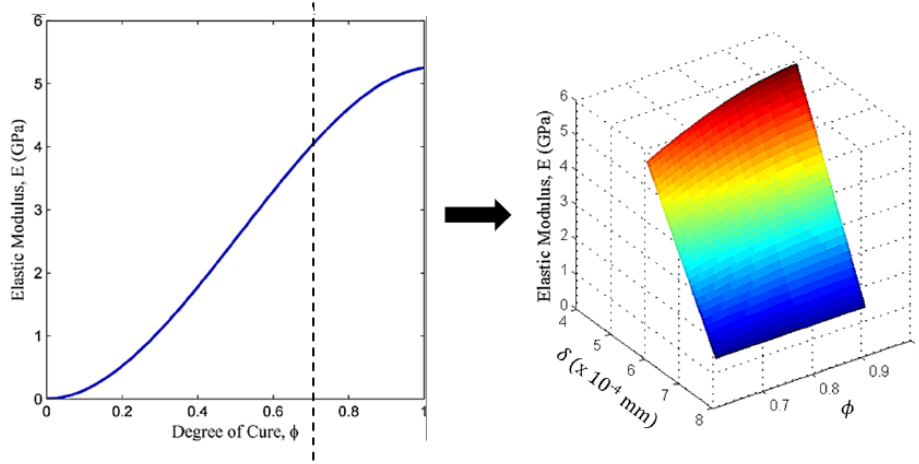


Figure A.3: Variation of the elastic modulus with respect to the degree of cure and separation (from cohesive law) in the material

Including damage capability in materials adds a region with negative tangent stiffness to the constitutive law. Classical finite element method (FEM) converges to a single solution with mesh refinement, as long as the tangent stiffness of the constitutive law is greater than or equal to zero. But, a negative tangent in the constitutive law makes the model pathologically mesh dependent. That is, the results change as the element size is reduced. Therefore, the energy dissipated during the failure process has to be scaled with the element size to make the problem mesh objective. Crack band model (CBM) introduced by Bazant and Oh [133] is an efficient method to account for the element size during material damage.

The damaging regime is modeled by adding a traction-strain law beyond a critical strength value in the constitutive law. The traction-strain law is determined by converting a traction-separation law utilizing the characteristic element length L as shown in Fig. A.4. The two inputs to the traction-separation law are the cohesive/critical strength (σ_c) and fracture toughness (G_c) of the material.

In CBM, a typical stress-strain material law is generated by adding a linearly decreasing damage path, with the characteristic length included, to follow the initial linearly increasing

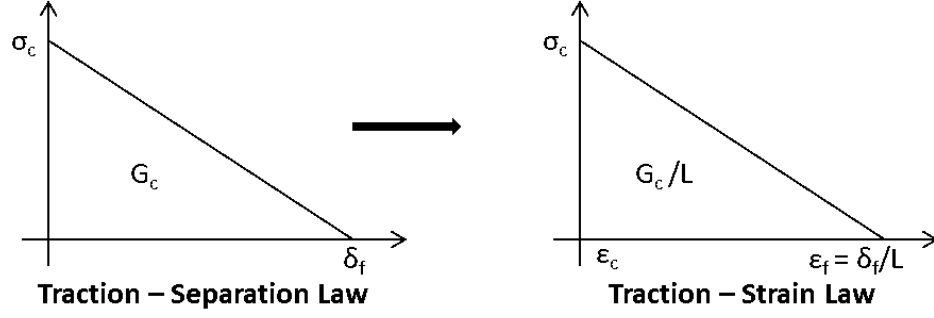


Figure A.4: Converting traction-separation law to traction-strain law

regime as shown in Fig. A.5. The initial linear stiffness of the material is E , which is a function of the degree of cure. As the strain within an element in the FEM model exceeds the critical strain corresponding to the critical stress, the stiffness of the element is reduced accordingly by entering the damage path in Fig. A.5. The degraded stiffness value is determine as $E = \sigma_i/\epsilon_i$, corresponding to the strain in the element.

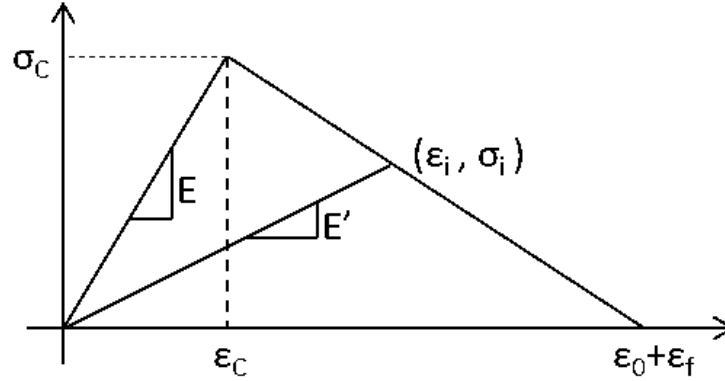


Figure A.5: CBM: modified stress-strain material law incorporating failure

After the entire fracture toughness is dissipated, the material is declared to have completely failed. Therefore, using the method described above, the surface plot shown in Fig. A.3 is generated as required for the damaging elements accounting for their characteristic lengths in the FEM model. It is assumed that the material starts to degrade (reduction in stiffness) beyond a critical stress (σ_c) value, corresponding to the degree of cure. This

critical stress is a function of the degree of cure. Further, the fracture energy released upon complete failure of the material is also dependent on the degree of cure. That is, the fracture energy associated with a more ductile material (partially cured) is higher than that of a material with less ductility (fully cured). But, in this paper, it is assumed that both σ_c and G_c remain constant, and are independent of the degree of cure, (ϕ).

A.4 Curing Study with Matrix Degradation

The method described above is a framework for modeling the curing process accounting for damage during curing. Three steps are involved in determining the effects of curing on the quality of the final RVE. The steps are discussed in detail in the following sections.

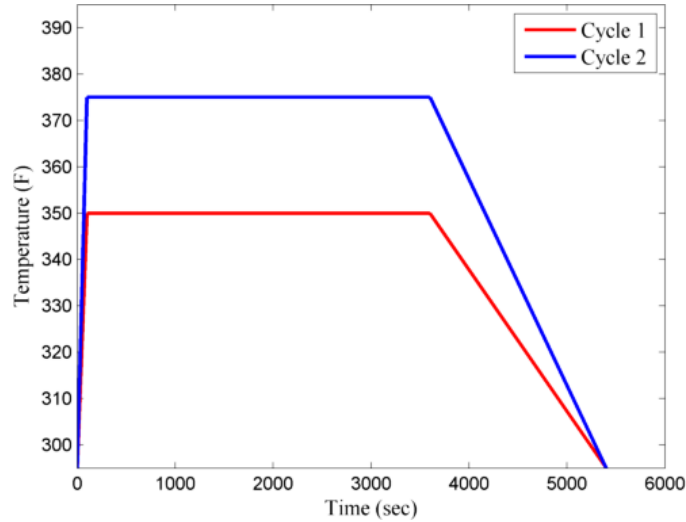


Figure A.6: Curing cycles

Step 1: Determine the temperature distribution in the RVE

Two different curing cycles are considered in this paper. The temperatures are raised to 350 K and 375 K from the room temperature (295 K) to accelerate the curing process. The cure cycles are shown in Fig. A.6. By numerically solving the heat transfer equation given in equation A.5, the temperature distribution in the model due to external heat imparted as well as internal heat generated due to curing of the epoxy is determined.

Step 2: Cured State of the RVE

A.5 Effect of Temperature Cycle

Temperature distribution over the model with time (from Step 1) is used in this step to determine the solidification/curing of the epoxy, and its effect on the curing process. For each cure cycle, the post cure state of the model is investigated for 4 different critical stresses (σ_c). The regions where damage has been initiated due to curing are shown in red in Fig. A.7 and Fig. A.8 corresponding to $\sigma_c = 45, 60, 75$ and 90 MPa.

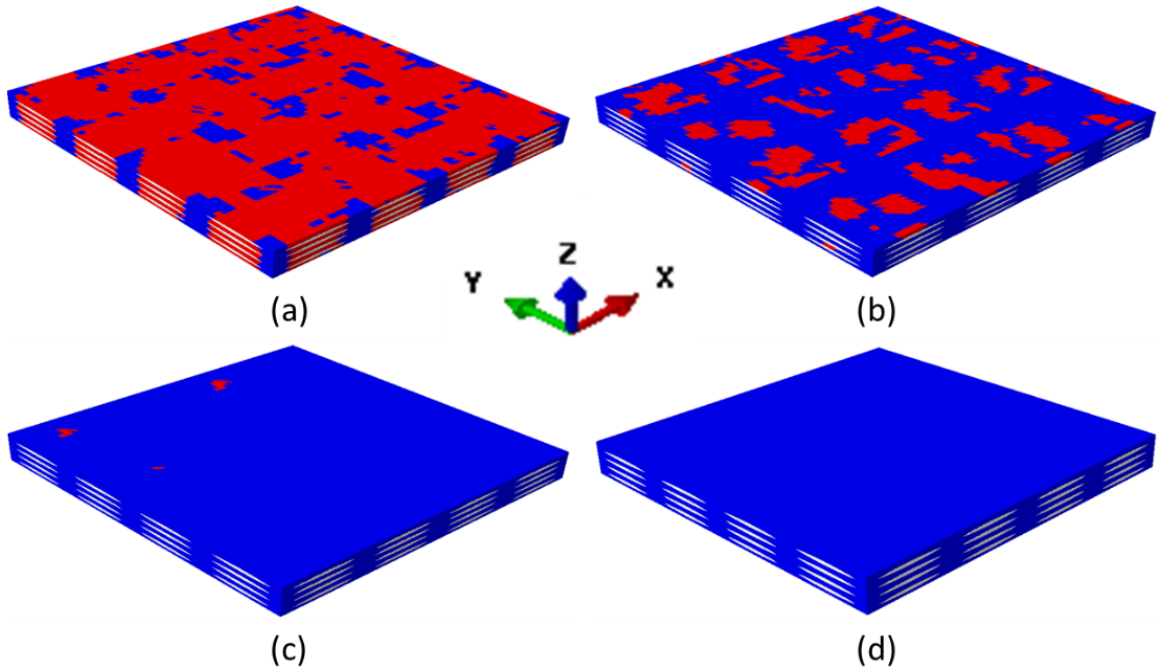


Figure A.7: Cure Cycle 1: Damage initiated regions corresponding to critical stress of (a) 45 MPa, (b) 60 MPa, (c) 75 MPa and (d) 90 MPa

The degradation of the matrix appears to depend on the cure cycle as well as the critical stress values. For cure cycle 1, where the maximum external temperature applied is 350 K, the damage initiated regions (red color) the matrix reduces with increase in matrix

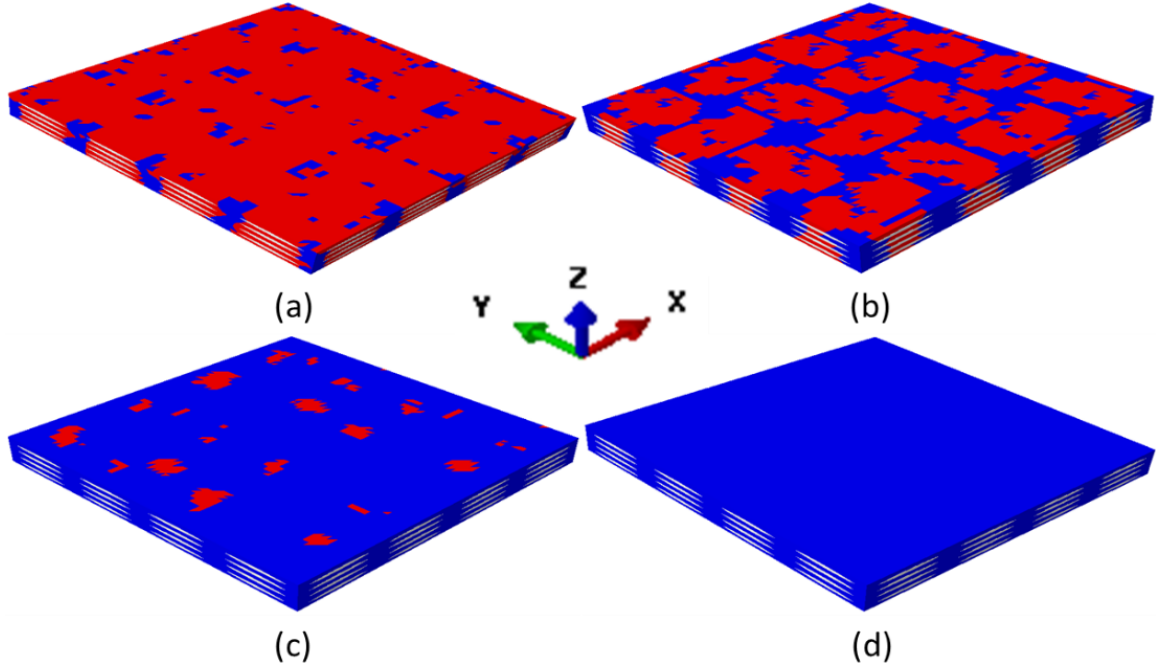


Figure A.8: Cure Cycle 2: Damage initiated regions corresponding to critical stress of (a) 45 MPa, (b) 60 MPa, (c) 75 MPa and (d) 90 MPa

critical stress. Same trend was also observed for curing cycle 2, where the maximum applied temperature was 375 K. For all these cases, it is observed that the area of damage initiated regions decrease with increase in the critical stress of the damage model. That is, maximum damaged regions are observed in the case of $\sigma_c=45$ MPa and almost no damage corresponding to 90 MPa. Clearly, the amount of degradation and subsequent failure, which are governed by the stress (and strain) evolution in the matrix will change based on the critical strength and fracture toughness of the matrix material. Fig. A.9 and Fig. A.10 show the failed regions in the matrix for different curing cycles. Damage initiated regions refer to the points in the degrading regime of the traction-strain law, whereas failed regions refer to the points where the material has lost all load carrying capacity completely.

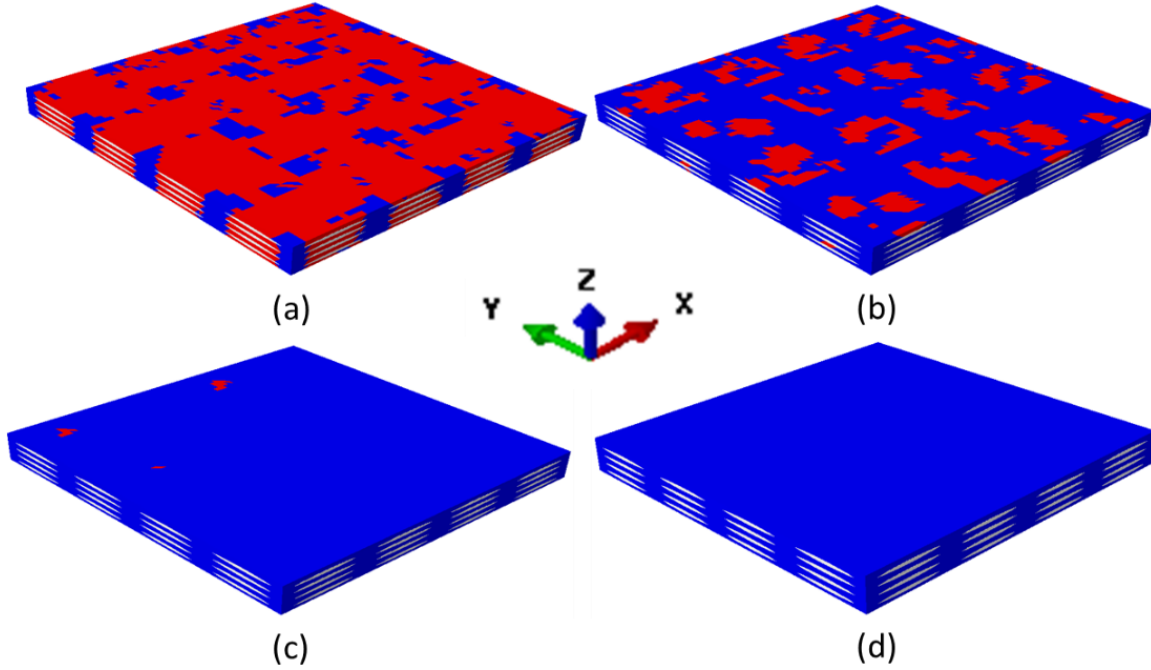


Figure A.9: Cure Cycle 1: Failed regions corresponding to critical stress of (a) 45 MPa, (b) 60 MPa, (c) 75 MPa and (d) 90 MPa

A.6 Effect of Compaction

The influence of compaction on the quality of the composite is investigated in this section. The compaction acting on the composite is due to the mold pressure during the manufacturing of textile composites. Several researchers have measured the extent of mold pressure after the injection process. Rudd [134] has reported mold pressures of upto 15 bar and Ikegawa et al. [135] has reported 20-50 bar. For compression molding of sheet molding compound, Revello [136] has reported mold pressure of 35-140 bar, whereas for compression molding Charrier [137] quotes mold pressure of 35-700 bar. In the current work, the influence of mold pressure of upto 50 bar is investigated. Failed regions corresponding to compaction pressure of 15 (1.5 MPa), 30 (3 MPa) and 50 (5 MPa) bar for the composite subjected to cure cycle 1, and critical stress of 60 MPa are reported in Fig. A.11 and

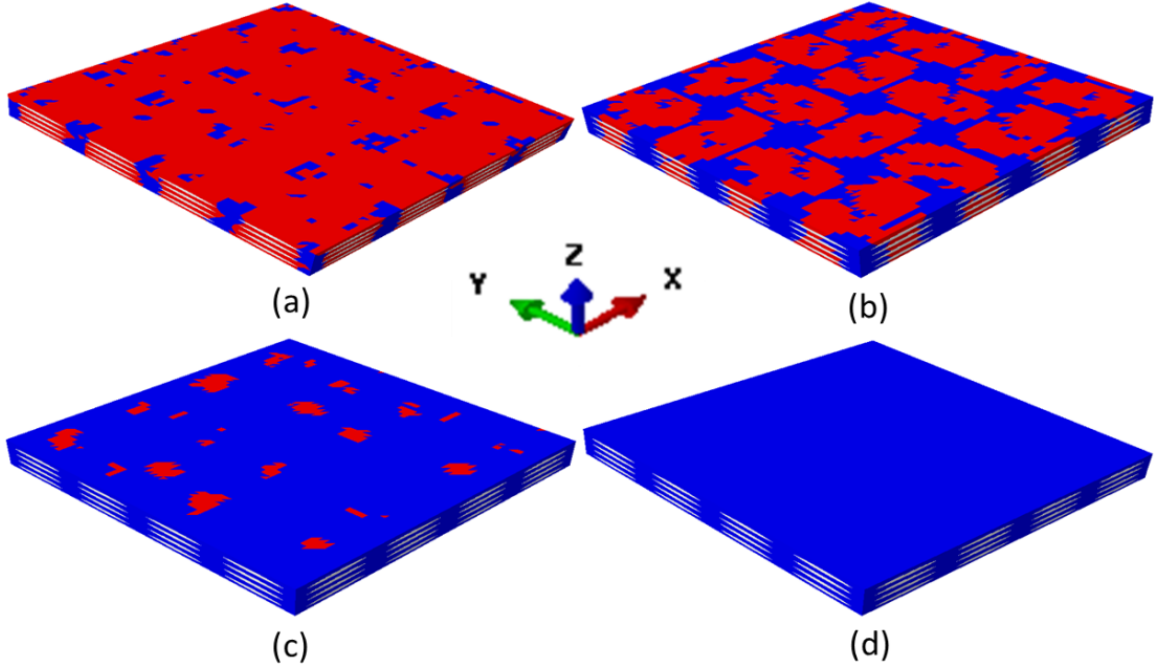


Figure A.10: Cure Cycle 2: Failed regions corresponding to critical stress of (a) 45 MPa, (b) 60 MPa, (c) 75 MPa and (d) 90 MPa

Fig. A.12.

From Fig. A.11 and Fig. A.12, it is evident that the extent of failure increases with increasing compaction or mold pressure. Similar trend is observed for critical stress of 45 MPa and 60 MPa. To ensure minimum to no failure during the manufacturing process, it is therefore important to investigate the space of cure cycle, compaction and material properties of the matrix to improve the design process of such polymer matrix composites. The computational framework developed in this paper serves as the tool to investigate influence of various manufacturing process parameters on the quality of the composite manufactured.

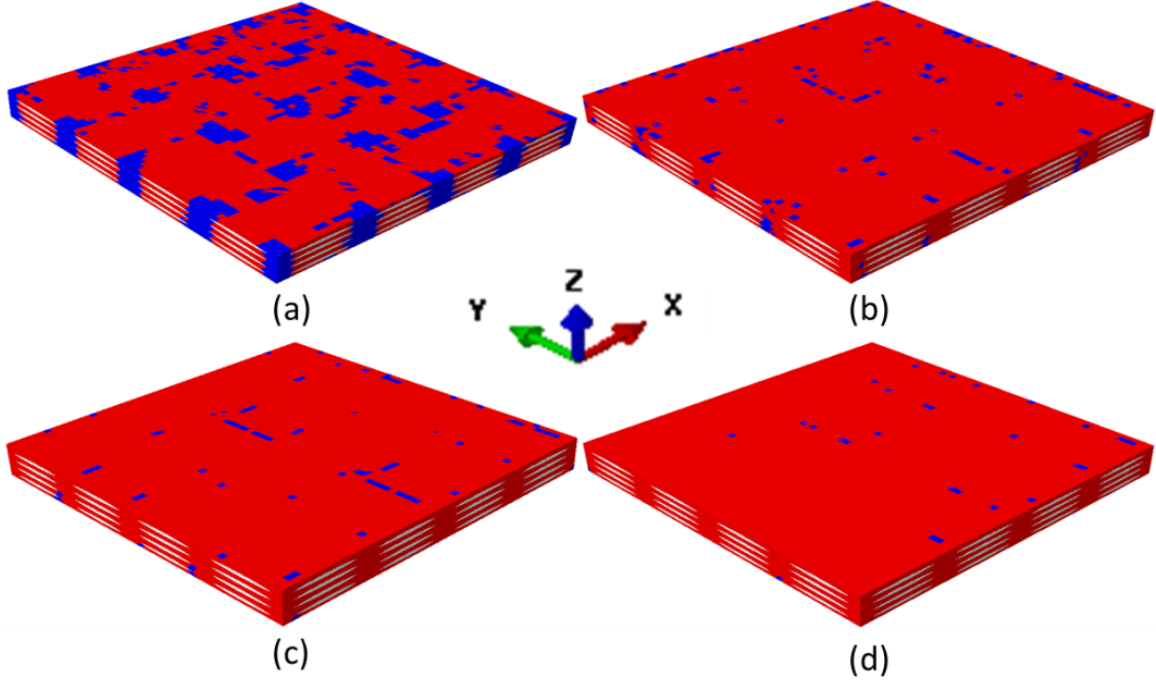


Figure A.11: Cure Cycle 1: Failed regions corresponding to critical stress of 45 MPa for a compaction of (a) 0 MPa, (b) 1.5 MPa, (c) 3 MPa and (d) 5 MPa

A.7 Conclusion

In this paper, a mesoscale investigation of the effects of the curing process on woven composites is presented. Woven composite with four layers of glass fabric in epoxy was modeled. It was observed that the cure cycle has a significant influence on the final response of the RVE. The cure shrinkage, the strength, the fracture toughness and the chemical properties of the epoxy influence the final material properties of the RVE. Specifically, the damage caused by different cure cycles and mold pressures on the composite was studied. The degradation in the matrix due to the presence of fiber tows in the context of woven composites was predicted. This type of initial predictions of the post cure state of the composite prior to manufacturing it will assist in the initial design of the manufacturing process. Using the computational tool developed, optimum cure cycles, mold pressures and strength of the

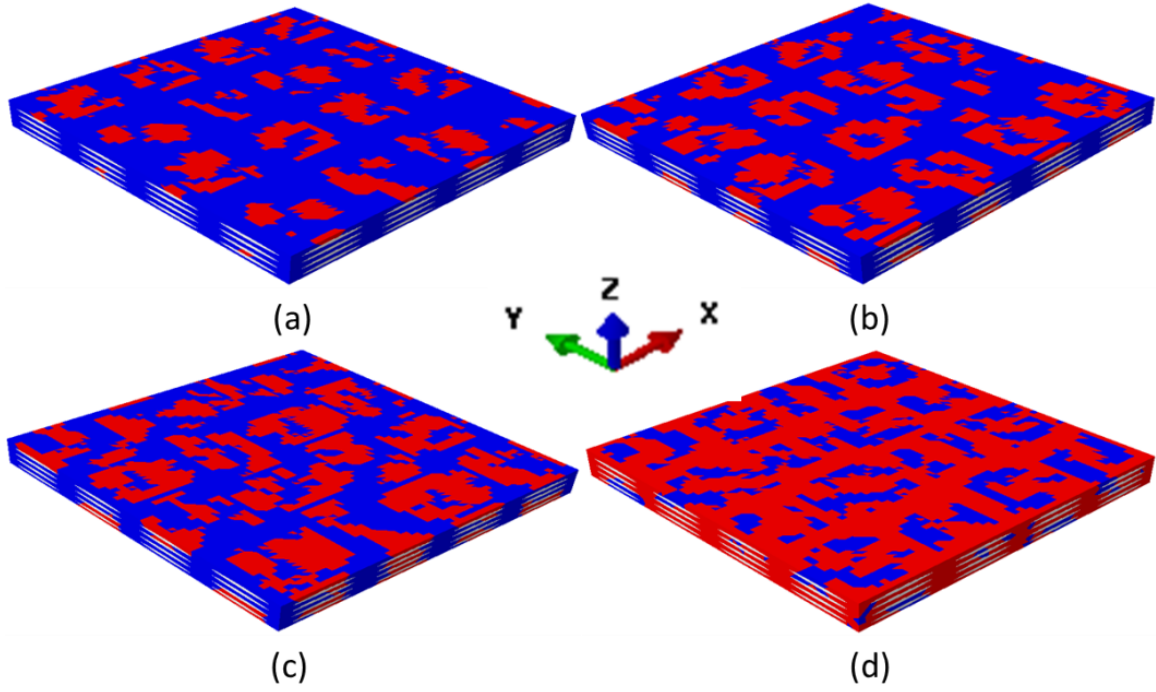


Figure A.12: Cure Cycle 1: Failed regions corresponding to critical stress of 60 MPa for a compaction of (a) 0 MPa, (b) 1.5 MPa, (c) 3 MPa and (d) 5 MPa

epoxy to be used for a particular woven composite can be assessed prior to manufacturing, and several trial and error steps can be minimized.

References

- [1] X. Song. Vacuum assisted resin transfer molding (vartm): model development and verification. 2003.
- [2] K. M. Chittajallu. *Computational Modeling of the Vacuum Assisted Resin Transfer Molding (VARTM) Process*. PhD thesis, Clemson University, 2004.
- [3] A. Belvin, S. K. Borowski, and J. Scott. The nuclear cryogenic propulsion stage. 2014.
- [4] J. H. Vickers. Composite australia conference composite cryotank project structures for launch vehicles. 2013.
- [5] S. Choi and B.V. Sankar. Fracture toughness of transverse cracks in graphite/epoxy laminates at cryogenic conditions. *Composites Part B: Engineering*, 38(2):193 – 200, 2007.
- [6] D.E. Steitz. Nasa tests game changing composite cryogenic fuel tank. *NASA Web.*, 16 Dec. 2013.
- [7] R. Sadeghian, S. Gangireddy, B. Minaie, and K. Hsiao. Manufacturing carbon nanofibers toughened polyester/glass fiber composites using vacuum assisted resin transfer molding for enhancing the mode-i delamination resistance. *Composites Part A: applied science and manufacturing*, 37(10):1787–1795, 2006.
- [8] A. J. Rodriguez, M. E. Guzman, C. Lim, and B. Minaie. Mechanical properties of carbon nanofiber/fiber-reinforced hierarchical polymer composites manufactured with multiscale-reinforcement fabrics. *Carbon*, 49(3):937–948, 2011.
- [9] L. Lin, J. Lee, C. Hong, G. Yoo, and S. G. Advani. Preparation and characterization of layered silicate/glass fiber/epoxy hybrid nanocomposites via vacuum-assisted resin

- transfer molding (varm). *Composites Science and Technology*, 66(13):2116–2125, 2006.
- [10] A. D. Kelkar, J. S. Tate, and P. Chaphalkar. Performance evaluation of varm manufactured textile composites for the aerospace and defense applications. *Materials Science and Engineering: B*, 132(1):126–128, 2006.
 - [11] B. V. Sankar and R. V Marrey. Analytical method for micromechanics of textile composites. *Composites Science and Technology*, 57(6):703–713, 1997.
 - [12] S. V. Lomov and I. Verpoest. Textile composite materials: Polymer matrix composites. *Encyclopedia of Aerospace Engineering*, 2010.
 - [13] S. B. Sharma and M. P. F. Sutcliffe. Draping of woven composites over irregular surfaces. In *Proceedings of the 13th International Conference on Composite Materials (ICCM-13), Beijing, China*, 2001.
 - [14] K. D. Potter. The influence of accurate stretch data for reinforcements on the production of complex structural mouldings: Part 1. deformation of aligned sheets and fabrics. *Composites*, 10(3):161–167, 1979.
 - [15] V. T. Bechel, M. B. Fredin, S. L. Donaldson, R. Y. Kim, and J. D. Campling. Effect of stacking sequence on micro-cracking in a cryogenically cycled carbon/bismaleimide composite. *Composites Part A: Applied Science and Manufacturing*, 34(7):663–672, 2003.
 - [16] V. T. Bechel and R. Y. Kim. Damage trends in cryogenically cycled carbon/polymer composites. *Composites science and technology*, 64(12):1773–1784, 2004.
 - [17] V. T. Bechel, M. Negilski, and J. James. Limiting the permeability of composites for cryogenic applications. *Composites Science and Technology*, 66(13):2284–2295, 2006.

- [18] J. Noh and J. Whitcomb. Effect of laminate design and loads on crack opening volume in laminates used in cryogenic tanks. *Journal of Composites Technology and Research*, 25(3):171–178, 2003.
- [19] S. Roy, A. Utturkar, and A. Nair. Modeling and characterization of permeability and damage of graphite/epoxy at cryogenic temperature. In *Proceedings of the 46th AIAA/ASME/ASCE/AHS/ASC SDM conference, Austin, TX*, pages 2005–2088, 2005.
- [20] T. Yokoeki, T. Aoki, and T. Ishikawa. Experimental cryogenic gas leakage through damaged composite laminates for propellant tank application. *Journal of Spacecraft and rockets*, 42(2):363–366, 2005.
- [21] V.T. Bechel. Helium flow through cryogenically pre-conditioned composite laminates. In *Proceedings of the 50th SAMPE international symposium, Long Beach, CA*, 2005.
- [22] H. Kumazawa, T. Aoki, and I. Susuki. Analysis and experiment of gas leakage through composite laminates for propellant tanks. *AIAA journal*, 41(10):2037–2044, 2003.
- [23] H. K. Rivers, J. G. Sikora, and S. N. Sankaran. Detection of hydrogen leakage in a composite sandwich structure at cryogenic temperature. *Journal of spacecraft and rockets*, 39(3):452–459, 2002.
- [24] V. T. Bechel, J. D. Camping, and R. Y. Kim. Cryogenic/elevated temperature cycling induced leakage paths in pmcs. *Composites Part B: Engineering*, 36(2):171–182, 2005.
- [25] M. Gong, X.F. Wang, and J.H. Zhao. Experimental study on mechanical behavior of laminates at low temperature. *Cryogenics*, 47(1):1–7, 2007.
- [26] S. Disdier, J.M. Rey, P. Pailler, and A.R. Bunsell. Helium permeation in composite materials for cryogenic application. *Cryogenics*, 38(1):135–142, 1998.

- [27] D. Verstraete, P. Hendrick, P. Pilidis, and K. Ramsden. Hydrogen fuel tanks for subsonic transport aircraft. *International journal of hydrogen energy*, 35(20):11085–11098, 2010.
- [28] S.M. Aceves, J. Martinez-Frias, and O. Garcia-Villazana. Analytical and experimental evaluation of insulated pressure vessels for cryogenic hydrogen storage. *International Journal of Hydrogen Energy*, 25(11):1075–1085, 2000.
- [29] Y. Shindo, R. Wang, and K. Horiguchi. Analytical and experimental studies of short-beam interlaminar shear strength of g-10cr glass-cloth/epoxy laminates at cryogenic temperatures. *Journal of engineering materials and technology*, 123(1):112–118, 2001.
- [30] M. S. Kumar, N. Sharma, and B.C. Ray. Microstructural and mechanical aspects of carbon/epoxy composites at liquid nitrogen temperature. *Journal of Reinforced Plastics and Composites*, 00(00), 2008.
- [31] I. G. Tapeinos and S. Koussios. Experimental study on various liner materials for cryogenic liquid hydrogen storage. *Materials*, 6(1), 2013.
- [32] T.J. Lu and N.A. Fleck. The thermal shock resistance of solids. *Acta Materialia*, 46(13):4755 – 4768, 1998.
- [33] D. Bender, J. Schuster, and D. Heider. Flow rate control during vacuum-assisted resin transfer molding (vartm) processing. *Composites Science and Technology*, 66(13):2265–2271, 2006.
- [34] K. T. Hsiao, R. Mathur, S. G. Advani, J. W. Gillespie, and B. K. Fink. A closed form solution for flow during the vacuum assisted resin transfer molding process. *Journal of manufacturing science and engineering*, 122(3):463–475, 2000.
- [35] B. W. Grimsley, P. Hubert, X. Song, R. J. Cano, A. C. Loos, and R. B. Pipes. Flow and compaction during the vacuum assisted resin transfer molding process. *Proceedings of th International SAMPE Symposium, Seattle, WA*, 2001.

- [36] R. Mathuw, S. G. Advani, D. Heider, C. Hoffmann, J. W. Gillespie, and B. K. Fink. Flow front measurements and model validation in the vacuum assisted resin transfer molding process. *Polymer Composites*, 22(4):477–490, 2001.
- [37] X. Sun, S. Li, and L. J. Lee. Mold filling analysis in vacuum-assisted resin transfer molding. part i: Scrimp based on a high-permeable medium. *Polymer Composites*, 19(6):807–817, 1998.
- [38] J. Ju, B. D. Pickle, R. J. Morgan, and J. N. Reddy. An initial and progressive failure analysis for cryogenic composite fuel tank design. *Journal of Composite Materials*, 41(21):2545–2568, 2007.
- [39] R. C. Goetz, R. S. Ryan, and A. F. Whitaker. Final report of the X-33 liquid hydrogen tank test investigation team. *Marshall Space Flight Center, Huntsville, AL*, 2000.
- [40] ASTM Standard. D3039/D3039 M, 2008, Standard Test Method for Tensile Properties of Polymer Matrix Composite Materials, ASTM International, West Conshohocken, PA, 2003.
- [41] ASTM Standard. D7264/D7264 M, 2007, Standard Test Method for Flexural Properties of Polymer Matrix Composite Materials, ASTM International, West Conshohocken, PA, 2003.
- [42] ASTM Standard. D2344/D2344 M, 2013, Standard Test Method for Short-Beam Strength of Polymer Matrix Composite Materials and Their Laminates, ASTM International, West Conshohocken, PA, 2003.
- [43] P. Prabhakar and A. M. Waas. Interaction between kinking and splitting in the compressive failure of unidirectional fiber reinforced laminated composites. *Composite Structures*, 98:85–92, 2013.

- [44] P. Prabhakar and A. M. Waas. Micromechanical modeling to determine the compressive strength and failure mode interaction of multidirectional laminates. *Composites Part A: Applied Science and Manufacturing*, 50:11–21, 2013.
- [45] M. S. Islam, E. Melendez-Soto, A. G. Castellanos, and P. Prabhakar. Investigation of woven composites as potential cryogenic tank materials. *Cryogenics*, 72:82–89, 2015.
- [46] D. Zhang, J. Ye, and H.Y. Sheng. Free-edge and ply cracking effect in cross-ply laminated composites under uniform extension and thermal loading. *Composite structures*, 76(4):314–325, 2006.
- [47] M. Tahani and A. Nosier. Free edge stress analysis of general cross-ply composite laminates under extension and thermal loading. *Composite Structures*, 60(1):91–103, 2003.
- [48] A.H. Puppo and H.A. Evensen. Interlaminar shear in laminated composites under generalized plane stress. *Journal of composite materials*, 4(2):204–220, 1970.
- [49] N.J. Pagano. On the calculation of interlaminar normal stress in composite laminate. *Journal of Composite Materials*, 8(1):65–81, 1974.
- [50] P.W. Hsu and C.T. Herakovich. Edge effects in angle-ply composite laminates. *Journal of Composite Materials*, 11(4):422–428, 1977.
- [51] S. Tang. A boundary layer theory-part i: Laminated composites in plane stress. *Journal of composite materials*, 9(1):33–41, 1975.
- [52] J.L. Davet and Ph. Destuynder. Free-edge stress concentration in composite laminates: A boundary layer approach. *Computer methods in applied mechanics and engineering*, 59(2):129–140, 1986.
- [53] C.C. Lin and C.C. Ko. Method for calculating the interlaminar stresses in symmetric laminates containing a circular hole. *AIAA journal*, 30(1):197–204, 1992.

- [54] R.B. Pipes and N.J. Pagano. Interlaminar stresses in composite laminatesan approximate elasticity solution. *Journal of Applied Mechanics*, 41(3):668–672, 1974.
- [55] N.J. Pagano. Stress fields in composite laminates. *International Journal of Solids and Structures*, 14(5):385–400, 1978.
- [56] S.G. Leknitskii and P. Fern. *Theory of elasticity of an anisotropic elastic body*. Holden-Day, 1963.
- [57] S.S. Wang and I. Choi. Boundary-layer effects in composite laminates: Part 1free-edge stress singularities. *Journal of Applied Mechanics*, 49(3):541–548, 1982.
- [58] S.S. Wang and I. Choi. Boundary-layer effects in composite laminates: Part 2free-edge stress solutions and basic characteristics. *Journal of Applied Mechanics*, 49(3):549–560, 1982.
- [59] S.S. Wang and I. Choi. The interface crack between dissimilar anisotropic composite materials. *Journal of applied mechanics*, 50(1):169–178, 1983.
- [60] S.S. Wang and I. Choi. The interface crack behavior in dissimilar anisotropic composites under mixed-mode loading. *Journal of applied mechanics*, 50(1):179–183, 1983.
- [61] C. Kassapoglou and P.A. Lagace. An efficient method for the calculation of interlaminar stresses in composite materials. *Journal of Applied Mechanics*, 53(4):744–750, 1986.
- [62] C. Kassapoglou and P.A. Lagace. Closed form solutions for the interlaminar stress field in angle-ply and cross-ply laminates. *Journal of Composite Materials*, 21(4):292–308, 1987.
- [63] J.P.H. Webber and S.K. Morton. An analytical solution for the thermal stresses at the free edges of laminated plates. *Composites science and technology*, 46(2):175–185, 1993.

- [64] W. Becker. Closed-form solution for the free-edge effect in cross-ply laminates. *Composite Structures*, 26(1):39–45, 1993.
- [65] C. Kassapoglou. Determination of interlaminar stresses in composite laminates under combined loads. *Journal of reinforced plastics and composites*, 9(1):33–58, 1990.
- [66] W.L. Yin. Free-edge effects in anisotropic laminates under extension, bending and twisting, part i: a stress-function-based variational approach. *Journal of Applied Mechanics*, 61(2):410–415, 1994.
- [67] W.L. Yin. Free-edge effects in anisotropic laminates under extension, bending, and twisting, part ii: eigenfunction analysis and the results for symmetric laminates. *Journal of Applied Mechanics*, 61(2):416–421, 1994.
- [68] W.L. Yin. The effect of temperature gradient on the free-edge interlaminar stresses in multi-layered structures. *Journal of composite materials*, 31(24):2460–2477, 1997.
- [69] R.B. Pipes and N.J. Pagano. Interlaminar stresses in composite laminates under uniform axial extension. *Journal of Composite Materials*, 4(4):538–548, 1970.
- [70] E. Altus, A. Rotem, and M. Shmueli. Free edge effect in angle ply laminates- a new three dimensional finite difference solution. *Journal of Composite Materials*, 14:21–30, 1980.
- [71] K. Bhaskar, T.K. Varadan, and C. Jacob. Free edge stresses in laminated cylindrical shells due to axisymmetric transverse loads. *JOURNAL-AERONAUTICAL SOCIETY OF INDIA*, 52(1):26–38, 2000.
- [72] N.J. Salamon. Interlaminar stressess in a layered composite laminate in bending. *Fibre Science and Technology*, 11(4):305–317, 1978.
- [73] A.S.D. Wang and F.W. Crossman. Some new results on edge effect in symmetric composite laminates. *Journal of Composite Materials*, 11(1):92–106, 1977.

- [74] A.S.D. Wang and F.W. Crossman. Edge effects on thermally induced stresses in composite laminates. *Journal of Composite Materials*, 11(3):300–312, 1977.
- [75] C.T. Herakovich, G.D. Renieri, and H.F. Brinson. Finite element analysis of mechanical and thermal edge effects in composite laminates. In *Army Symposium on Solid Mechanics, Composite Materials: The Influence of Mechanics of Failure on Design, Cape Cod (USA)*, pages 237–248, 1976.
- [76] G. Isakson and A. Levy. Finite-element analysis of interlaminar shear in fibrous composites. *Journal of Composite Materials*, 5(2):273–276, 1971.
- [77] E.F. Rybicki. Approximate three-dimensional solutions for symmetric laminates under inplane loading. *Journal of Composite Materials*, 5(3):354–360, 1971.
- [78] J.Y. Kim and C.S. Hong. Three-dimensional finite element analysis of interlaminar stresses in thick composite laminates. *Computers & structures*, 40(6):1395–1404, 1991.
- [79] U. Icardi and A.M. Bertetto. An evaluation of the influence of geometry and of material properties at free edges and at corners of composite laminates. *Computers & structures*, 57(4):555–571, 1995.
- [80] L.B. Lessard, A.S. Schmidt, and M.M. Shokrieh. Three-dimensional stress analysis of free-edge effects in a simple composite cross-ply laminate. *International Journal of Solids and Structures*, 33(15):2243–2259, 1996.
- [81] S. Yi and H.H. Hilton. Finite element analysis of free edge stresses in non-linear viscoelastic composites under uniaxial extension, bending and twisting loadings. *International journal for numerical methods in engineering*, 40(22):4225–4238, 1997.
- [82] R.L. Spilker and S.C. Chou. Edge effects in symmetric composite laminates- importance of satisfying the traction-free-edge condition. *Journal of Composite Materials*, 14:2–20, 1980.

- [83] C.Y. Lee and J.M. Chen. Interlaminar shear stress analysis of composite laminate with layer reduction technique. *International journal for numerical methods in engineering*, 39(5):847–865, 1996.
- [84] D.H. Robbins and J.N. Reddy. Variable kinematic modelling of laminated composite plates. *International Journal for Numerical Methods in Engineering*, 39(13):2283–2317, 1996.
- [85] P. Gaudenzi, A. Mannini, and R. Carbonaro. Multi-layer higher-order finite elements for the analysis of free-edge stresses in composite laminates. *International journal for numerical methods in engineering*, 41(5):851–873, 1998.
- [86] E. Martin, D. Leguillon, and N. Carrère. A twofold strength and toughness criterion for the onset of free-edge shear delamination in angle-ply laminates. *International journal of Solids and Structures*, 47(9):1297–1305, 2010.
- [87] V.T. Nguyen and J.F. Caron. Finite element analysis of free-edge stresses in composite laminates under mechanical and thermal loading. *Composites Science and Technology*, 69(1):40–49, 2009.
- [88] R.P. Carreira, J.F. Caron, and A.D. Diaz. Model of multilayered materials for interface stresses estimation and validation by finite element calculations. *Mechanics of materials*, 34(4):217–230, 2002.
- [89] S.H. Lo, W. Zhen, Y.K. Cheung, and C. Wanji. An enhanced global–local higher-order theory for the free edge effect in laminates. *Composite structures*, 81(4):499–510, 2007.
- [90] M. M. Pavlick, W. S. Johnson, B. Jensen, and E. Weiser. Evaluation of mechanical properties of advanced polymers for composite cryotank applications. *Composites Part A: Applied Science and Manufacturing*, 40(4):359–367, 2009.

- [91] U. Galan, Y. Lin, G.J. Ehlert, and H.A. Sodano. Effect of zno nanowire morphology on the interfacial strength of nanowire coated carbon fibers. *Composites Science and Technology*, 71(7):946–954, 2011.
- [92] S.S. Wicks, W. Wang, M.R. Williams, and B.L. Wardle. Multi-scale interlaminar fracture mechanisms in woven composite laminates reinforced with aligned carbon nanotubes. *Composites Science and Technology*, 100:128–135, 2014.
- [93] A. Szekrenyes. Overview on the experimental investigations of the fracture toughness in composite materials. *Hungarian Electronic Journal of Sciences*, <http://hej.sze.hu/>, Mechanical Engineering Section, MET-020507-A, 2002.
- [94] K.A. Dransfield, L.K. Jain, and Y. Mai. On the effects of stitching in cfrpsi. mode i delamination toughness. *Composites Science and Technology*, 58(6):815–827, 1998.
- [95] A. Argüelles, J. Viña, A.F. Canteli, M.A. Castrillo, and J. Bonhomme. Interlaminar crack initiation and growth rate in a carbon-fibre epoxy composite under mode-i fatigue loading. *Composites Science and Technology*, 68(12):2325–2331, 2008.
- [96] R. Khan, C.D. Rans, and R. Benedictus. Effect of stress ratio on delamination growth behavior in unidirectional carbon/epoxy under mode i fatigue loading. *Proceedings ICCM. Edinburgh*, 2009.
- [97] R. Rikards, F.G. Buchholz, A.K. Bledzki, G. Wacker, and A. Korjakin. Mode i, mode ii, and mixed-mode i/ii interlaminar fracture toughness of gfrp influenced by fiber surface treatment. *Mechanics of composite materials*, 32(5):439–462, 1996.
- [98] T. K. O’Brien. Characterization of delamination onset and growth in a composite laminate. In *Damage in Composite Materials: Basic Mechanisms, Accumulation, Tolerance, and Characterization*. ASTM International, 1982.

- [99] P. Robinson and S. Das. Mode i dcB testing of composite laminates reinforced with z-direction pins: a simple model for the investigation of data reduction strategies. *Engineering Fracture Mechanics*, 71(3):345–364, 2004.
- [100] R.J. Sager, P.J. Klein, D.C. Davis, D.C. Lagoudas, G.L. Warren, and H. Sue. Interlaminar fracture toughness of woven fabric composite laminates with carbon nanotube/epoxy interleaf films. *Journal of applied polymer science*, 121(4):2394–2405, 2011.
- [101] Z. Fan, M.H. Santare, and S.G. Advani. Interlaminar shear strength of glass fiber reinforced epoxy composites enhanced with multi-walled carbon nanotubes. *Composites Part A: Applied science and manufacturing*, 39(3):540–554, 2008.
- [102] B. Ashrafi, J. Guan, V. Mirjalili, Y. Zhang, L. Chun, P. Hubert, B. Simard, C.T. Kingston, O. Bourne, and A. Johnston. Enhancement of mechanical performance of epoxy/carbon fiber laminate composites using single-walled carbon nanotubes. *Composites science and technology*, 71(13):1569–1578, 2011.
- [103] A.G. Castellanos, M.S. Islam, M.A.I. Shuvo, Y. Lin, and P. Prabhakar. Nanowire reinforcement of woven composites for enhancing interlaminar fracture toughness. *Journal of Sandwich Structures and Materials*, page 1099636216650989, 2016.
- [104] A. Castellanos, M.S. Islam, S. Quevedo, M.A.I. Shuvo, Y. Lin, and P. Prabhakar. Nanowire stiffening of woven composites towards enhancing interlaminar fracture toughness. In *American Society of Composites-30th Technical Conference*, 2015.
- [105] A. Castellanos, M.S. Islam, M.A.I. Shuvo, Y. Lin, and P. Prabhakar. Impact response of woven composites with interlaminar reinforcement. In *57th AIAA/ASCE/AHS/ASC Structures, Structural Dynamics, and Materials Conference*, page 1236, 2016.

- [106] K. Kong, B.K. Deka, S. K. Kwak, A. Oh, H. Kim, Y. Park, and H.W. Park. Processing and mechanical characterization of zno/polyester woven carbon–fiber composites with different zno concentrations. *Composites Part A: Applied Science and Manufacturing*, 55:152–160, 2013.
- [107] H. Hwang, M.H. Malakooti, B.A. Patterson, and H.A. Sodano. Increased inter yarn friction through zno nanowire arrays grown on aramid fabric. *Composites Science and Technology*, 107:75–81, 2015.
- [108] J.B. Baxter and E.S. Aydil. Nanowire-based dye-sensitized solar cells. *Applied Physics Letters*, 86(5):053114, 2005.
- [109] X. Wang, J. Song, J. Liu, and Z.L. Wang. Direct-current nanogenerator driven by ultrasonic waves. *Science*, 316(5821):102–105, 2007.
- [110] Y. Lin, G. Ehlert, and H.A. Sodano. Increased interface strength in carbon fiber composites through a zno nanowire interphase. *Advanced functional materials*, 19(16):2654–2660, 2009.
- [111] K. Kong, B.K. Deka, M. Kim, A. Oh, H. Kim, Y. Park, and H.W. Park. Interlaminar resistive heating behavior of woven carbon fiber composite laminates modified with zno nanorods. *Composites Science and Technology*, 100:83–91, 2014.
- [112] M. S. Islam, E. Melendez-Soto, A. G. Castellanos, and P. Prabhakar. Investigation of woven composites as potential cryogenic tank materials. *Cryogenics*, 72:82–89, 2015.
- [113] M.S. Islam, A.G. Castellanos, and P. Prabhakar. Effect of curing induced parameters during manufacturing of textile composites. In *American Society of Composites-30th Technical Conference*, 2015.
- [114] M.S. Islam and P. Prabhakar. Computational modeling of curing induced damage due to compaction on woven fabric composite. In *American Society of Composites-29th Technical Conference/16th US-Japan Conference on Composite Materials*, 2015.

- [115] M.S. Islam and P. Prabhakar. Effect of compaction during manufacturing of textile composites. In *International Conference on Mechanical, Industrial and Energy Engineering*, 2014.
- [116] M.S. Islam, P. Prabhakar, H. Kreiger, S. Stapleton, and T. Gries. Prediction of damage due to compaction during manufacturing of textile composites. In *16th European Conference on Composite Materials*, 2014.
- [117] N. Rabearison, C. Jochum, and J. Grandidier. A fem coupling model for properties prediction during the curing of an epoxy matrix. *Computational Materials Science*, 45(3):715–724, 2009.
- [118] T.J. Corden, I.A. Jones, D.T. Jones, and V. Middleton. The mechanisms of interlaminar cracking in thick resin transfer moulded composite cylinders. *Composites Part A: Applied Science and Manufacturing*, 29(4):455–464, 1998.
- [119] A.R. Plepys and R.J. Farris. Evolution of residual stresses in three-dimensionally constrained epoxy resins. *Polymer*, 31(10):1932–1936, 1990.
- [120] M. R. Kamal. Thermoset characterization for moldability analysis. *Polymer Engineering & Science*, 14(3):231–239, 1974.
- [121] A. Plepys, M. S. Vratsanos, and R. J. Farris. Determination of residual stresses using incremental linear elasticity. *Composite structures*, 27(1):51–56, 1994.
- [122] T. A. Bogetti and J. W. Gillespie. Process-induced stress and deformation in thick-section thermoset composite laminates. *Journal of Composite Materials*, 26(5):626–660, 1992.
- [123] D. Adolf and R. Chambers. Verification of the capability for quantitative stress prediction during epoxy cure. *Polymer*, 38(21):5481–5490, 1997.

- [124] D. B. Adolf, J. E. Martin, R. S. Chambers, S. N. Burchett, and T. R. Guess. Stresses during thermoset cure. *Journal of materials research*, 13(03):530–550, 1998.
- [125] J. Lange, S. Toll, J. E. Månson, and A. Hult. Residual stress build-up in thermoset films cured above their ultimate glass transition temperature. *Polymer*, 36(16):3135–3141, 1995.
- [126] S.R. White and H.T. Hahn. Process modeling of composite materials: residual stress development during cure. part ii. experimental validation. *Journal of Composite Materials*, 26(16):2423–2453, 1992.
- [127] Y. Mei. *Stress evolution in a conductive adhesive during curing and cooling*. 2000.
- [128] Y. Mei, A. F. Yee, A. S. Wineman, and C. Xia. Stress evolution during thermoset cure. In *MRS Proceedings*, volume 515, page 195. Cambridge Univ Press, 1998.
- [129] C. Heinrich, M. Aldridge, A. S. Wineman, J. Kieffer, A. M. Waas, and K. W. Shahwan. Generation of heat and stress during the cure of polymers used in fiber composites. *International Journal of Engineering Science*, 53:85–111, 2012.
- [130] S. Song, A. M. Waas, K. W. Shahwan, X. Xiao, and O. Faruque. Braided textile composites under compressive loads: modeling the response, strength and degradation. *Composites Science and Technology*, 67(15):3059–3070, 2007.
- [131] M. W. Hyer and A. M. Waas. Micromechanics of linear elastic continuous fiber composites. *Comprehensive composite materials*, 1:345–375, 2000.
- [132] M. Hossain, G. Possart, and P. Steinmann. A small-strain model to simulate the curing of thermosets. *Computational Mechanics*, 43(6):769–779, 2009.
- [133] Z. P. Bažant and B. H. Oh. Crack band theory for fracture of concrete. *Matériaux et construction*, 16(3):155–177, 1983.

- [134] C.D. Rudd. Resin transfer molding and structural reaction injection molding. *Materials Park, OH: ASM International, 2001.*, pages 492–500, 2001.
- [135] N. Ikegawa, H. Hamada, and Z. Maekawa. Effect of compression process on void behavior in structural resin transfer molding. *Polymer Engineering & Science*, 36(7):953–962, 1996.
- [136] M. Revello, L. Saggese, and E. Gaiero. Compression molding of smcs. *Comprehensive composite materials*, pages 763–805, 2000.
- [137] J. Charrier. Polymeric materials and processing: plastics, elastomers, and composites. 1991.

Curriculum Vitae

Md Shariful Islam, the third child of Md Sirajul Islam and Mst. Sufia Khatun, was born on October 18, 1985 in Meherpur, Bangladesh. He completed his secondary school certificate from Dariapur High School and his higher secondary school certificate from Mujibnagar Degree College, Bangladesh and then joined Khulna University of Engineering & Technology (KUET) in 2004 to pursue his Bachelor of Science in Mechanical Engineering. After graduating from KUET he joined at the Department of Mechanical Engineering of the same university as a lecturer on October 2008 and served there for more than three years. Then he came to United States for higher study. He earned his Master of Science in Mechanical Engineering from the University of Texas at El Paso (UTEP) in May 2013. He started his Ph.D. at UTEP in August 2013. He was working as a Graduate Teaching / Research Assistant for the department. His research was focused manufacturing and mechanics of polymer matrix composites. He has published his research findings in several peer reviewed journals and also presented his research in many international conferences. He won *Cytec Student Paper Award for Composite Processing* at the ASC 29th Technical Conference / 16th US-Japan Conference on Composite Materials, San Diego, California, USA, September 2014 and *Best Paper Award* at the International Conference on Mechanical, Industrial and Energy Engineering, Khulna, Bangladesh, December 2014.

Permanent address: Village: Purondorpur, P.O. Dariapur

P.S. Mujibnagar, Dist. Meherpur, Bangladesh

This thesis was typed by Md Shariful Islam.